Seismic Performance Evaluation of an Eight-Story Steel-Reinforced Concrete Building Using Performance Curves of the Building

(8 階建 SRC 造建物の建物性能曲線による耐震性能評価)

LI LIGANG

(李立岗)

DOCTOR OF ENGINEERING

GRADUATE SCHOOL OF ENVIRONMENT STUDIES

NAGOYA UNIVERSITY, JAPAN

(名古屋大学大学院環境学研究科　博士(工学))

2015

Contents:

II

Chapter 1
INTRODUCTION

1.1 Research Background

Destructive earthquakes caused much serious earthquake damage of buildings, and that is the main reason of the large casualties. The number of refugees will increase after the main earthquakes. In order to recover the social order and make the refugees go back to their homes as soon as possible, the safety of the buildings should be confirmed. And the buildings should be judged strong enough to withstand the following aftershocks, which may even cause much more structural damage than the main shocks. As a result, a quick and effective evaluation method for the earthquake damage in main shocks and for the prediction of the residual seismic capacity (related with the collapse of the building) of the buildings in the aftershocks should be developed.

The current local damage evaluation method in the Guideline for Post-Earthquake Damage Evaluation and Rehabilitation of RC Buildings in Japan[1] is based on the visual observation of the cracks of the structural elements (columns and walls); and the Residual Seismic Capacity Ratio Index R (decided by I_s, seismic capacity index of structure before earthquake damage, and I_s^D seismic capacity index of structure considering deteriorated member capacity) is employed, which is used for judging the earthquake damage level of the buildings. However, the method has three main drawbacks: (a) it takes too much time, and needs many engineers; (b) the method cannot detect some hidden damage; and the assessment of the

damage is easily influenced by subjective judge of the engineers[2] (influent the accuracy of I_s^p); (c) the real building is different from the design model because of the accuracy of the construction (influent the accuracy of the initial I_s,), so the accuracy of the index R is a challenge. Therefore, although the observation method can help know the distribution and sizes of the cracks of some essential structural elements in the main shocks, it is impossible to quickly and effectively assess the residual seismic capacity after the main shock and neither to judge whether the residual seismic capacity of the building can withstand the strong aftershocks.

Unlike visual observation method, earthquake response records are utilized to monitor the structural health (Global Health Monitoring Techniques[3]). In most of those kinds of methods, the changes of the dynamic characteristics (such as fundamental frequency and modal shapes) of a building can be identified, which are used to judge the global damage. For those methods, noise is the most important influence factor on the accuracy of the evaluation results of the global damage. A new method [4] to detect earthquake damage has been brought out, which is based on the wave propagation theory and wavelet transform. However, these methods mainly focused on the earthquake damage detection of a building in main shocks, but cannot predict the collapse risk of the building in aftershocks.

In the seismic design, Capacity-Demand Spectrum[5, 6, 7, 8] (based on nonlinear static pushover analysis and earthquake response spectrum) is a useful method to evaluate the seismic capacity of a building, which can give the capacity point and demand point of a building. Similarly, some researcher[2]

think that earthquake response data of the building during main shocks can be used to get a Real-Time Capacity-Demand Spectrum (capacity spectrum in the main shock: performance curve, namely $S_a - S_d$ curve in this paper; Demand spectrum: earthquake response spectrum for aftershocks) of an in-service building for the aftershocks, then the safety of the building in aftershocks can be predicted based on the Real-Time Capacity-Demand Spectrum. The concept of the evaluation system is shown in Figure 1.1. In Figure 1, CA$_M$ represents the maximum response point in the main shock, DE$_A$ represents the demand point in aftershock and CP is the collapse point of a building. The basic principle of the method is to make sure that the point DE$_A$ should be never beyond the point CP, which means that the seismic capacity should satisfy the demand capacity of a building.
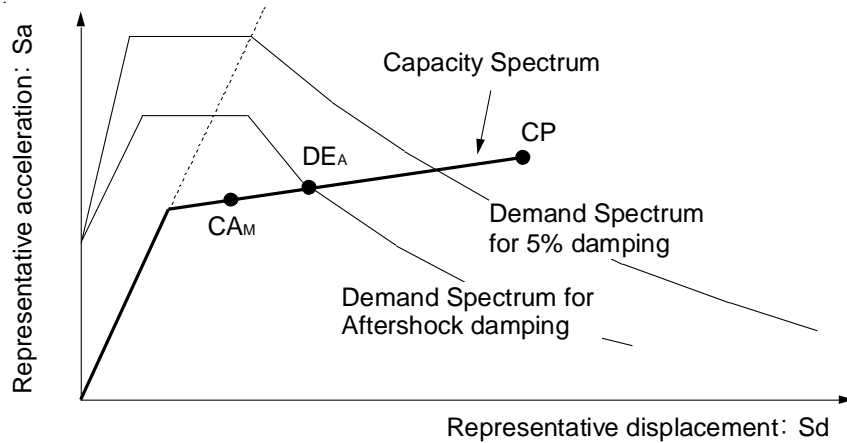
Fig. 1.1 Concept of the structural safety evaluation in aftershock

The method mentioned in Figure 1.1 can expand the application of the Capacity-Demand Spectrum theory from the design stage to the in-service

3

stage of the building. Firstly, seismic performance evaluation of a real building can be made using the seismic response caused by the main shocks. The performance curve can show the performance changes of the building from small responses to the maximum response; the linearity and nonlinearity of the earthquake response of the measurement building can also be observed directly. Second application is the predication of the structural safety of a real building in the aftershocks, see Figure 1.1. In order to complete the method shown in Figure 1.1, several problems should be solved: (1) how to get accurate enough seismic performance curve---$S_a - S_d$ curve; (2) the definition of the aftershocks; (3) the definition of the damping.

As for the problems (2) and (3), they were discussed briefly[9, 10], and some further research needs to be made in the future. While as for the problem (1), a new signal processing method---Wavelet Transform Technology has already been employed to get fundamental response of the structure; and then the fundamental response can be used to get the $S_a - S_d$ curve. Three shaking table tests, specimens are One-Story models (SDOF model) and Three-Story model (MDOF model), were carried out to show that the useful $S_a - S_d$ curves of the real structures can be achieved[11, 12, 13, 14]; and among these research, the modeling of the $S_a - S_d$ curve and accuracy of estimated maximum displacement in aftershock were discussed. At the same time, the importance of the peak response points was also noticed, which were used to get $S_a - S_d$ skeleton curves. However, in order to make the method widely applied, there are some problems we need to solve as follows:

(1) The application of $S_a - S_d$ curves for real buildings is rare in the past research because of lack of the valuable field measurement data.

(2) There is no research on how to use $S_a - S_d$ curve to evaluate the earthquake damage, and the most important point is how to define the initial secant stiffness of the $S_a - S_d$ curve.

(3) In order to realize the automatic calculation by computer, an automatic selection method of the fundamental response should be set up.

(4) It is necessary to evaluate the seismic performance of the soil considering the SSI effect in the seismic design, so the research on how to use $S_a - S_d$ curve of the superstructure to evaluate the soil properties during earthquakes is important.

Based on those research background mentioned above, the research in this paper was carried out.

1.2 Research Contents and Objectives

The main objective of this research in this paper is to study the application of the $S_a - S_d$ curves of real buildings using field measurement data. Theoretically at the peak response points, damping forces are zero (because the velocity is zero), then the relationship between the inertial forces and deformation of the building (performance curve for the superstructure) can be set up directly; similarly, once the peak response points of the rotation motion of the foundation were known, the relationship between the inertial moment of building and the rotation displacement (reflects the seismic performance of the soil) could be set up. Based on the two performance

curves, the earthquake damage evaluation of the superstructure and the soil stiffness evaluation can be made. In the paper, earthquake response records of an 8-story Steel-Reinforce Concrete building were studied. I used the field measurement data to evaluate the seismic performance of the building. The detailed research contents of the thesis are as follows:

(1) Chapter 2: Detailed introduction was made on the past research of the performance curves, especially the deduction of the $S_a - S_d$ curve, application of the Wavelet Transform Technology and the definition of the fundamental response.

(2) Chapter 3: Study the earthquake response (deformation and rocking motion of the building) and the changes of the dynamic characteristics of the building. In this section, I found that the decrease of the fundamental frequency of the building happened. However, two major factors influence the changes of the fundamental frequency: one is the stiffness of the superstructure and the other one is the soil stiffness. In order to explain the phenomenon, I used the performance curve to evaluate the stiffness of the superstructure and the soil in Chapter 4 and Chapter 5.

(3) Chapter 4: Evaluate the earthquake damage using $S_a - S_d$ curve of the building, and conform the practicability of the $S_a - S_d$ curve for the real buildings in strong earthquakes.

(4) Chapter 5: Estimate the soil stiffness using performance curve of the building, and $R_a - R_d$ curves were brought out to evaluate the linearity and nonlinearity of the soil response.

Compared with the previous research, we brought out some new thoughts

and got some new calculation results in the paper, as follows:

(1) Massive of measurement earthquake response data of a real SRC building were accumulated, and I used the data to test the application of the $S_a - S_d$ curves for real buildings.

(2) I brought out a simple method to define the initial secant stiffness of the $S_a - S_d$ curves, and the usefulness of the method was evaluated and confirmed.

(3) An automatic selection method of the fundamental response based on the energy theory was brought out in this paper.

(4) I used the $S_a - S_d$ curves of the superstructure and the rotation motions of the foundation to evaluate the soil stiffness during earthquakes.

References:

1) Yoshiaki NAKANO, Masaki MAEDA, Hiroshi KURAMOTO and Masaya MURAKAMI: GUIDELINES FOR POST-EARTHQUAKE DAMAGE EVALUATION AND REHABILITATION OF RC BUILDINGS IN JAPAN. 13th World Conference on Earthquake Engineering, Paper NO.124, Vancouver, B.C., Canada, August 1-6, 2004.

2) Koichi Kusunoki and Masaomi Teshigawara: A New Acceleration Integration Method to Develop a Real-Time Residual Seismic Capacity Evaluation System, J. Struct. Constr. Eng., AIJ, No. 569, pp. 119–126, 2003.7.

3) Peter C. Chang, Alison Flatau and S. C. Liu: Review Paper: Health Monitoring of Civil Infrastructure, Structural Health Monitoring, Vol. 2(3),

pp. 257–267, 2003.

4) Maria I. Todorovska, M. Rahmani: Recent Advances in Wave Travel Time Based Methodology for Structural Health Monitoring and Early Earthquake Damage Detection in Buildings, 15th World Conference of Earthquake Engineering, LISBOA, 2012.

5) Sigmund A. Freeman: Review of the Development of the Capacity Spectrum Method, ISET Journal of Earthquake Technology, Paper No. 438, Vol.41, No.1, pp.1-13, March 2004.

6) Peter Fajfar and M.EERI: A Nonlinear Analysis Method for Performance Based Seismic Design, Earthquake Spectra, Vol.16, No.3, pp.573-592, August 2000.

7) Anil K. Chopra and Rakesh K. Goel: Capacity-Demand-Diagram Methods for Estimating Seismic Deformation of Inelastic Structures: SDF Systems, Pacific Earthquake Engineering Research Center, Report No. PEER-1999/02, April 1999.

8) Hiroshi KURAMOTO, Masaomi TESHIGAWARA, Toshifumi OKUZONO, Norihide KOSHIKA, Masaharu TAKAYAMA and Tomihiro HORI: PREDICTING THE EARTHQUAKE RESPONSE OF BUILDINGS USING EQUIVALENT SINGLE DEGREE OF FREEDOM SYSTEM, 12 WCEE, Paper No. 1039, 2000

9) Koichi KUSUNOKI, Masaomi TESHIGAWARA and Eiji KOIDE: Development of real-time residual seismic capacity evaluation system No 1: Outline of the evaluation method, Summaries of Technical Papers of Annual Meeting Architectural Institute of Japan, Tokai, Japan, pp.961-962, 2003.

10) Koichi KUSUNOKI, Masaomi TESHIGAWARA: Development of real-time residual seismic capacity evaluation system No 3: Substitute damping ratio for an aftershock, Summaries of Technical Papers of Annual Meeting Architectural Institute of Japan, Kanto, Japan, pp.949-950, 2006.

11) Manabu Kawamura, Koichi Kusunoki, Miho Yamashita, Yuki Kattori, Daiki Hinata, Miguel Augusto DIAZ FIGUEROA and Akira Tasai: Study of a New Method to Compute the Performance Curve of Real Structures with Acceleration Sensors in the case of SDOF System Structures, J. Struct. Constr. Eng. AIJ, No.688, pp.1061–1069, 2013.6.

12) Koichi Kusunoki, Daiki Hinata, Yuki Hattori, and Akira Tasai: Development of a new method of realtime residual seismic capacity evaluation of existing structures with accelerometers in the case of MDOF system structures, J. Struct. Constr. Eng., AIJ, No. 699, pp. 613–620, 2014.5.

13) Yuki Hattori, Koichi Kusunoki, Daiki Hinata and Akira Tasai: Research on the Modeling of Performance curve with Accelerometers, Proceedings of the Japan Concrete Institute, Vol.36, No.2, pp.745-750, 2014.

14) Yuki Hattori, Koichi Kusunoki, Daiki Hinata and Akira Tasai: Experiment Study on the Accuracy of the Response Point in Aftershock Based on Residual Seismic Capacity Evaluation, Proceedings of the Japan Concrete Institute, Vol.36, No.2, pp.793-798, 2014.

Chapter 2
Past Research on Performance Curve

2.1 Overview

Generally, a multi-story building is modeled as a kind of Multi-Degree-of-Freedom (MDOF) model. Then the MDOF model can be reduced into an equivalent Single-Degree-of-Freedom (SDOF) model, see Figure 2.1. The simplification procedure is the fundamental theory of the performance curve. In the design stage, the performance curve of a structure is obtained using static nonlinear pushover analysis, which is a kind of pseudo-dynamic analysis. While for the building installed with accelerometers, the performance curve is directly obtained using field measurement acceleration data of earthquake responses. A kind of signal processing method—Wavelet Transform Technology (WWT) was employed, which can be used to extract the fundamental response. In this chapter, the basic theory of performance curve, fundamental response and WWT were introduced.

2.2 Reduction of the Multi-Degree of Freedom model[1, 2]

The differential equations governing the response of a multistory building to horizontal earthquake $\ddot{u}_g(t)$ are as follows:

$$[M]\{\ddot{U}\} + [C]\{\dot{U}\} + [K]\{U\} = -[M]\{l\}\ddot{u}_g(t) \qquad (2.1)$$

Where $\{U\}$ is the displacement vector of the MDOF model; $[M]$, $[C]$ and $[K]$ are the mass, damping, and lateral stiffness matrices of the systems; each element of the influence vector $\{l\}$ is equal to 1.

(a) MDOF model   (b) SDOF model
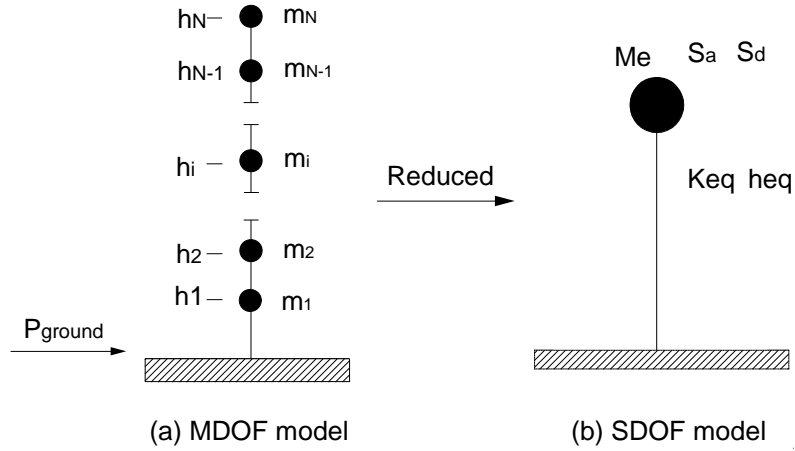
Fig. 2.1 Reduction of MDOF model to SDOF model for fixed foundation

The right-hand side of Equation (2.1) can be interpreted as effective earthquake forces:

$$\{\mathbf{P}_{ground}(t)\} = -[M]\{l\}\ddot{u}_g(t) \tag{2.2}$$

The spatial distribution of ground motions over the height of the building is defined by the vector $\{s\}=[M]\{l\}$. This force distribution can be expanded as a summation of modal inertia force distribution $\boldsymbol{s}_n$, which is as follows:

$$\sum_{n=1}^{N}\{s_n\} = \sum_{n=1}^{N}\Gamma_n[M]\{\phi_n\} \tag{2.3}$$

where $\{\phi_n\}$ is the nth natural vibration mode of the structure, and

$$\Gamma_n = \frac{L_n}{M_n}, \ L_n = \{\phi_n\}^T[M]\{l\}, \ M_n = \{\phi_n\}^T[M]\{\phi_n\} \tag{2.4}$$

The effective earthquake forces can then be expressed as

$$\{\mathbf{P}_{ground}(t)\} = \sum_{n=1}^{N}-\{s_n\}\ddot{u}_g(t) \tag{2.5}$$

The contribution of the nth mode to $\mathbf{s}$ and to $\mathbf{P}_{ground}(t)$ is as follows

$$\{s_n\} = \Gamma_n[M]\{\phi_n\} \tag{2.6a}$$

$$\{P_{ground,n}(t)\} = -\{s_n\}\ddot{u}_g(t) \tag{2.6b}$$

The response of the MDOF system to $\{P_{ground,n}(t)\}$ is entirely in the nth-mode, with no contributions from other modes. Then the floor displacements are

$$\{u_n(t)\} = \{\phi_n\}q_n(t) \tag{2.7}$$

Where the modal response $q_n(t)$ is governed by

$$\ddot{q}_n(t)+2\xi_n\omega_n\dot{q}_n(t)+\omega_n^2 q_n(t) = -\Gamma_n\ddot{u}_g(t) \tag{2.8}$$

in which ω_n is the natural vibration frequency and ξ_n is the damping ratio for the nth mode. The solution $q_n(t)$ of Equation (2.8) is given by

$$q_n(t)= \Gamma_n D_n(t) \tag{2.9}$$

where $D_n(t)$ is governed by the equation of motion for the nth-mode linear SDOF system, an SDOF system with vibration properties—natural frequency ω_n and damping ratio ξ_n of the nth-mode of the MDOF system, subjected to $\ddot{u}_g(t)$:

$$\ddot{D}_n(t)+2\xi_n\omega_n\dot{D}_n(t)+\omega_n^2 D_n(t) = -\ddot{u}_g(t) \tag{2.10}$$

Substituting Equation (2.9) into Equation (2.7) gives the floor displacements are as follows

$$\{u_n(t)\}= \Gamma_n \{\phi_n\}D_n(t) \tag{2.11}$$

Then the corresponding equivalent static forces for the nth mode are

$$\{f_n(t)\}=[K]\{u_n(t)\}=\Gamma_n[K] \{\phi_n\}D_n(t) \tag{2.12}$$

As for the nth-mode linear SDOF system,

$$[K] \{\phi_n\}=\omega_n^2 [M]\{\phi_n\} \tag{2.13}$$

Substituting Equation (2.13) into Equation (2.12), then

$$\{f_n(t)\}=\Gamma_n [M]\{\phi_n\} A_n(t) \tag{2.14a}$$

$$A_n(t) = \omega_n^2 D_n(t) \tag{2.14b}$$

From the equations (2.11) and (2.14) respectively, ith floor displacements and shear forces for nth mode are as follows:

$$u_{in}(t)= \Gamma_n \, \phi_{in} D_n(t) = \frac{\sum_{j=1}^{N} m_j \, \phi_{jn}}{\sum_{j=1}^{N} m_j \, \phi_{jn}{}^2} \phi_{in} D_n(t) \qquad (2.15)$$

$$V_{in}=\sum_{j=i}^{N} f_{jn}(t) = \frac{\left(\sum_{j=1}^{N} m_j \, \phi_{jn}\right) \cdot \left(\sum_{j=i}^{N} m_j \, \phi_{jn}\right)}{\sum_{j=1}^{N} m_j \, \phi_{jn}{}^2} A_n(t) \qquad (2.16)$$

And for ith floor, the total floor displacements and shear forces are as follows

$$u_i(t)=\sum_{n=1}^{N}\left\{ \frac{\sum_{j=1}^{N} m_j \, \phi_{jn}}{\sum_{j=1}^{N} m_j \, \phi_{jn}{}^2} \phi_{in} D_n(t)\right\} \qquad (2.17)$$

$$V_i=\sum_{n=1}^{N}\left\{ \frac{\left\{\sum_{j=1}^{N} m_j \, \phi_{jn}\right\} \cdot \left(\sum_{j=i}^{N} m_j \, \phi_{jn}\right)}{\sum_{j=1}^{N} m_j \, \phi_{jn}{}^2} A_n(t)\right\} \qquad (2.18)$$

If only the first mode is considered, then the equations (2.17) and (2.18) will be as follows

$$u_{i1}(t)=\Gamma_1 \, \phi_{i1} D_1(t) \qquad (2.19)$$

$$V_{i1}=\Gamma_1 \cdot \left(\sum_{j=i}^{N} m_j \, \phi_{j1}\right) A_1(t) \qquad (2.20)$$

Where $u_{i1}(t)$ and V_{i1} are the lateral displacement and the lateral-shear force of the ith floor for the first mode. Then the representative displacement D_1 according to Equation (2.19) for the first mode will be as follows

$$D_1 = \frac{u_{N1}}{\Gamma_1 \, \phi_{N1}} \qquad (2.21)$$

And the equation (2.20) can be used to calculate the base shear force coefficient A_1 as follows

$$A_1 = \frac{V_{11}}{\Gamma_1 \cdot \left(\sum_{j=1}^{N} m_j \, \phi_{j1}\right)} \qquad (2.22)$$

Equations (2.21) and (2.22) (corresponding to the parameters S_d and S_a respectively in Figure 2.1) are the basics for the pushover analysis (to get the Capacity Spectrum of a structure), which has already been widely applied for the seismic design.

2.3 $S_a - S_d$ curve for Equivalent Single-Degree of Freedom Model

To get $S_a - S_d$ curve, only the first mode is considered. According to the equations (2.5) and (2.6b), then the dynamic equation (2.1) can be rewritten as follows

$$[M]\{\ddot{u}_1(t)\}+[C]\{\dot{u}_1(t)\}+[K]\{u_1(t)\} = -\{s_1\}\ddot{u}_g(t) \tag{2.23}$$

Where

$$\{u_1(t)\}=\Gamma_1 \{\phi_1\}D_1(t) \tag{2.24}$$

$$\{s_1\} = \Gamma_1[M]\{\phi_1\} \tag{2.25}$$

Let the left side of the Equation (2.24) be multiplied by mass matrix $[M]$ and unit column vector $\{1\}$, and displacement $D_1(t)$ can be got as follows

$$D_1(t) = \frac{[M]\{1\}\{u_1(t)\}}{\Gamma_1[M]\{1\}\{\phi_1\}} \tag{2.26}$$

Then $D_1(t)$ was defined as the representative displacement S_d,

$$S_d = \frac{\sum m_i \cdot u_{i1}}{M_e} \tag{2.27}$$

$$M_e = \Gamma_1[M]\{1\}\{\phi_1\} \quad \text{or} \quad M_e = \frac{(\sum m_i \cdot \phi_{i1})^2}{\sum m_i \cdot \phi_{i1}^2} \tag{2.28}$$

M_e can be found in Equation (2.28). And the inertial forces of each mass can be calculated as follows

$$\{f_1(t)\} = [M]\{\ddot{u}_1(t)\} + \{s_1\}\ddot{u}_g(t) \tag{2.29}$$

Equation (2.25) can be substituted into equation (2.29), then

$$\{f_1(t)\} = [M]\{\ddot{u}_1(t)\} + \Gamma_1[M]\{\phi_1\}\ddot{u}_g(t) \tag{2.30}$$

Then the base-shear force caused by inertial forces will be

$$V_f = \sum_{i=1}^{N} f_{i1}(t) = \sum_{i=1}^{N} m_i \ddot{u}_{i1}(t) + M_e \ddot{u}_g(t) \tag{2.31}$$

Substitute equation (2.31) into equation (2.32), then the base shear force coefficient S_a for the equivalent SDOF model will be defined as follows

$$S_a = \frac{V_f}{M_e} \tag{2.32}$$

Then

$$S_a = \frac{\sum_{i=1}^{N} m_i \ddot{u}_{i1}}{M_e} + \ddot{u}_g \tag{2.33}$$

Finally, the performance curve ($S_a - S_d$ curve) for earthquake can be got through Equations (2.27) and (2.33). At the peak response points, which the damping force is zero, S_d and S_a have the following relationship:

$$S_a = \omega_n^2 \cdot S_d \tag{2.34}$$

which is same with the relationship between D and A in Figure 2.1.

2.4 Wavelet Transform Technology and Fundamental response
2.4.1 Wavelet Transform Technology

Wavelet Transform Technique (WTT) has been applied in the engineering field in recent years, which is advantage over single processing methods based on Fast Fourier Transform (FFT) technique. KOICHI KUSUNOKI & MASAOMI TESHIGAWARA[3] have presented the method for using WTT (in their research, B-Spline Mother Wavelet and the order is 4) to calculate the fundamental response. The basic theory of WTT will be briefly introduced as follows.

For a series of discrete signal S, which the number of data is N and time step is dt, the signal can be decomposed into some specific component signals, which is

$$S = S_1 + S_2 + \cdots + S_i + \cdots + S_n + L_n \tag{2.35}$$

where component signal S_i is for the Rank i, and the number n (a round number) of component signals is decided by the equation (2.36)

$$n = log_2 N \tag{2.36}$$

For example, a series of the measurement signal S ($N = 12100$, $dt = 0.01$s) can be decomposed into 13 component signals (Rank 1 ~ Rank 13), see Figure 2.2. The frequency range of the signal of Rank i is limited, and different ranks are corresponding to different non-intersect frequency ranges. The Nyquist frequency for Rank i is calculated as follows

$$f_{s,\ i} = \left(dt \cdot 2^{i+1}\right)^{-1} \tag{2.37}$$

Table 2.1 Frequency ranges for each rank ($dt = 0.01$s)

Rank i	$f_{s,\ i}$ (Hz ~ Hz)
1	25 ~ 50
2	12.5 ~ 25
3	6.25 ~ 12.5
4	3.125 ~ 6.25
5	1.563 ~ 3.125
6	0.781 ~ 1.563
7	0.391 ~ 0.781
8	0.195 ~ 0.391
9	0.098 ~ 0.195
10	0.049 ~ 0.098
11	0.024 ~0.049
12	0.012 ~ 0.024
13	0.006 ~ 0.012

It means that time step dt is an important factor to change the size of

frequency ranges of the component signals, Table 2.1 shows the frequency ranges for the time step $dt = 0.01$s.
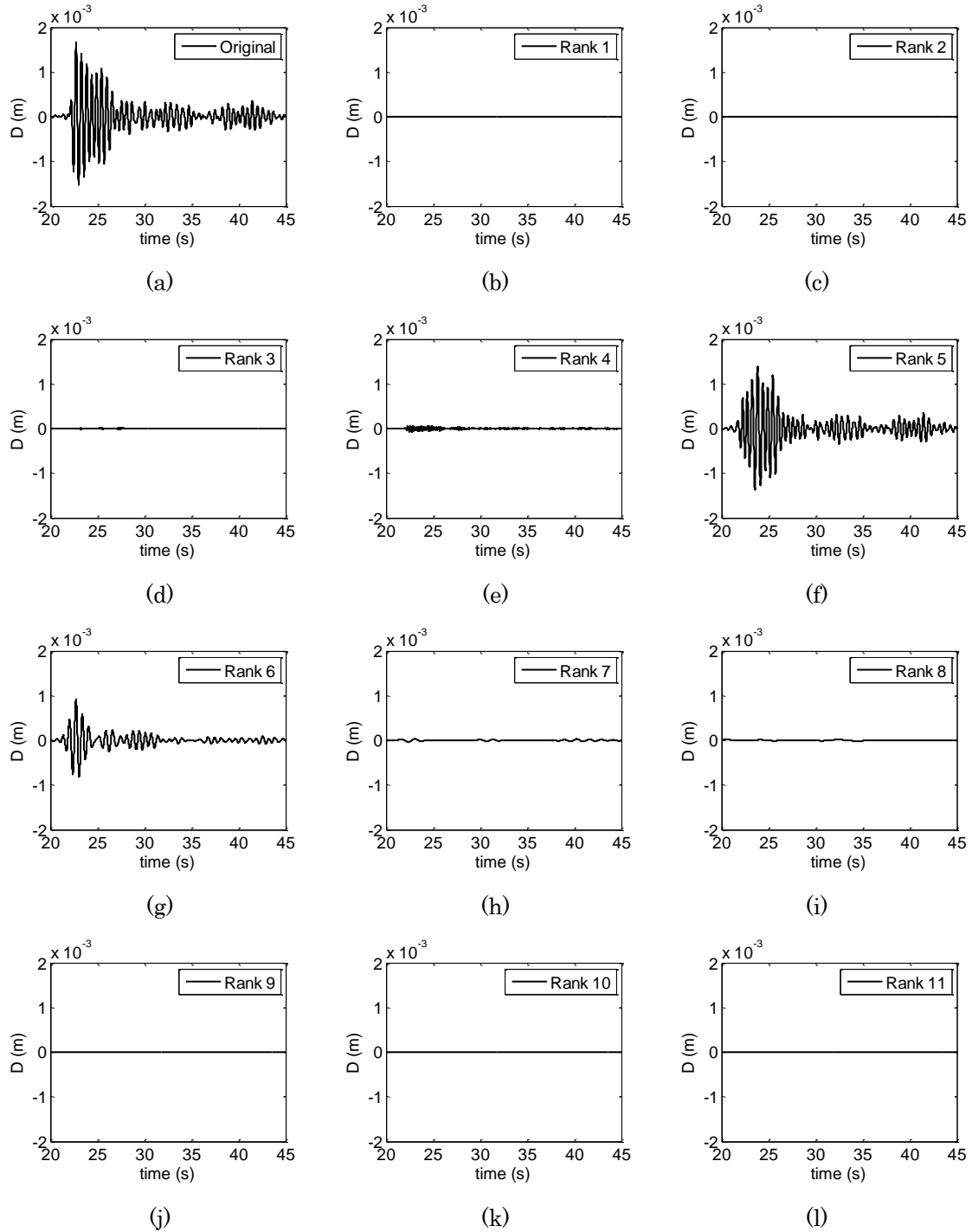
Fig. 2.2 Original signal S and component signals of each rank (time step dt= 0.01s)
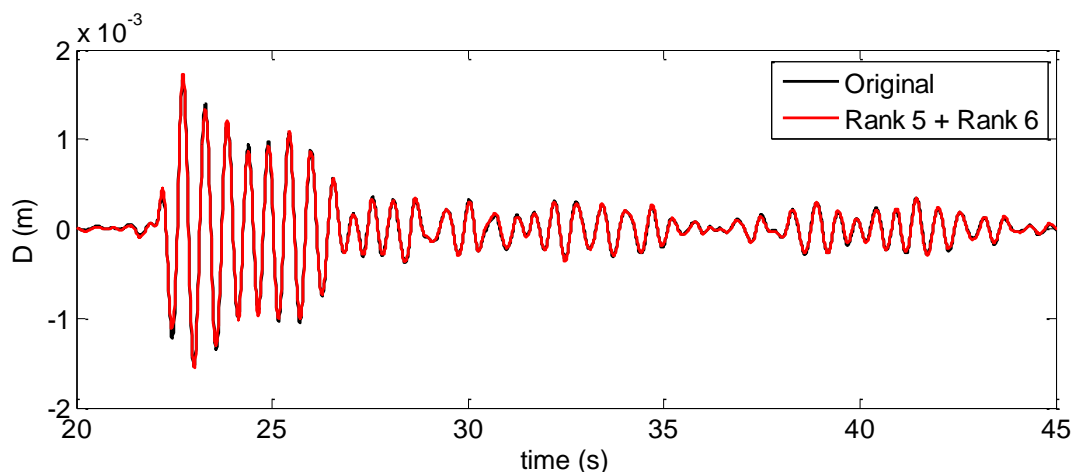
Fig. 2.3 Original signal S and component signals of Rank5 + Rank6

Just as shown in Figure 2.2, Figure 2.3 and Table 2.1, the major components of the example original signal lie on the Rank 5 (1.563Hz $\sim$ 3.125 Hz) and Rank 6 (0.781 Hz $\sim$ 1.563 Hz), while the other components of Rank 1 $\sim$ Rank 4 (high-frequency components, higher than 1.563Hz) and Rank 7 $\sim$ Rank 13 (low-frequency components, lower than 0.781Hz) are little enough to be neglected. Needless to say, the WTT technique can help find the big picture of the earthquake response of a building, which can be accepted as the fundamental responses.

2.4.2 Fundamental response

It has already been known that WTT can separate an original signal into different components. The next problem is how to define and judge the fundamental response of a measurement earthquake response of a building, which will be used for drawing $S_a - S_d$ curve. Fundamental response should be defined in two aspects: firstly, fundamental response should be corresponding to the first-mode (fundamental mode) response, which the higher mode effect should be deleted; secondly, the influence of noise effect on

the fundamental response is very small which can be neglected. Nevertheless, general knowledge and experience tell that earthquake input with the main frequency near the first resonant frequency of the building will cause the maximum response of the building, which will cause the structural damage. That gives a reasonable explanation that the WTT technique can be applied to the both sides of the Equation (2.1), which can be rewritten as follows

$$\mathbf{WTT} \; \{ \; [M]\{\ddot{U}\} + [C]\{\dot{U}\} + [K]\{U\} \; \} = \mathbf{WTT} \; \{ \; -[M]\{l\}\ddot{u}_g(t) \; \} \qquad (2.37)$$

Then equation (2.37) can be rewritten for the first-mode response as follows

$$\mathbf{WTT} \; \{ \; [M]\{\ddot{u}_1(t)\} + [C]\{\dot{u}_1(t)\} + [K]\{u_1(t)\} \; \} \; = \mathbf{WTT} \; \{ \; -\{s_1\}\ddot{u}_g(t) \; \} \; (2.38)$$

Equation (2.27), for calculating representative displacement, will be changed as follows

$$S_d = \frac{\sum m_i \cdot u_{i1}{}^f}{M_e} \qquad (2.39)$$

And equation (2.33), for calculating base-shear force coefficient, will be rewritten as

$$S_a = \frac{\sum_{i=1}^{N} m_i \ddot{u}_{i1}{}^f}{M_e} + \ddot{u}_g{}^f \qquad (2.40)$$

Where $u_{i1}{}^f(t)$ and $\ddot{u}_g{}^f(t)$ are fundamental response and fundamental input obtained through the WTT technique. Then $S_a - S_d$ curve can be calculated through the fundamental responses, extracted using WTT technique.

Nowadays, the judgment of fundamental response is based on two methods: one is based on transfer function[4], see Figure 2.4. In this method, firstly the fundamental frequency of the building is calculated through transfer

function; secondly, the fundamental frequency can be located in a specific rank, for example the fundamental frequency was located in Rank 5 in Figure 2.4; thirdly, at least three ranks (two neighborhood ranks Rank 4 and Rank 6, and one main component Rank 5, see Figure 2.4) were selected as the fundamental response.

The other one is based on Fourier spectrum of component signals, see Figure 2.5. As for this method, the Fourier Amplitude spectrums of component signals and original signal are compared in a same diagram, then one or two components (Rank 5 only, or Rank 5 and Rank 6, for example Figure 2.5) which are as strong as the original signal will be selected as the fundamental response.

Both methods need artificial judgment to determine the fundamental response, so the selected choices of the ranks are not solitary and different researchers have different selections. However, it is regarded that all the reasonable judgments can reach to the almost same results, and the only difference is the accuracy (which can be controlled, because it is easy to get $S_a - S_d$ curves based on different choices and the accuracy could be evaluated).

In this research, we used the second method (Figure 2.5) to judge the fundamental response; and it was assumed that the only one or two component signals are enough to stand for the fundamental response.

In order to realize the automatic selection of the fundamental response in the future, a concept of 'Energy' of the signal may be employed. The basic thought is as follows: (1) definition of the concept of 'Energy'. Generally, the

energy can be calculated as follows:

$$E_d = 0.5 \cdot M \cdot v^2 \tag{2.41}$$

Where E_d is the energy (unit: kg$\cdot m^2/s^2$), M is the mass (unit: kg) and v is the velocity (unit: m/s). However, because the mass value of the building is a constant, so I used v^2 (unit: m^2/s^2) to define the 'Energy'. For example we can use the envelope size of the acceleration time history (E, unit: m/s), see Figure 2.6; (2) calculate the envelope sizes of the original data (E_o) and those of the component signals (E_i for Rank i, i=1, ..., N); (3) Compare the differences d_i ($d_i = E_o{}^2 - E_i{}^2$, unit: m^2/s^2), the smallest d_i (for Rank i) corresponds to the fundamental response. As shown in Table 2.2, Rank 5 and Rank 6 contain the fundamental response, and the judgment is same with those by the previous two methods.
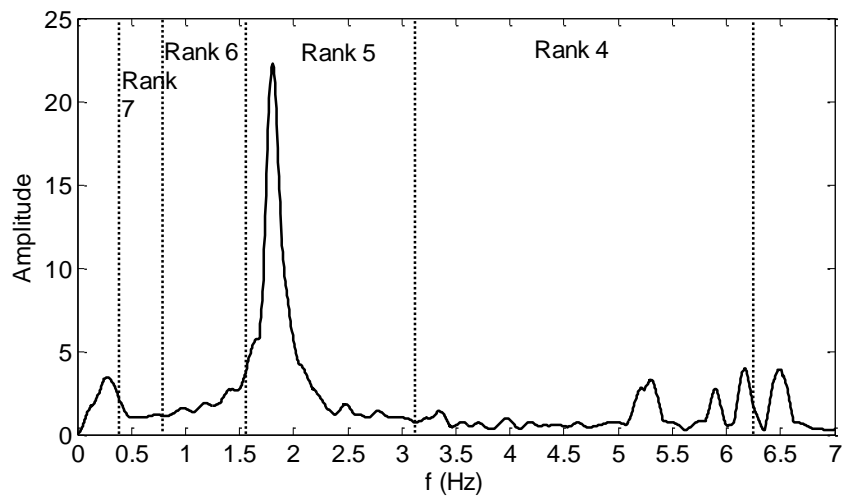
Fig. 2.4 Determination of fundamental response based on Transfer function
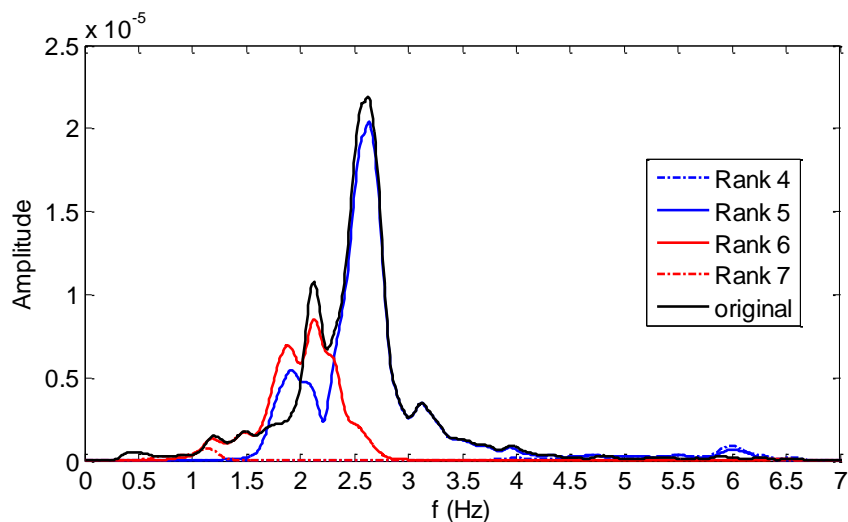
Fig. 2.5 Determination of fundamental response based on Fourier spectrum

of component signals
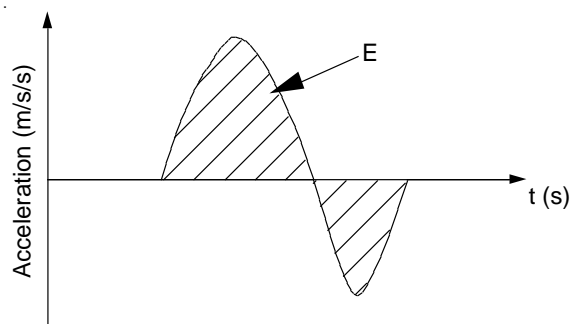
Fig. 2.6 Definition of the concept of 'Energy'

Table 2.2 Automatic selection of the fundamental response for the example in

Figure 2.2

Rank i	$E_i{}^2$ (m^2/s^2)	$E_o{}^2$ (m^2/s^2)	$d_i = E_o{}^2 - E_i{}^2$ (m^2/s^2)	Fundamental response
1	0.00		2.98	No
2	0.01		2.98	
3	0.03		2.95	
4	0.04		2.94	
5	2.50		0.48	Yes
6	0.26		2.73	Yes?
7	0.00	2.98	2.98	No
8	0.00		2.98	
9	0.00		2.98	
10	0.00		2.98	
11	0.00		2.98	
12	0.00		2.98	
13	0.00		2.98	

2.5 Real-Time $S_a - S_d$ curve

Real-Time $S_a - S_d$ curve was firstly brought out by Koichi KUSUNOKI and Masaomi TESHIGAWARA, and the curve could be calculated using the data accumulated by few inexpensive accelerometers installed in a building; the Equations (2.27) and (2.33) give the calculation method of the $S_a - S_d$ curve, while Real-Time $S_a - S_d$ curve emphasizes that the efficiency method should be used to get $S_a - S_d$ curve. The past research mainly focused on the extraction method of the fundamental response and the displacement calculation using accelerations[4, 5, 6]. At the beginning, Butterworth Filter was employed to get the fundamental response and trapezoidal integration method was used to calculate the displacement[5]. Currently, a better signal processing method---Wavelet Transform Technology (WTT) was applied to extract the fundamental response[4, 6]; and a series of shaking table tests were carried to test the possibility of the Real-Time $S_a - S_d$ curve using the measurement data of the real structures. Based on the results of the shaking table test, it can be concluded that Real-Time $S_a - S_d$ curve can be got based on the WTT technique effectively.

2.6 Summary

In this chapter, we reviewed the past research on the performance curve. The basic theory of the Real-Time $S_a - S_d$ curve was also introduced briefly, and the important achievement of the past research is the application of WWT technique to get fundamental response. Although the shaking table test has already showed that the Real-Time $S_a - S_d$ curves can be got using the field measurement data, it is necessary to test the applicability of the Real-Time $S_a - S_d$ curves for the real buildings in strong earthquakes. In the following

chapters, we will study the earthquake responses of an 8-story Steel-Reinforced Concrete (SRC) building; and the seismic evaluation of the building will be carried out using Real-Time $S_a - S_d$ curves.

Reference:

1) Anil K. Chopra and Rakesh K. Goel: A modal pushover analysis procedure for estimating seismic demands for buildings, Earthquake Engineering and Structural Dynamics, Vol.31, pp.561-582, 2002.

2) Anil K. Chopra: Dynamics of Structures: Theory and Applications to Earthquake Engineering, Second Edition. Prentice Hall, 2001.

3) Koichi KUSUNOKI, Ahmed Elgamal, Masaomi Teshigawara and Joel P. Conte. Evaluation of Structural Condition Using Wavelet Transforms. 13th World Conference on Earthquake Engineering. October 12-17, 2008, Beijing, China.

4) Koichi Kusunoki, Daiki Hinata, Yuki Hattori, and Akira Tasai: Development of a new method of realtime residual seismic capacity evaluation of existing structures with accelerometers in the case of MDOF system structures, J. Struct. Constr. Eng., AIJ, No. 699, pp. 613–620, 2014.5.

5) Koichi Kusunoki and Masaomi Teshigawara: A New Acceleration Integration Method to Develop a Real-Time Residual Seismic Capacity Evaluation System, J. Struct. Constr. Eng., AIJ, No. 569, pp. 119–126, 2003.7.

6) Manabu Kawamura, Koichi Kusunoki, Miho Yamashita, Yuki Kattori,

Daiki Hinata, Miguel Augusto DIAZ FIGUEROA and Akira Tasai: Study of a New Method to Compute the Performance Curve of Real Structures with Acceleration Sensors in the case of SDOF System Structures, J. Struct. Constr. Eng. AIJ, No.688, pp.1061–1069, 2013.6.

Chapter 3

BRI Annex Building and the Earthquake Responses

3.1 Overview

The research object of this chapter is a kind of Eight-Story Steel-Reinforced Concrete building, which has already been installed with 11 accelerometers. In this chapter, I will introduce the outline of the building; and the recorded earthquake responses of the building will also be calculated and analyzed. Transfer function of the building for the past earthquakes was calculated and the fundamental frequency of the building was identified. I found that the fundamental frequency of the building decreased in the past years.

3.2 Introduction of the BRI Annex building and the measurement outline

The BRI annex building is an eight-story SRC building with a base floor underground (B1F). The building is supported by a gravity foundation and connected to the main building through a nonstructural passageway, as shown in Figure 3.1 (a). The height of the building (from the ground level to the 8th floor) is 28 m, and the depth of the underground portion is 8.5 m. An instrument cabin consisting of a steel structure is located on the 8th floor. The building is instrumented with 11 accelerometers, each of which can record accelerations in 3 directions: east–west (taken here to be the X direction), north–south (the Y direction), and up–down (the Z direction). The locations of the measurement points in the building are shown in Figures 3.1(b) and 3.1(c).

3.3 Earthquake response records

A total number of 1,239 earthquake record sets were collected for the annex

building between the year of 1998 and 2012. During the same period, 141 earthquakes with peak ground accelerations (PGA) greater than 10 gal and Japanese Meteorological Agency intensities (IJMA) greater than 1 degree occurred in Japan, and see Table 3.1.

The building experienced the 2011 off the Pacific Coast of Tohoku Earthquake (see Figure 3.2, Magnitude: 9.0 degree, which happened off the coast of Sanriku, Japan at 14:46 JST on Friday, March 11, 2011), and the local PGA=279.3gal (see Figure 3.3), IJMA=5.3 degree for the building.

3.4 Displacements calculated from the measurement data

The sampling frequency of the accelerometers in the building is 100 Hz, and displacements were calculated using the Fourier integration method[1] in this paper. For example, a series of discrete acceleration data $\ddot{x}(r)$ (r =0, 1, 2, 3, ···, N. Sampling frequency is f_{sa}), according to Fourier integration method, the velocity can be calculated as follows:

$$\dot{x}(r) = \sum_{k=0}^{N-1} \frac{1}{j \cdot 2 \cdot \pi \cdot k \cdot f_{sa}/N} \cdot H(k) \cdot X(k) \cdot e^{j \cdot 2 \cdot \pi \cdot k \cdot r/N} \tag{3.0a}$$

The displacement can be calculated as follows:

$$x(r) = \sum_{k=0}^{N-1} \frac{-1}{(2 \cdot \pi \cdot k \cdot f_{sa}/N)^2} \cdot H(k) \cdot X(k) \cdot e^{j \cdot 2 \cdot \pi \cdot k \cdot r/N} \tag{3.0b}$$

Where

$$H(k) = \begin{cases} 1 & f_d \le k \cdot f_{sa}/N \le f_u \\ 0 & \end{cases} \tag{3.0c}$$

Where f_d and f_u are the cutoff frequency (in this dissertation, $f_d = 0.2$Hz and $f_u = 80$Hz), $X(k)$ (k =0, 1, 2, 3, ···, N) is the Fourier coefficients of the signal $\ddot{x}(r)$.

In general, the vertical motions of two points are used to calculate the rocking angle[2), 3)]. However, in this research, three measurement points in the basement were not located on the translational axes, so the vector method, which makes use of three points, was employed to calculate the rocking angle.

## Table 3.1 (a) All the 141 Strong earthquakes happened from 1998 to 2012

Time	Epicenter	Latitude	Longitude	Depth	M	Dist.	PGA	IJMA
1998-06-24 23:52	S Ibaraki Pref.	140.1017	36.1500	68	4.7	3	19.3	2.6
1998-08-29 08:46	Tokyo Bay	140.0317	35.6283	65	5.2	56	10.1	2.1
1999-03-26 08:31	N Ibaraki Pref.	140.6183	36.4467	59	5.0	60	46.3	3.2
1999-04-25 21:27	N Ibaraki Pref.	140.6250	36.4517	59	5.2	61	36.9	3.1
1999-12-27 00:05	S Ibaraki Pref.	139.8567	36.1450	53	4.1	20	11.5	1.6
2000-01-12 11:09	N Ibaraki Pref.	140.5900	36.4467	60	4.3	58	12.0	1.9
2000-04-10 06:30	S Ibaraki Pref.	140.0633	36.1867	55	4.7	6	49.4	3.2
2000-06-03 17:54	NE Chiba Pref.	140.7483	35.6850	48	6.1	79	16.1	2.7
2000-07-21 03:39	Off Ibaraki Pref.	141.1217	36.5250	49	6.4	104	37.9	3.4
2000-08-15 03:54	S Ibaraki Pref.	140.0333	36.1933	55	3.9	8	10.2	1.8
2000-08-21 21:27	S Ibaraki Pref.	139.9417	36.0650	47	3.6	14	11.0	1.3
2001-04-20 01:44	S Ibaraki Pref.	139.7783	36.0783	59	4.0	27	11.8	1.9
2001-05-31 08:59	S Ibaraki Pref.	139.8100	36.1717	56	4.7	24	10.8	1.8
2001-07-20 06:02	S Ibaraki Pref.	139.8150	36.1583	55	5.0	23	21.9	2.3
2001-10-18 06:30	S Ibaraki Pref.	139.8583	36.0833	49	4.4	20	15.7	2.1
2002-02-05 19:57	S Ibaraki Pref.	140.1083	36.1767	69	4.5	6	14.1	1.8
2002-02-12 22:44	Off Ibaraki Pref.	141.0850	36.5850	48	5.7	104	46.8	3.1
2002-06-14 11:42	S Ibaraki Pref.	139.9800	36.2117	57	5.1	12	74.3	3.4
2002-07-13 21:45	S Ibaraki Pref.	140.1267	35.9950	65	4.8	16	14.8	2.4
2002-10-21 01:06	Off Ibaraki Pref.	141.1267	36.3650	50	5.4	98	10.1	2.0
2003-03-13 12:12	S Ibaraki Pref.	139.8583	36.0867	47	5.0	20	31.1	2.9
2003-04-08 04:17	S Ibaraki Pref.	139.9117	36.0683	47	4.6	16	19.0	2.1
2003-05-06 23:48	S Ibaraki Pref.	139.9067	36.0317	46	4.2	19	15.2	2.0
2003-05-12 00:57	S Ibaraki Pref.	140.0883	35.8650	47	5.3	30	17.4	2.4
2003-05-26 18:24	Off Miyagi Pref.	141.6533	38.8167	72	7.1	330	29.2	3.2
2003-08-04 20:57	N Ibaraki Pref.	140.6150	36.4383	58	4.9	59	19.4	2.4
2003-09-20 12:54	S Chiba Pref.	140.3033	35.2150	70	5.8	104	13.7	2.8
2003-11-12 17:26	Off Tokaido	137.0567	33.1700	398	6.5	430	14.9	2.6
2003-11-15 03:43	Off Ibaraki Pref.	141.1683	36.4283	48	5.8	104	21.4	2.9
2004-03-11 11:34	Off Ibaraki Pref.	141.0100	36.3183	48	5.3	87	18.4	2.3
2004-04-04 08:02	Off Ibaraki Pref.	141.1567	36.3867	49	5.8	101	21.2	2.9
2004-07-10 20:07	S Ibaraki Pref.	139.8883	36.0767	48	4.7	18	21.4	2.3
2004-10-06 23:40	S Ibaraki Pref.	140.0917	35.9850	66	5.7	17	54.5	3.8
2004-10-23 17:56	Chuetsu, Niigata Pref.	138.8700	37.2883	13	6.8	168	30.9	3.4
2004-10-23 18:34	Chuetsu, Niigata Pref.	138.9317	37.3033	14	6.5	165	18.1	3.1
2005-02-08 11:29	Off Ibaraki Pref.	140.0850	36.1400	67	4.8	0	22.5	2.4
2005-02-23 21:58	S Ibaraki Pref.	139.8483	36.1067	50	4.4	20	11.0	1.6
2005-04-11 07:22	NE Chiba Pref.	140.6200	35.7267	52	6.1	67	25.9	3.3
2005-06-20 01:15	NW Chiba Pref.	140.6933	35.7333	51	5.6	71	11.3	2.4
2005-07-23 16:34	NW Chiba Pref.	140.1383	35.5817	73	6.0	62	25.8	3.0
2005-07-28 19:15	S Ibaraki Pref.	139.8450	36.1250	51	5.0	21	17.6	2.4
2005-08-16 11:46	Off Miyagi Pref.	142.2783	38.1500	42	7.2	298	29.8	3.3
2005-10-16 16:05	S Ibaraki Pref.	139.9367	36.0383	47	5.1	16	36.7	3.1
2005-10-19 20:44	Off Ibaraki Pref.	141.0417	36.3817	48	6.3	91	40.2	3.5
2005-11-15 06:38	Off Sanriku	144.8883	38.0300	83	7.1	476	11.2	2.2
2005-12-02 21:54	S Ibaraki Pref.	139.8500	36.1333	50	4.2	20	10.8	1.6
2005-12-28 18:46	S Ibaraki Pref.	140.0267	36.1817	53	4.8	7	12.5	1.9
2006-01-14 15:30	S Ibaraki Pref.	140.0267	36.1867	52	4.3	7	14.1	1.9
2006-02-01 20:35	NW Chiba Pref.	140.0033	35.7600	101	5.1	42	13.3	2.3

Table 3.1 (b) All the 141 Strong earthquakes happened from 1998 to 2012

2007-05-08 21:01	S Ibaraki Pref.	139.8900	36.0600	46	4.5	18	15.2	2.0
2007-06-02 14:43	S Ibaraki Pref.	140.0333	36.1333	50	4.6	4	42.4	3.1
2007-07-16 10:13	Off Jochuetsu, Niigata Pref.	138.6083	37.5567	17	6.8	205	19.3	3.6
2007-08-16 04:15	E Off Chiba Pref.	140.5300	35.4433	31	5.3	87	13.9	2.6
2008-03-08 01:54	N Ibaraki Pref.	140.6117	36.4517	57	5.2	60	25.0	2.7
2008-03-09 06:13	S Ibaraki Pref.	139.9483	36.0567	47	4.4	14	17.0	2.0
2008-04-04 19:01	S Ibaraki Pref.	139.8267	36.1200	53	5.0	22	33.1	2.8
2008-05-08 01:02	Off Ibaraki Pref.	141.9483	36.2300	60	6.4	169	12.7	2.5
2008-05-08 01:45	Off Ibaraki Pref.	141.6067	36.2267	51	7.0	138	49.6	3.6
2008-06-14 08:43	S Inland Iwate Pref.	140.8800	39.0283	8	7.2	330	26.2	3.4
2008-07-05 16:49	Off Ibaraki Pref.	140.9517	36.6417	50	4.2	97	13.0	2.1
2008-07-24 00:26	N Coast, Iwate Pref.	141.6350	39.7317	108	6.8	423	16.8	2.6
2008-08-20 15:13	S Ibaraki Pref.	139.9000	36.0567	45	4.6	18	40.6	2.8
2008-08-22 19:59	N Ibaraki Pref.	140.6150	36.4417	56	5.2	60	37.0	3.1
2009-02-01 06:51	Off Ibaraki Pref.	141.2783	36.7167	47	5.8	126	15.1	2.4
2009-08-09 19:55	S Off Tokaido	138.4033	33.1267	333	6.8	368	28.4	3.2
2009-12-18 05:41	S Tochigi Pref.	139.7183	36.3333	78	5.1	39	17.9	2.7
2010-02-22 18:52	N Ibaraki Pref.	140.5767	36.4517	56	4.4	57	11.3	1.9
2010-03-12 16:08	S Ibaraki Pref.	139.8850	36.0500	44	4.2	19	10.9	1.4
2010-03-14 17:08	Off Fukushima Pref.	141.8167	37.7233	40	6.7	235	12.0	2.5
2010-06-13 12:32	Off Fukushima Pref.	141.7950	37.3950	40	6.2	208	15.9	2.5
2010-07-23 06:06	NE Chiba Pref.	140.4850	35.8783	35	4.9	47	16.5	2.5
2010-11-05 19:14	S Ibaraki Pref.	139.8417	36.0617	45	4.6	22	20.6	2.5
2011-03-11 14:46	Off Sanriku	142.8600	38.1033	24	9.0	330	279.3	5.3
2011-03-11 15:06	Off Iwate Pref.	142.3967	39.0417	27	6.4	383	25.0	3.1
2011-03-11 15:15	Off Ibaraki Pref.	141.2650	36.1083	43	7.6	107	151.1	4.7
2011-03-11 16:14	Off Ibaraki Pref.	142.0683	36.5550	20	6.8	185	13.7	2.8
2011-03-11 16:25	Off Sanriku	144.6017	38.0900	46	6.2	457	13.0	3.0
2011-03-11 18:04	Off Ibaraki Pref.	140.9817	36.5367	15	5.4	93	10.4	2.3
2011-03-11 18:19	Off Ibaraki Pref.	140.9617	36.5600	15	5.0	93	10.0	2.0
2011-03-11 22:16	Off Ibaraki Pref.	141.8567	36.4417	20	5.7	164	10.4	2.2
2011-03-11 23:00	Off Ibaraki Pref.	140.9550	36.1833	37	5.4	79	14.1	2.3
2011-03-12 00:13	Off Ibaraki Pref.	142.0283	36.0367	22	6.7	176	12.0	2.7
2011-03-12 22:15	Off Fukushima Pref.	141.4250	37.1967	40	6.2	169	11.2	2.3
2011-03-14 10:02	Off Ibaraki Pref.	141.1250	36.4583	32	6.2	101	25.5	3.3
2011-03-14 15:17	Off Fukushima Pref.	142.4317	37.7233	4	5.3	274	10.0	1.9
2011-03-16 12:52	E Off Chiba Pref.	140.9050	35.8367	10	6.1	82	31.5	3.4
2011-03-16 22:39	S Ibaraki Pref.	140.4333	35.9250	49	5.4	40	14.6	2.7
2011-03-17 21:54	Off Ibaraki Pref.	141.3083	36.7367	47	5.7	129	18.3	2.6
2011-03-19 18:56	N Ibaraki Pref.	140.5700	36.7833	5	6.1	85	80.8	3.9
2011-03-22 18:19	Off Fukushima Pref.	141.9100	37.3150	43	6.4	210	11.5	2.4
2011-03-23 07:12	Hama-dori, Fukushima Pref.	140.7867	37.0833	8	6.0	124	18.7	2.7
2011-03-23 07:34	Hama-dori, Fukushima Pref.	140.7950	37.0967	7	5.5	125	46.2	3.3
2011-04-02 16:55	S Ibaraki Pref.	139.9617	36.2067	54	5.0	13	48.0	3.0
2011-04-06 21:56	N Ibaraki Pref.	140.6017	36.7333	7	4.9	82	15.6	2.4
2011-04-07 23:32	Off Miyagi Pref.	141.9200	38.2033	66	7.2	283	39.4	3.4
2011-04-08 04:46	S Ibaraki Pref.	139.9317	36.0517	44	3.8	16	10.6	1.3
2011-04-09 17:02	S Ibaraki Pref.	140.0900	36.2283	54	4.3	11	17.3	2.2
2011-04-11 17:16	Hama-dori, Fukushima Pref.	140.6717	36.9450	6	7.0	105	118.1	4.6
2011-04-11 17:26	Naka-dori, Fukushima Pref.	140.6217	37.0617	5	5.4	114	14.1	2.3

Table 3.1 (c) All the 141 Strong earthquakes happened from 1998 to 2012

2011-04-11 17:45	Hama-dori, Fukushima Pref.	140.7217	36.9483	7	4.7	108	10.4	1.9
2011-04-11 17:58	Hama-dori, Fukushima Pref.	140.6067	37.0233	10	4.9	110	12.8	2.2
2011-04-11 18:05	Hama-dori, Fukushima Pref.	140.7300	36.9883	12	5.1	112	26.0	2.6
2011-04-11 20:42	N Ibaraki Pref.	140.6333	36.9650	11	5.9	105	41.7	3.3
2011-04-12 14:07	Naka-dori, Fukushima Pref.	140.6433	37.0517	15	6.4	114	39.0	3.5
2011-04-12 17:48	Hama-dori, Fukushima Pref.	140.6883	37.0267	10	4.9	114	11.4	2.2
2011-04-13 10:07	Hama-dori, Fukushima Pref.	140.7067	36.9150	5	5.7	104	37.4	3.3
2011-04-14 07:35	N Ibaraki Pref.	140.5717	36.7783	9	5.1	85	18.1	2.4
2011-04-14 12:08	Hama-dori, Fukushima Pref.	140.7717	36.9833	11	5.4	113	12.3	2.4
2011-04-16 11:19	S Tochigi Pref.	139.9450	36.3400	79	5.9	26	44.5	3.6
2011-04-19 23:10	S Ibaraki Pref.	139.8067	36.1683	53	5.0	24	17.1	2.5
2011-04-21 22:37	E Off Chiba Pref.	140.6850	35.6750	46	6.0	75	17.3	2.9
2011-04-24 12:25	S Ibaraki Pref.	139.8567	36.0700	44	4.1	21	11.5	1.8
2011-04-26 21:12	S Ibaraki Pref.	139.9750	36.0850	46	5.0	10	27.7	2.8
2011-05-20 09:46	E Off Chiba Pref.	141.1750	35.8000	36	5.8	106	11.9	2.7
2011-05-22 07:06	NE Chiba Pref.	140.6433	35.7283	48	5.5	68	18.2	2.9
2011-05-25 09:19	S Ibaraki Pref.	140.1383	35.9233	62	4.5	24	18.0	2.4
2011-06-09 19:38	Off Ibaraki Pref.	140.9700	36.4967	13	5.7	90	17.0	2.6
2011-07-08 03:35	Off Fukushima Pref.	141.1283	37.0967	55	5.6	143	10.7	2.0
2011-07-10 09:57	Off Sanriku	143.5067	38.0317	34	7.3	371	13.5	2.7
2011-07-15 21:01	S Ibaraki Pref.	140.0833	36.1633	66	5.4	4	42.4	3.4
2011-07-25 03:51	Off Fukushima Pref.	141.6267	37.7083	46	6.3	223	12.4	2.4
2011-07-31 03:53	Off Fukushima Pref.	141.2200	36.9017	57	6.5	134	33.1	3.2
2011-08-12 03:22	Off Fukushima Pref.	141.1600	36.9683	52	6.1	134	18.6	2.6
2011-08-15 15:26	S Ibaraki Pref.	140.0800	36.1267	64	4.7	0	10.8	2.0
2011-08-19 00:39	S Ibaraki Pref.	140.0833	36.1517	50	4.0	2	20.2	1.7
2011-08-19 14:36	Off Fukushima Pref.	141.7967	37.6483	51	6.5	228	13.7	2.5
2011-09-10 15:00	Off Ibaraki Pref.	140.6933	36.4283	53	4.8	65	14.4	2.3
2011-09-15 17:00	Off Ibaraki Pref.	141.4833	36.2550	51	6.3	127	14.6	2.7
2011-09-21 22:30	N Ibaraki Pref.	140.5767	36.7367	9	5.2	81	24.6	2.6
2011-11-03 19:34	S Ibaraki Pref.	140.1417	35.9200	62	4.9	24	45.9	3.1
2011-11-20 10:23	N Ibaraki Pref.	140.5867	36.7100	9	5.3	79	13.0	2.2
2012-01-01 14:27	Near Torishima Is.	138.5650	31.4267	397	7.0	542	22.1	3.0
2012-01-17 12:30	S Ibaraki Pref.	139.8600	36.0650	46	4.7	21	14.7	2.0
2012-02-11 10:26	NW Chiba Pref.	139.7883	36.0867	46	4.7	26	14.4	2.1
2012-02-19 14:54	N Ibaraki Pref.	140.5883	36.7500	7	5.2	83	35.3	3.1
2012-02-28 14:20	Off Ibaraki Pref.	140.9667	36.5350	23	5.1	92	18.3	2.8
2012-03-01 07:32	Off Ibaraki Pref.	140.6250	36.4383	56	5.3	60	37.9	3.2
2012-03-08 03:50	S Ibaraki Pref.	139.8650	36.0667	44	4.2	20	18.5	2.1
2012-03-10 02:25	N Ibaraki Pref.	140.6117	36.7167	7	5.4	81	19.4	2.4
2012-03-14 21:05	E Off Chiba Pref.	140.9317	35.7467	15	6.1	88	33.3	3.3
2012-03-16 04:20	S Saitama Pref.	139.5900	35.8800	94	5.3	52	11.7	2.0
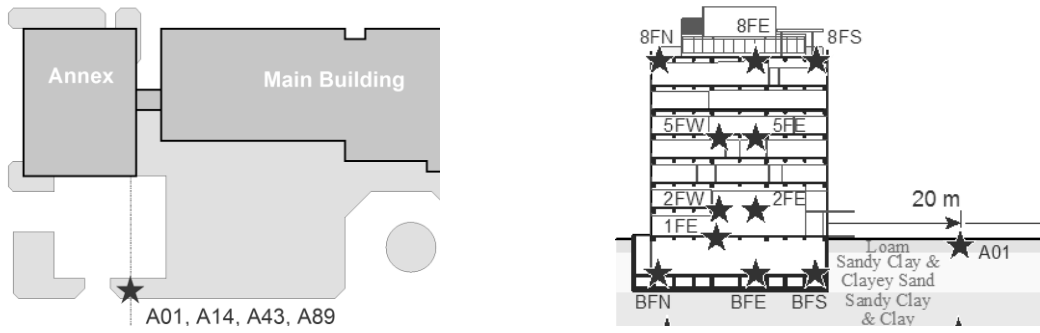
(a) Diagram of the building footprint

(b) Elevation diagram of the measurement points in the building
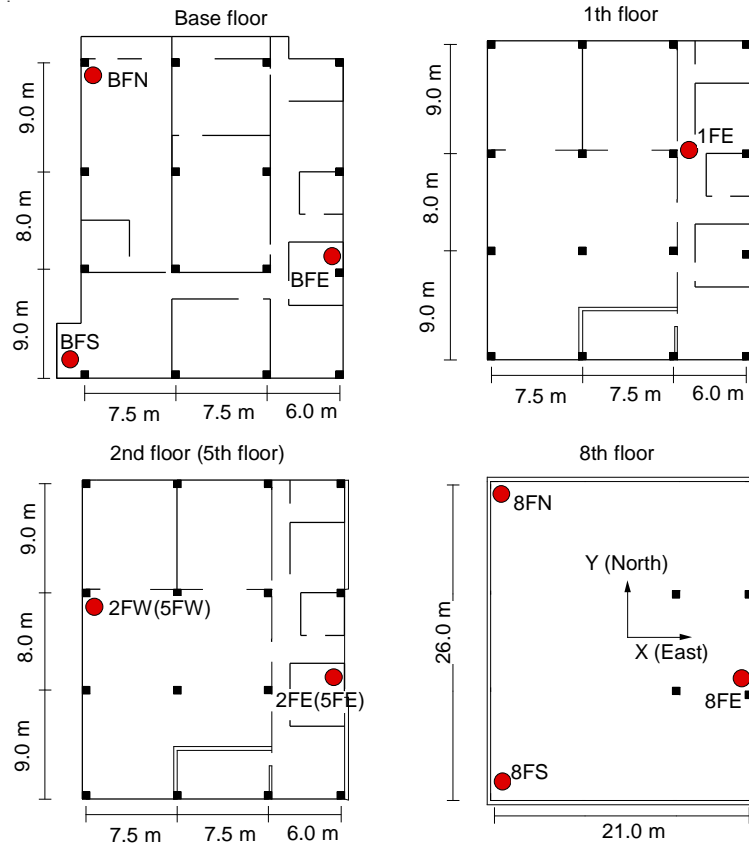
(c) Configuration of the measurement points on floors

Fig. 3.1 Measurement points in the building

Fig. 3.2 Location of the BRI ANX building and the 2011 off the Pacific Coast

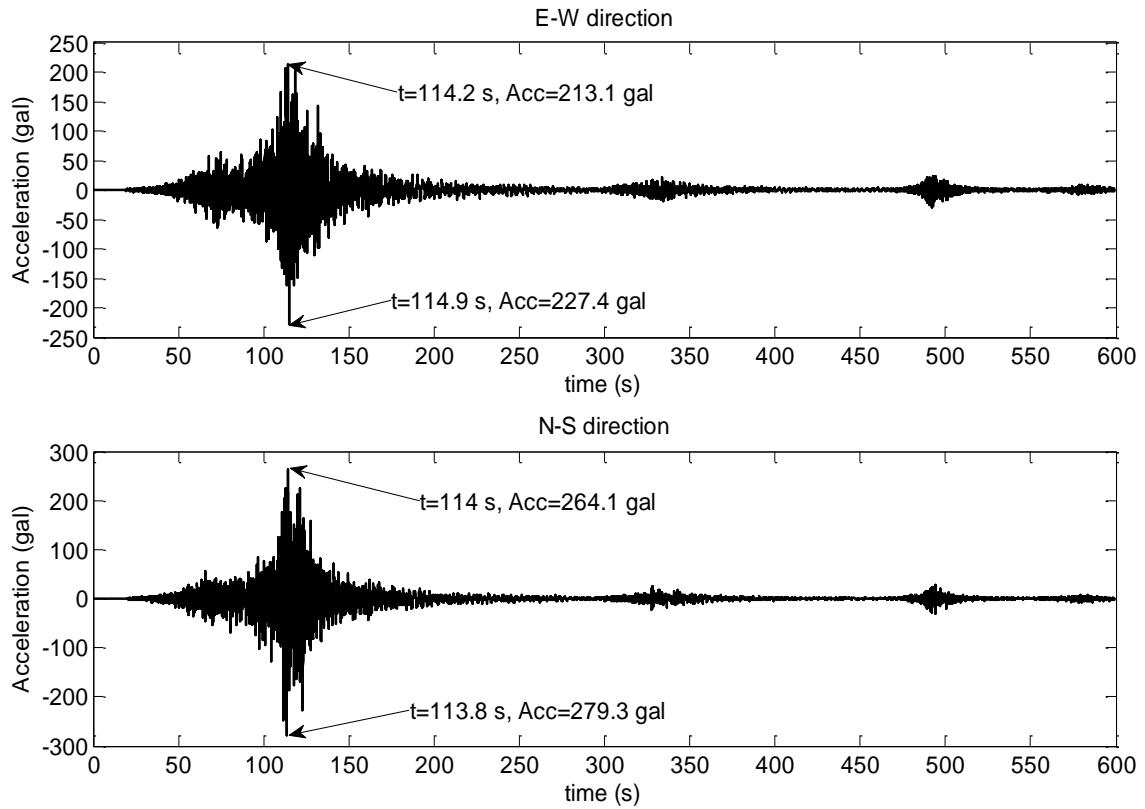of Tohoku Earthquake (Referred to the Google Map)

Fig. 3.3 Recorded local ground motion of BRI ANNEX building for the 2011

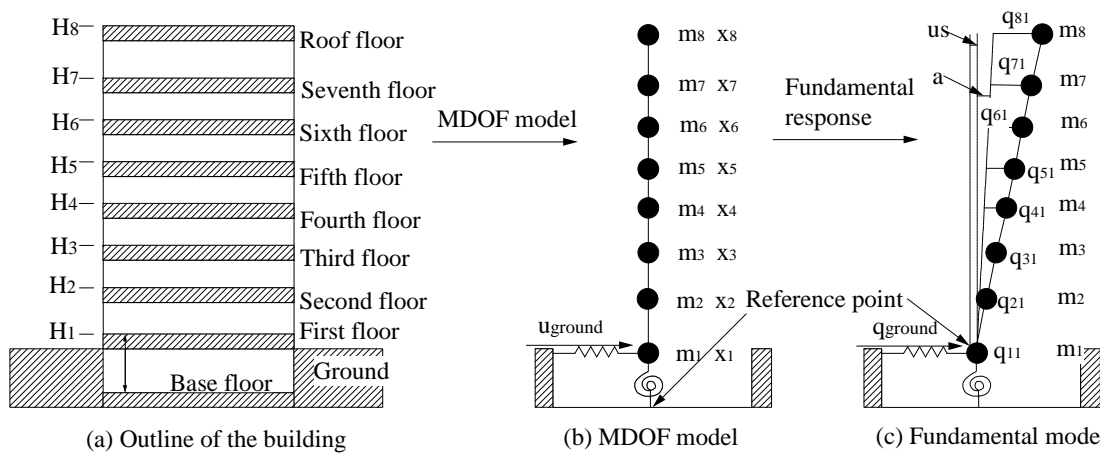off the Pacific Coast of Tohoku Earthquake

(Accelerometers A01 in Figure 3.1 (b))

Fig. 3.4 MDOF model of the building

35

As shown in Figure 3.1(c), BFN, BFE, and BFS are the three points on the base mat. We can calculate the following two vectors:

$$\vec{p} = \overrightarrow{BFN - BFE} \tag{3.1a}$$

$$\vec{q} = \overrightarrow{BFS - BFE} \tag{3.1b}$$

The normal vector of the base mat $\vec{\mathbf{n}} = (x_n, y_n, z_n)$ can be calculated as follows:

$$\vec{\mathbf{n}} = \vec{p} \times \vec{q} \tag{3.2}$$

The normal vector $\vec{\mathbf{n}}$ can be normalized to a length of 1. The rocking angle a is sufficiently small that $\cos a \approx 1$, so $|z_n| \approx 1$. We can easily obtain the rocking angle in the E–W direction, $a_x \approx x_n$, and the rocking angle in the N–S direction, $a_y \approx y_n$.

The lateral fundamental-mode deformation of each floor can be calculated as follows (with a, u_i, and u_0 extracted using WWT):

$$R_{ri} = H_i \times a \tag{3.3a}$$

$$q_{i1} = u_i - u_0 - R_{ri} \tag{3.3b}$$

where R_{ri} is the rocking displacement of the ith floor, H_i is the height of the ith floor, a is the rocking angle, u_i is the measured lateral displacement of the ith floor, u_0 is the measured displacement of the base floor, and q_{i1} is the deformation of the ith floor for the fundamental mode, as shown in Figure 3.4 (c).
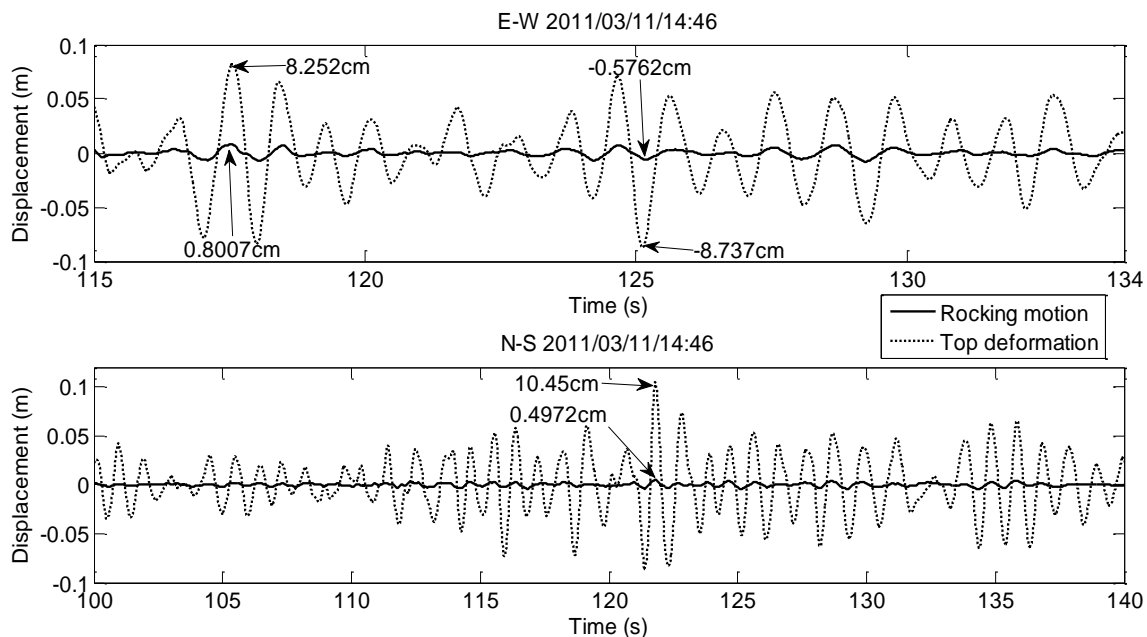
Fig. 3.5 Rocking motion and deformation of the top floor (roof floor) of BRI

ANNEX building for the 2011 off the Pacific Coast of Tohoku Earthquake

The displacements caused by rocking motion (R_{ri}) and swaying motion of the underground basement, also the structural deformation (q_{i1}) of each floor can be calculated directly. Figure 3.5 gives the displacements of rocking motion and displacement of the top floor, which shows that the rocking ratio is about 5%~7%. Based on above calculation for the earthquake response records, rocking motion and structural deformation can be separated and these results will be used for the calculation of the seismic performance curve.

As what is shown in Figure 3.6, for the earthquake responses of the 141 strong earthquakes, the maximum displacements (D_m) of the roof floor are less than 0.018m for the first 70 earthquakes. But the EP earthquake (the 2011 Off the Pacific Coast of Tohoku earthquake happened in 2011/03/11/14:46, the detailed information of the earthquake can be found in

Table 2; in Chapter 4, this earthquake is named as earthquake X08 or Y08; in Chapter 5, this earthquake is named as earthquake E5 for convenience) caused very large roof displacements which reach to about 0.08m~0.11m. Besides, Figure 3.6 shows that stronger earthquakes which are of stronger intensity and higher PGA value cause larger responses.
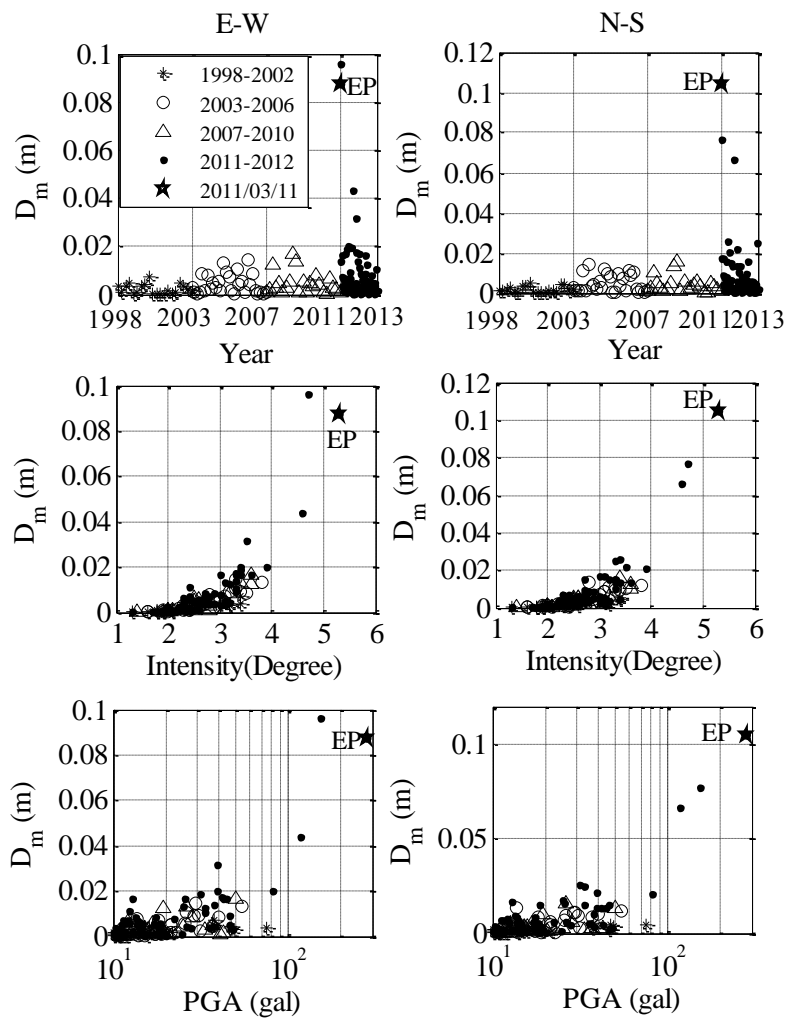
Fig. 3.6 Relationships between the earthquake intensity and maximum roof displacements

3.5 Analysis on the changes of the fundamental frequency using Fourier Transform

Jonathan P. Stewart[4] brought out a method to use the transfer function to calculate the dynamic characteristics of the building considering the SSI effect, and the Transfer Function (TF) is expressed as follows,

$$TF(f) = \frac{\mathcal{F}(roof)}{\mathcal{F}(ground)} \qquad (3.4)$$

As for the transfer function $TF(f)$, fundamental frequency can be picked (Figure 3.7) after the spectrum smoothing technology process (Parzen window function was applied in this paper).
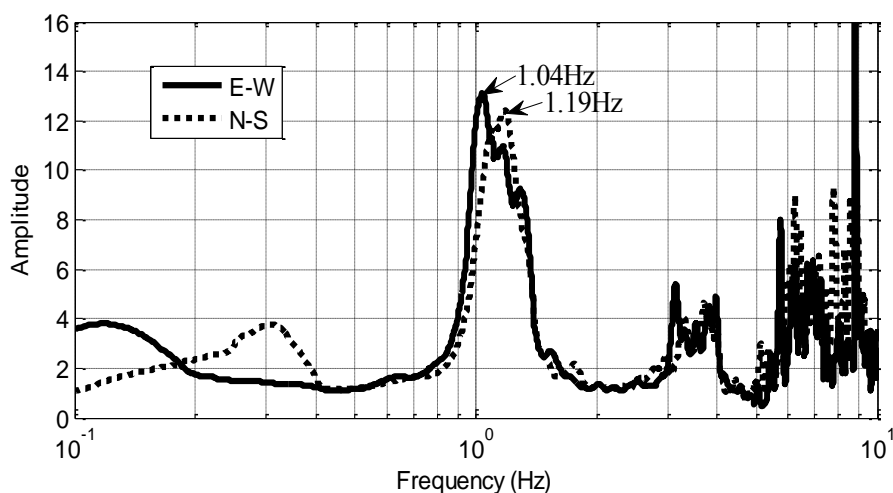
Fig.3.7 Transfer function of Roof to base of BRI ANNEX building

for the 2011 off the Pacific Coast of Tohoku Earthquake
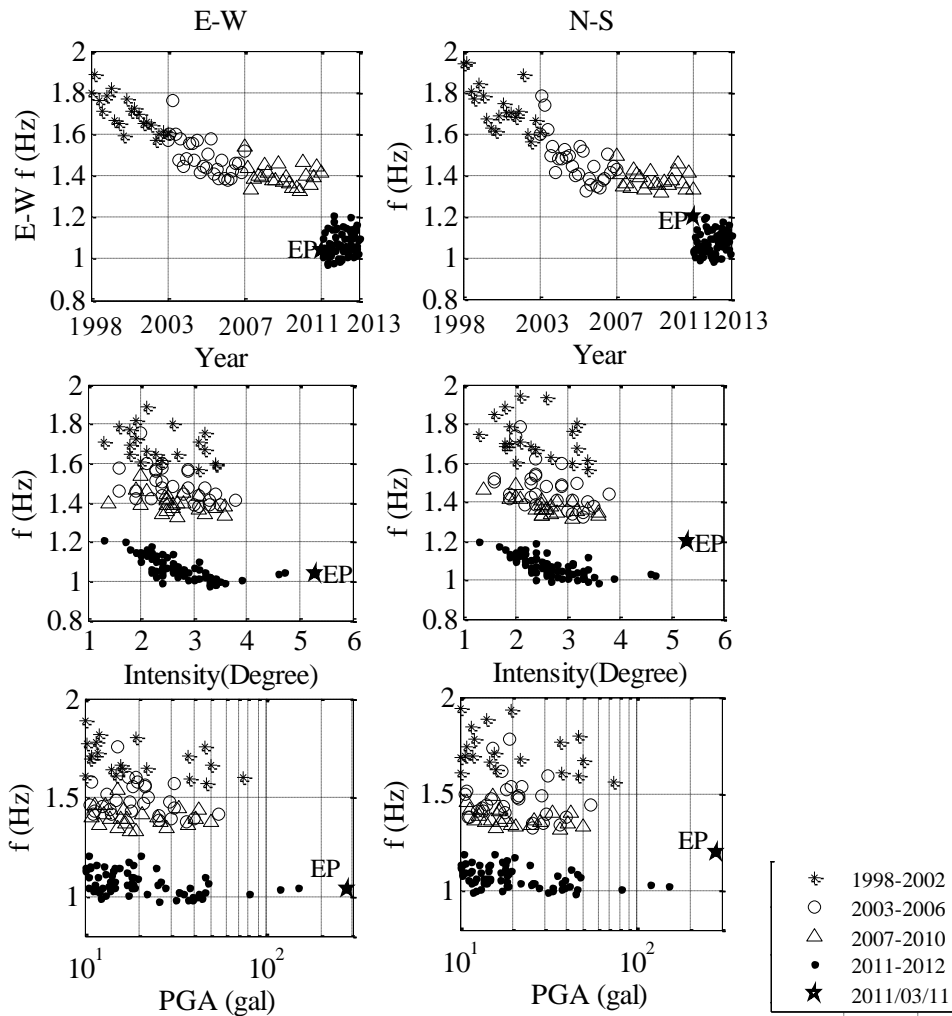
Fig. 3.8 Relationships between the earthquake intensity and frequency

As what is shown in Figure 3.8, the fundamental frequency of the building decreased gradually from about 1.9Hz to 1.3Hz in the first 13 years (1998-2010), and about 70 outstanding earthquakes happened during this period; but in the earthquake EP the fundamental frequency fell down to about 1.02Hz and after this earthquake the fundamental frequency is always in the low level which is less than 1.2Hz for the 71 outstanding earthquakes occurring from 2011/3 to 2012/03. On the other hand, the fundamental

frequency has no correlation with the size of the earthquake intensity and PGA for low level earthquakes (Intensity< 4.0 degree and PGA< 100 gal).

Based on the above analysis, it was found that the fundamental frequency decreased about 32% even experiencing low earthquake responses from $1998 \sim 2010$; while for 2011and 2012, the falling of the fundamental frequency maybe mainly because of the damage caused by the strong earthquake. In order to find what kind of role the earthquake played in the fundamental frequency's decrease, the performance curves of the building calculated through the measurement data will be evaluated in the next chapters.

3.6 Fundamental frequency and rocking effect[4]

For a specific building, it can be supposed that the mass (m) and the height of the building (h) are stable, while the stiffness of the superstructure (k_{sup}) and the rocking stiffness of the soil (k_r) will change. Let ratio between the superstructure and soil is

$$\alpha = \frac{k_{sup}h^2}{k_r} \tag{3.5}$$

And the fundamental circular frequency of the superstructure is as follows,

$$\omega_0 = \sqrt{\frac{k_{sup}}{m}} \tag{3.6}$$

Then the fundamental circular frequency ω_T $(= 2\pi \cdot f$, f is obtained in Figure 3.7) is calculated as follows,

$$\omega = \omega_0 \sqrt{\frac{1}{1+\alpha}} \tag{3.7}$$
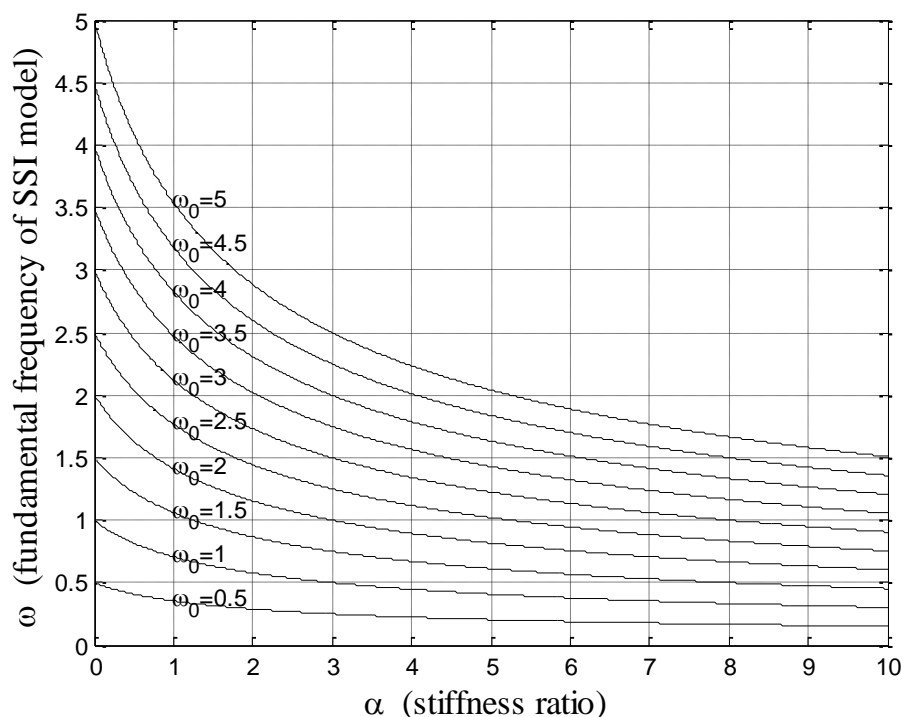
Fig. 3.9 Relationship between ω and α

As shown in Figure 3.9, fundamental frequency of the building is decided by two factors: one is the fundamental frequency of the superstructure (ω_0) and the other one is the stiffness ratio α. Moreover, stiffness of the superstructure k_{sup} and rocking stiffness of the soil k_r are the two significant factors. In this dissertation, I used the performance curves to evaluate the two stiffness values.

3.7 Summary

In this chapter, earthquake response of the building was studied. Displacements were calculated using the acceleration data; the deformation of the superstructure and the rocking motion of the foundation were separated using a simple calculation model. Transfer function was used to analyze the changes of the fundamental frequency during the past strong

earthquakes. It can be concluded as follows:

(1) In the first 13 years, from 1998 to 2010, fundamental frequency of the building decreased gradually from about 1.9 Hz to about 1.3 Hz. However, it seems that the frequency changes have no relationship with the earthquake intensity and PGA.

(2) In the Off the Pacific Coast of Tohoku Earthquake and the following aftershock, the fundamental frequency suddenly decreased from about 1.3Hz to about 1.1Hz, and then the frequency remained stable in the following one year. It seems that the decrease of the fundamental frequency was maybe caused by earthquake damage.

Generally, there are two major influence factors on the changes of the fundamental frequency of the building: one is the superstructure and the other one is the soil. In the following 2 chapters, we will study that what kind of role the earthquake played in the changes of the fundamental frequency. Chapter 4 is to evaluate the earthquake damage of the superstructure using $S_a - S_d$ curve; Chapter 5 is to estimate the soil stiffness using performance curves of the superstructure.

Reference

1) Wang Ji: Application of MATLAB in Vibration Signal Processing, Intellectual Property Publishing House, pp.104-108,2005.

2) Ali Niousha, Yukio Natio, Masao Kan, Atsushi Onouchi and Atsushi Tachibana: System Identification of a Nuclear Reactor Building Under Fixed Base Condition Using Measurement Data, J. Struct. Constr. Eng., AIJ, No. 583, pp. 69–76, 2004.9.

3) Toshihide Kashima and Yoshikazu Kitagawa: Dynamic characteristics of a building estimated from strong motion records using evolution strategy, J. Struct. Constr. Eng., AIJ, No. 602, pp. 145–152, 2006.4.

4) Jonathan P. Stewart and Gregory L. Fenves. System identification for evaluation soil-structure interaction effects in buildings from strong motion recordings. Earthquake Engineering and Structural Dynamics. 27, 869-885, 1998.

Chapter 4
Earthquake Damage Evaluation of the BRI Annex Building Using $S_a - S_d$ Curves

4.1 Introduction

Rapid and quantitative evaluation of earthquake damage is important for seismic retrofit and avoidance of secondary hazards caused by aftershocks. Recent advances in the technology used in accelerometers have made good-quality measurement data available for this purpose. The data recorded by seismic accelerometers installed in buildings have been used in damage evaluation. In addition, damage evaluation methods have been developed to identify both the location and the degree of damage. In general, earthquake damage detection methods are based on monitoring changes in the dynamic characteristics (vibration frequency and modal shapes) of structures [1].

However, it is difficult to understand how the fundamental frequency and seismic capacity of a structure change during an earthquake using methods based on dynamic characteristics. The fundamental frequency does not always reliably reflect the damage condition of a building due to a specific earthquake. Changes in the fundamental frequency are influenced by many factors, such as soil–structure interaction (SSI) effects[2] and the local weather[3] (high temperature, heavy rainfall, and wind). A reduction in the fundamental frequency has been observed even in cases when no damage could be detected with a vibration test[3, 4]. Furthermore, modal shapes are not reliable for use in damage detection[1].

In recent years, a new type of earthquake damage detection method based on wavelet technology and wave propagation has been developed by Maria I. Todorovska and Mihailo D. Trifunac[5), 6), 7)]. In this method, a building is modeled as a layered shear beam, and structural damage can be detected from the distribution of shear and torsional wave velocities, which can be directly related to the structural rigidity along the building's height. The advantages of this method, including its robustness and insensitivity to SSI effects and local weather, over methods based on monitoring changes in the dynamic characteristics have been well described[8)].

An earthquake damage evaluation method based on the $S_a - S_d$ curve (seismic performance curve) concept was developed recently. This method uses wavelet transform technology (WTT) to extract the fundamental mode responses of a structure[9)]. The effectiveness of the $S_a - S_d$ curve approach to assessing the damage caused by large structural deformations has been confirmed in a shaking table test. The measured performance curve largely agreed with the computed curve calculated using WTT[10)]. In contrast to traditional dynamic characteristics-based methods, the $S_a - S_d$ curve method was found to be able to detect changes in the fundamental frequency from small responses to the maximum response and to identify the seismic capacity points of the measured building.

 However, there has been little applied research on how to use $S_a - S_d$ curves to evaluate the seismic capacity of real steel-reinforced concrete (SRC) buildings. In the paper, we present an evaluation strategy for using $S_a - S_d$ curves to evaluate the seismic capacity of real buildings and the

damage suffered by such buildings in real earthquakes. We also describe how to use $S_a - S_d$ curves to explain and evaluate changes in the fundamental frequency of a real building—the Building Research Institute (BRI) annex building (an 8-story SRC building) using earthquake response measurement data. Besides, the observation of the structural damage (such as sizes of the cracks and their distribution) caused by the 2011 off the Pacific Coast Earthquake was also introduced, and the observation results were compared with the $S_a - S_d$ curves.

4.2 The selected strong earthquakes and Earthquake Response Records

In this paper, the 27 strongest of these earthquakes (see Table 4.1) were selected for use in the analysis. The selected 27 earthquakes are contained in the 141 strong earthquake mentioned in chapter 3, and each one is the strongest earthquake in the corresponding years from 1998 to 2012.

In fact, only the motions of the first floor (u_1), the second floor (u_2), the fifth floor (u_5) and the roof floor (u_8) were measured. It is reasonably assumed that the fundamental mode is dominant, so we need to calculate the motions of the other floors by linear interpolation as follows.

$$u_3 = \frac{h_2}{h_2 + h_3 + h_4}(u_5 - u_2) + u_2 \qquad (4.1a)$$

$$u_4 = \frac{h_2 + h_3}{h_2 + h_3 + h_4}(u_5 - u_2) + u_2 \qquad (4.1b)$$

$$u_6 = \frac{h_5}{h_5 + h_6 + h_7}(u_8 - u_5) + u_5 \qquad (4.1c)$$

$$u_7 = \frac{h_5 + h_6}{h_5 + h_6 + h_7}(u_8 - u_5) + u_5 \qquad (4.1d)$$

where h_i is the height of the ith floor. The properties and motions of the

MDOF system are summarized in Table 4.2.

Table 4.1 27 Strong earthquakes occurred in Japan between 1998 and 2012

Time	Epicenter	Latitude	Longitude	Depth (Km)	M (Degree)	Dist. (Km)	PGA (gal)	IJMA (Degree)	Fundamental response	
									E-W	N-S
1998/06/24 23:52	S Ibaraki Pref.	140.1017	36.1500	68	4.7	3	19.3	2.6	rank5	rank5
1998/08/29 08:46	Tokyo Bay	140.0317	35.6283	65	5.2	56	10.1	2.1	rank5	rank5
1999/03/26 08:31	N Ibaraki Pref.	140.6183	36.4467	59	5.0	60	46.3	3.2	rank5	rank5
1999/04/25 21:27	N Ibaraki Pref.	140.6250	36.4517	59	5.2	61	36.9	3.1	rank5+rank6	rank5
2000/04/10 06:30	S Ibaraki Pref.	140.0633	36.1867	55	4.7	6	49.4	3.2	rank6	rank6
2000/06/03 17:54	NE Chiba Pref.	140.7483	35.6850	48	6.1	79	16.1	2.7	rank6	rank5+rank6
2000/07/21 03:39	Off Ibaraki Pref.	141.1217	36.5250	49	6.4	104	37.9	3.4	rank6	rank6
2003/05/26 18:24	Off Miyagi Pref.	141.6533	38.8167	72	7.1	330	29.2	3.2	rank6	rank6
2003/09/20 12:54	S Chiba Pref.	140.3033	35.2150	70	5.8	104	13.7	2.8	rank6	rank6
2004/10/06 23:40	S Ibaraki Pref.	140.0917	35.9850	66	5.7	17	54.5	3.8	rank6	rank6
2004/10/23 17:56	Chuetsu, Niigata Pref.	138.8700	37.2883	13	6.8	168	30.9	3.4	rank6	rank6
2004/10/23 18:34	Chuetsu, Niigata Pref.	138.9317	37.3033	14	6.5	165	18.1	3.1	rank6	rank6
2005/04/11 07:22	NE Chiba Pref.	140.6200	35.7267	52	6.1	67	25.9	3.3	rank6	rank6
2005/08/16 11:46	Off Miyagi Pref.	142.2783	38.1500	42	7.2	298	29.8	3.3	rank6	rank6
2005/10/19 20:44	Off Ibaraki Pref.	141.0417	36.3817	48	6.3	91	40.2	3.5	rank6	rank6
2007/07/16 10:13	Off Jochuetsu, Niigata Pref.	138.6083	37.5567	17	6.8	205	19.3	3.6	rank6	rank6
2008/05/08 01:45	Off Ibaraki Pref.	141.6067	36.2267	51	7.0	138	49.6	3.6	rank6	rank6
2008/06/14 08:43	S Inland Iwate Pref.	140.8800	39.0283	8	7.2	330	26.2	3.4	rank6	rank6
2009/08/09 19:55	S Off Tokaido	138.4033	33.1267	333	6.8	368	28.4	3.2	rank6	rank6
2010/03/14 17:08	Off Fukushima Pref.	141.8167	37.7233	40	6.7	235	12.0	2.5	rank6	rank6
2010/06/13 12:32	Off Fukushima Pref.	141.7950	37.3950	40	6.2	208	15.9	2.5	rank6	rank6
2010/11/05 19:14	S Ibaraki Pref.	139.8417	36.0617	45	4.6	22	20.6	2.5	rank6	rank6
2011/03/11 14:46	Off Sanriku	142.8600	38.1033	24	9.0	330	279.3	5.3	rank6	rank6+rank7
2011/03/11 15:15	Off Ibaraki Pref.	141.2650	36.1083	43	7.6	107	151.1	4.7	rank6	rank6
2011/03/19 18:56	N Ibaraki Pref.	140.5700	36.7833	5	6.1	85	80.8	3.9	rank6	rank6
2011/04/11 17:16	Hama-dori, Fukushima Pref.	140.6717	36.9450	6	7.0	105	118.1	4.6	rank6+rank7	rank6+rank7
2012/03/14 21:05	E Off Chiba Pref.	140.9317	35.7467	15	6.1	88	33.3	3.3	rank6+rank7	rank6+rank7
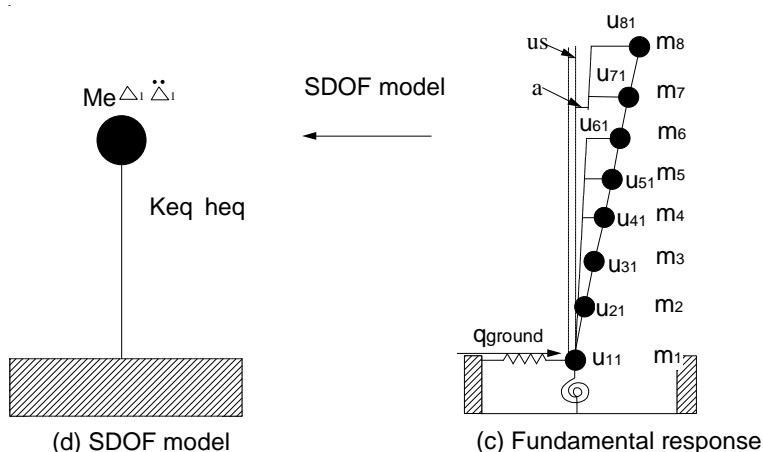
Fig. 4.1 MDOF model simplified to an SDOF model

Table 4.2 Masses, fundamental displacements and heights corresponding to

floors of the MDOF system

i	Mass m_i (10^6kg)	u_i (m)	u_{i1} (m)	H_i (m)
8	1.12	u_8	u_{81}	34
7	0.74	u_7	u_{71}	28.9
6	0.77	u_6	u_{61}	25.2
5	0.93	u_5	u_{51}	21.5
4	0.78	u_4	u_{41}	17.8
3	0.78	u_3	u_{31}	14.1
2	0.84	u_2	u_{21}	10.3
1	1.26	u_1	u_{11}	6

4.3 Damage Evaluation Strategy Using $S_a - S_d$ Curves

4.3.1 Seismic performance curve ($S_a - S_d$ curve) [14]

For the BRI annex building, the representative displacement S_d was calculated using the deformation of the superstructure (Equation (4.2a)). The base shear force coefficient S_a was calculated using Equation (4.2b). The base shear force Q_B was calculated using Equation (4.4).

$$S_d = \Delta_1 \cdot \frac{\sum m_i}{M_e} \qquad (4.2a)$$

$$S_a = \frac{Q_B}{M_e} + \ddot{q}_{ground} \qquad (4.2b)$$

$$\Delta_1 = \frac{\sum m_i \cdot u_{i1}}{\sum m_i} \qquad (4.3)$$

$$Q_B = \sum m_i \cdot \ddot{u}_i \qquad (4.4)$$

$$M_e = \frac{(\sum m_i \cdot u_{i1max})^2}{\sum m_i \cdot u_{i1max}^2} \qquad (4.5)$$

M_e is the equivalent mass corresponding to the fundamental mode. It is assumed that M_e remained unchanged during a single earthquake and can be calculated (using equation (4.5)) from the maximum response points (q_{i1max}) of the fundamental mode response. Mass ratios $M_e / \sum m_i$ in the range of 0.72 to 0.76 were calculated for the earthquakes considered in this research.

The relationship between S_a and S_d (for the peak response points, for which the damping effect is zero) can be expressed as follows, with ω_f denoting the fundamental circular frequency of the superstructure.

$$S_a = \omega_f{}^2 \cdot S_d \qquad (4.6)$$

The fundamental response (u_{i1}; see Figure 4.1(b)) is calculated using the WTT technique. KOICHI KUSUNOKI & MASAOMI TESHIGAWARA[9] have presented the method for using WTT to calculate the fundamental response. As Figure 4.2 shows, the original response can be decomposed into components that contain different frequency range signals). Rank6 and Rank7 reflect the fundamental response of the building to the earthquake that occurred at 2011/03/11/14:46. This fundamental response can be used to calculate the $S_a - S_d$ curve (Equation (4.2)). A performance skeleton curve that reflects changes in the seismic performance from small responses to the maximum response can then be obtained[10], as shown in Figure 4.3.
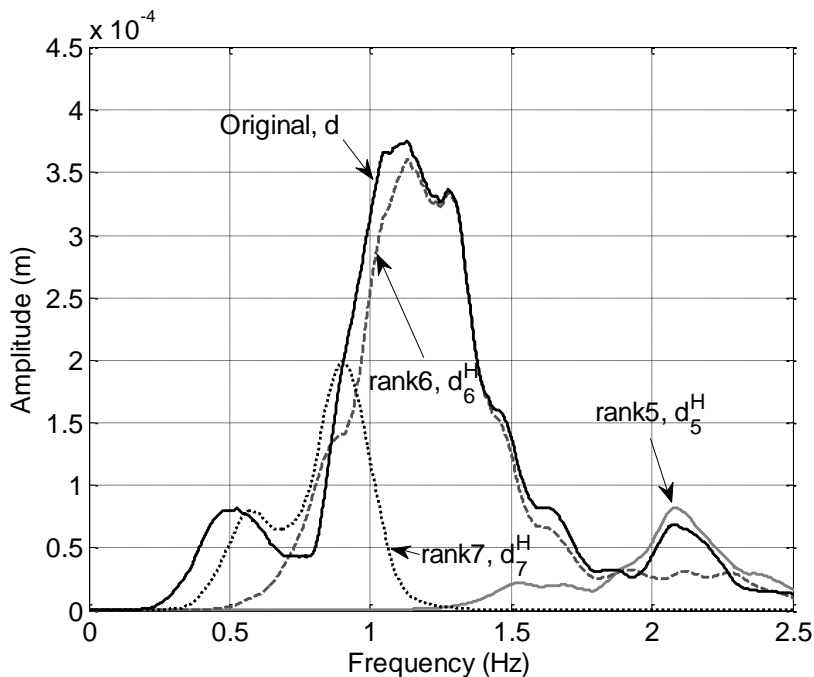
Fig. 4.2 Fourier spectrum of each component of the roof floor displacement

for the 2011 off the Pacific Coast of Tohoku Earthquake in N-S direction
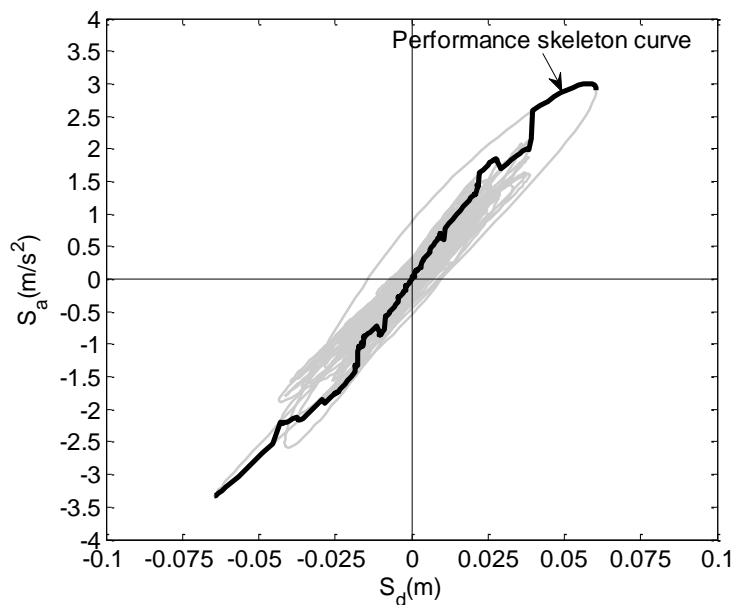
Fig. 4.3 Performance curve using Rank6 and Rank7 for Figure 3 as the

fundamental

4.3.2 The proposed Damage Evaluation Strategy

One of the objectives of this research was to use the $S_a - S_d$ curve to determine whether the building was damaged in past earthquakes. And $S_a - S_d$ curves for the building for strong earthquakes were calculated using WWT and SDOF model theory (Figure 4.5 and Figure 4.6). However, there are two problems associated with using $S_a - S_d$ curves for damage detection: (1) it is difficult to determine the initial stiffness of the $S_a - S_d$ curve and (2) the velocity effect (the damping force) is contained in the $S_a - S_d$ curve. To overcome these problems, we established the following analysis strategy.

Step 1: Calculate the performance skeleton curve $(S_a - S_d$ curve) using earthquake response measurement data collected during the earthquake, according to the method described in section 4.3.1.

Step 2: Define the two deformation levels shown in Table 4.3, 1/3200 and 1/200, where D_{ai} is the drift angle of the superstructure and S_{di} is the corresponding representative displacement (calculated using equation (4.2a)). The minimum acceleration recorded by the accelerometers in the building was 1 Gal[11]; therefore, the drift angle 1/3200 rad (S_{d1} =0.0056 m for the building) is accurate and sufficiently small for the first level. The second-level 1/200 rad is larger than the maximum response for the earthquake shown in Figure 4.7 (for example, the maximum S_d is 0.065 m, which is less than S_{d2} =0.0891 m).
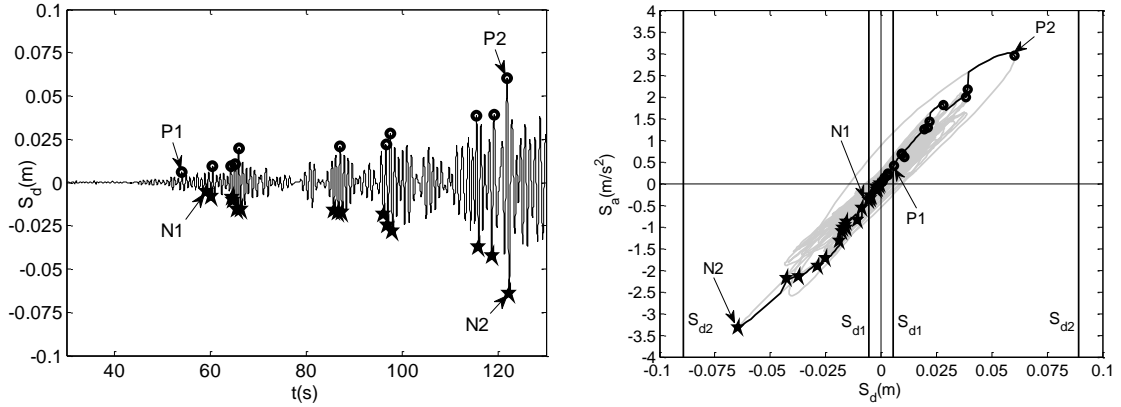
(a) Peak response points   (b) Peak response points in the $S_a - S_d$ curve
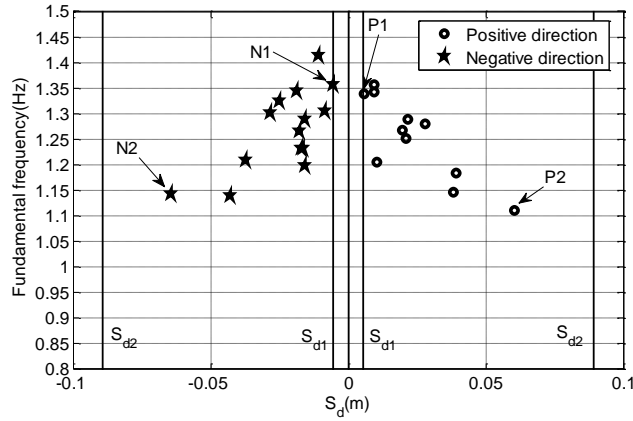
(c) Fundamental frequencies for the peak response points

Fig. 4.4 Damage assessment using the $S_a - S_d$ curve for the 2011

earthquake off the Pacific Coast of Tohoku Earthquake in N-S

Table 4.3 Deformation level for the $S_a - S_d$ curve of the BRI annex building

Level (i)	1	2
D_{ai} (rad)	$\dfrac{1}{3200}$	$\dfrac{1}{200}$
Height of the building (m)	28	
S_{di} (10^{-3}m)	5.6	89.1

Step 3: Select the peak response points inside or outside the deformation level 1 (S_{d1}) as the "initial points"—for example, N1 and P1 in Figure 4.4. The maximum peak response points (N2 and P2 in Figure 4.4) are selected as the "final points". The fundamental frequencies of the "initial points" and the "final points" are compared to assess whether damage occurred. As Figure 4.4(c) shows, the fundamental frequency decreased from approximately 1.35 Hz to approximately 1.1 Hz, which means that earthquake damage occurred.

In this research, some large earthquakes (E–W direction: X01–X11, N–S direction: Y01–Y04, YA–YD and Y08–Y11; see Figure 4.7) with larger S_d values than those of the neighborhood earthquakes were studied using the damage evaluation strategy mentioned above.

4.4 The identified decrease of seismic performance and the earthquake damage

Using the $S_a - S_d$ curve evaluation strategy described in section 4.3, $S_a - S_d$ curves for several strong earthquakes were developed and are shown in Figure 4.5 (E–W direction) and Figure 4.6 (N–S direction). The fundamental frequencies calculated using the "initial points" (for example, N1 and P1 defined in Figure 4.4) and "final points" (for example, N2 and P2 defined in Figure 4.4) of the $S_a - S_d$ curve (where "Positive direction" refers to the points in the positive direction and "Negative direction" refers to the points in the negative direction) are summarized in Figure 4.8. For smaller earthquakes whose maximum representative displacement S_d is less than S_{d1} (for example, X01–X04, Y01–Y03, YA, and YB), we calculated the

fundamental frequency using the maximum response points only. For larger earthquakes (such as X05–X11, Y04, YC, YD, and Y08–Y11), we used the points ("initial points" and "final points") described previously. However, for the earthquake X09 or Y09, which was an aftershock that occurred approximately 30 minutes after the earthquake X08 or Y08, only the maximum response points were used to calculate the fundamental frequency. For the E–W direction, it is found that earthquake damage might have occurred in earthquake X08 (X09 was the aftershock of X08. The fundamental frequency decreased from approximately 1.30 Hz to 1.09 Hz (see Figure 4.8 (a), X08 and X09), as shown by the $S_a - S_d$ curve and Figure 4.5 (c) (X08 and X09). We also found that no severe earthquake damage occurred in the other earthquakes considered, such as X01–X07, X10, and X11.

For the N–S direction, it is found that earthquake damage occurred in earthquake Y08 (the fundamental frequency decreased from approximately 1.35 Hz to 1.05 Hz (see Figure 4.8(b), Y08 and Y09 and Figure 4.6(c), Y08 and Y09). It is also found that no severe earthquake damage occurred in the other earthquakes considered, such as Y01–Y04, YA–YD, Y10, and Y11.
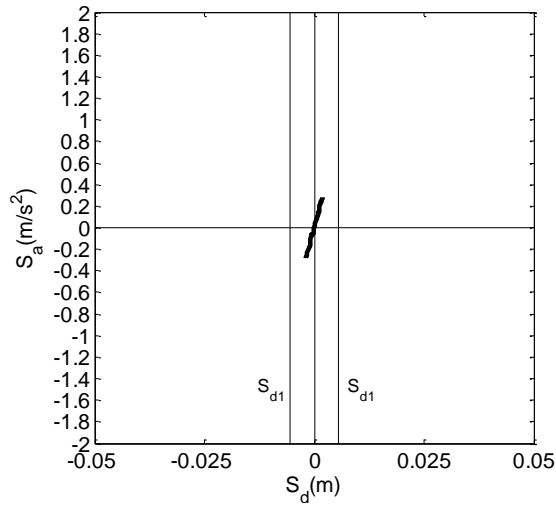
(a) X01
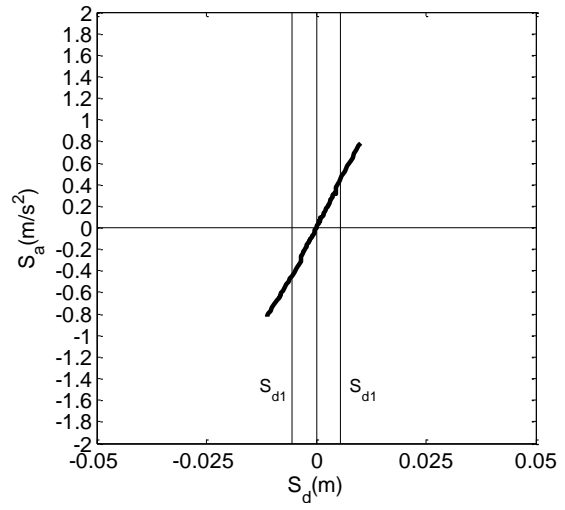
(b) X07
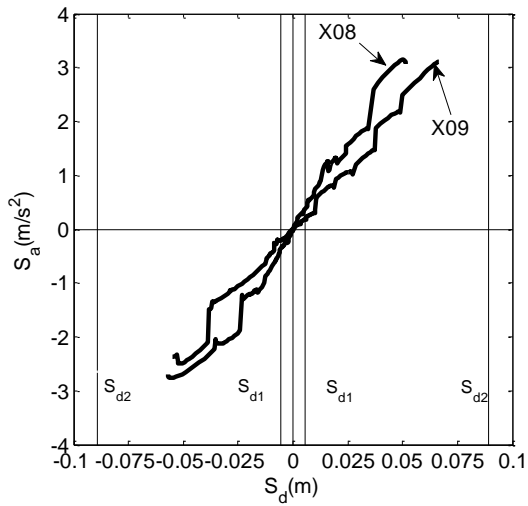
(c) X08 and X09
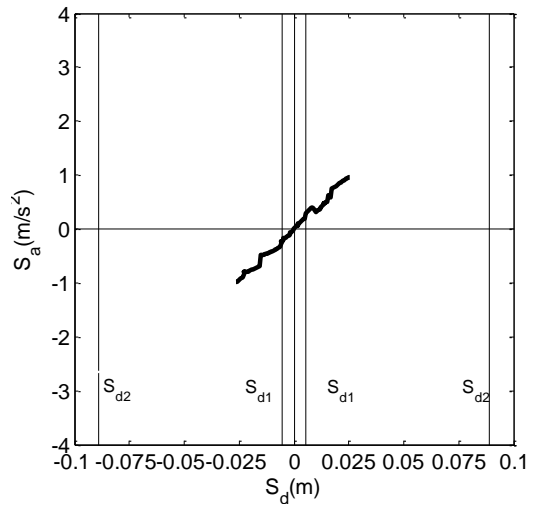
(d) X10

Fig. 4.5 Comparison of $S_a - S_d$ curves in the E–W direction

(a) Y01

(b) YD

(c) Y08 and Y09

(d) Y10
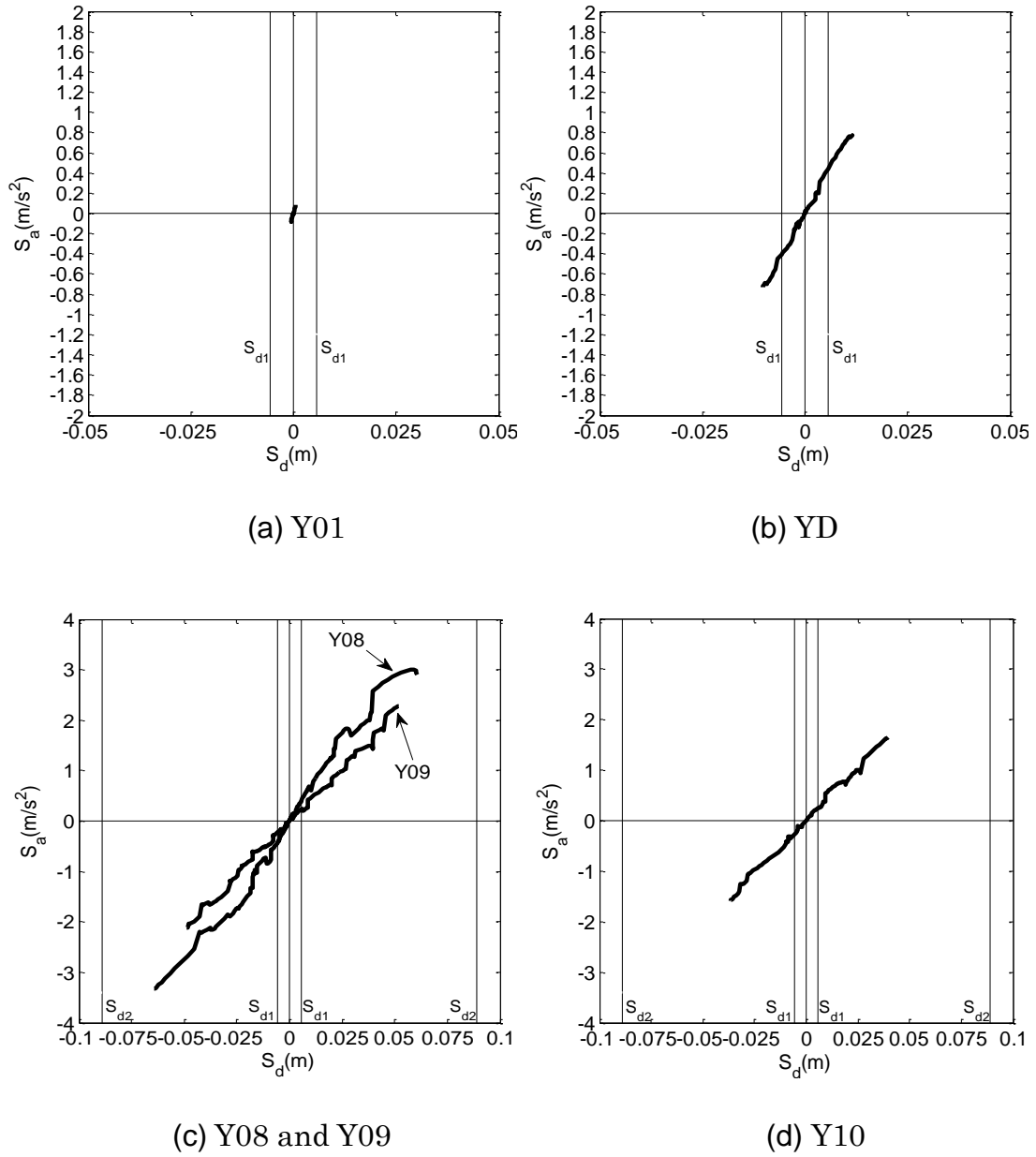
Fig. 4.6 Comparison of $S_a - S_d$ curves in the N–S direction

Overall, the fundamental frequency decreased from approximately 1.9 Hz to approximately 1 Hz (a decrease of approximately 47.4%), but the decrease in the fundamental frequency caused by earthquake damage was only approximately 11.1% in the E–W direction and 16.32% in the N–S direction. For some smaller earthquakes (X01–X07, X10, and X11; Y01–Y04, YA–YD, Y10, and Y11), the $S_a - S_d$ curves (Figures 4.5 (a) and (b) and Figures 4.6 (a) and (b)) are linear. However, the $S_a - S_d$ curves for these earthquakes show that the seismic capacity of the superstructure decreased substantially, as shown in Figure 4.8. The fundamental frequency decreased from approximately 1.9 Hz to approximately 1.36 Hz in the E–W and 1.30 Hz in the N–S direction between 1998 and 2010 (as Figure 4.5 (a)(b) and Figure 4.6 (a)(b) show, the $S_a - S_d$ curves are linear), which is consistent with the results calculated by Kashima[11]. We conclude that the decrease in the superstructure stiffness (the fundamental frequency) over this time period was not caused by severe earthquake damage but other unknown reasons such as material aging.
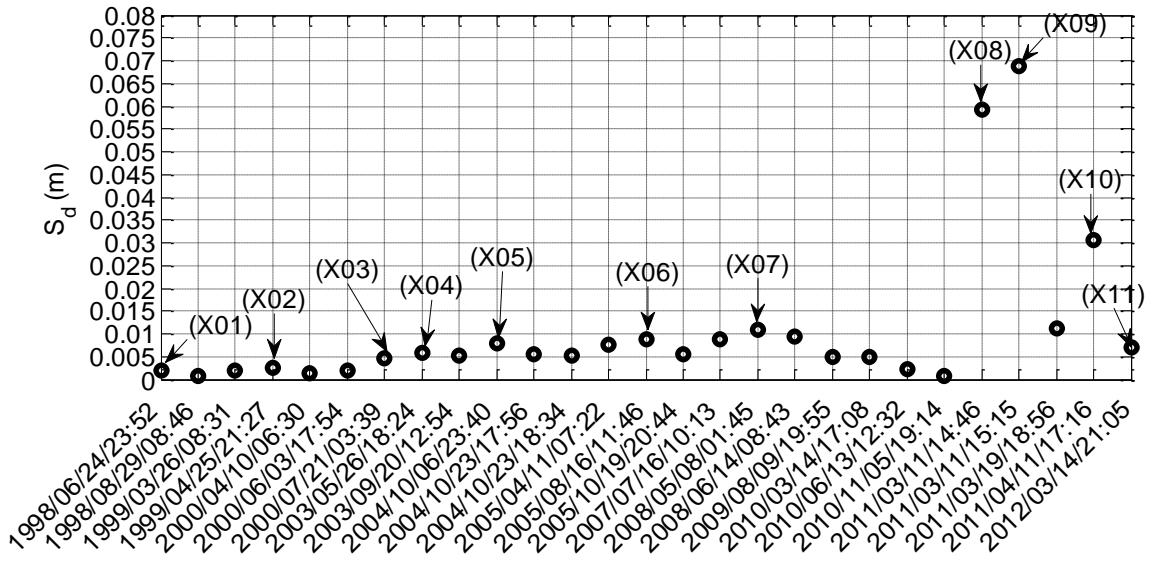
(a) E-W direction S_d
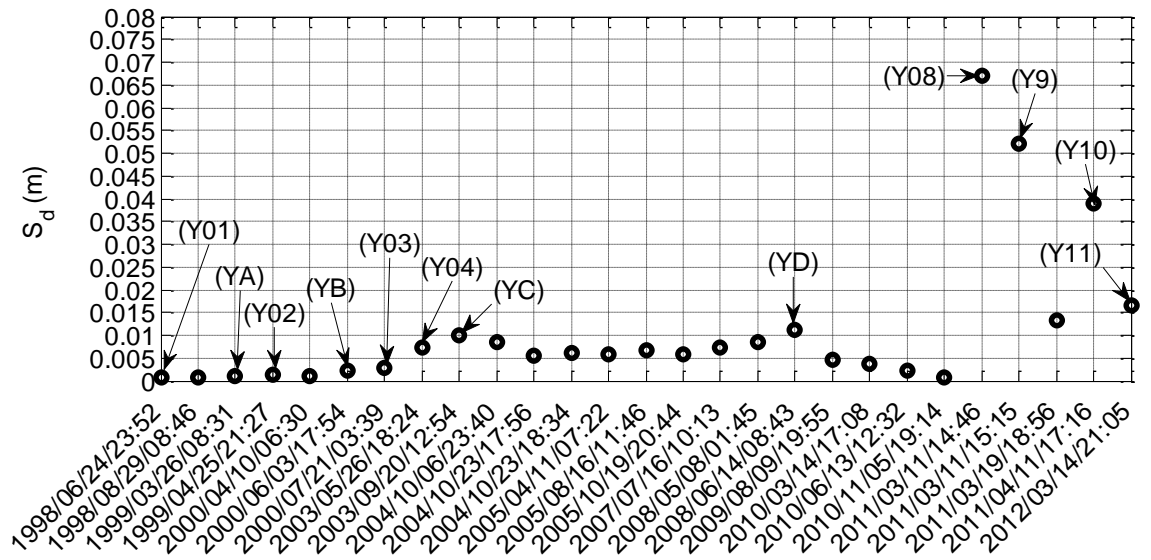
(b) N-S direction S_d

Fig. 4.7 S_d for 27 strong earthquakes
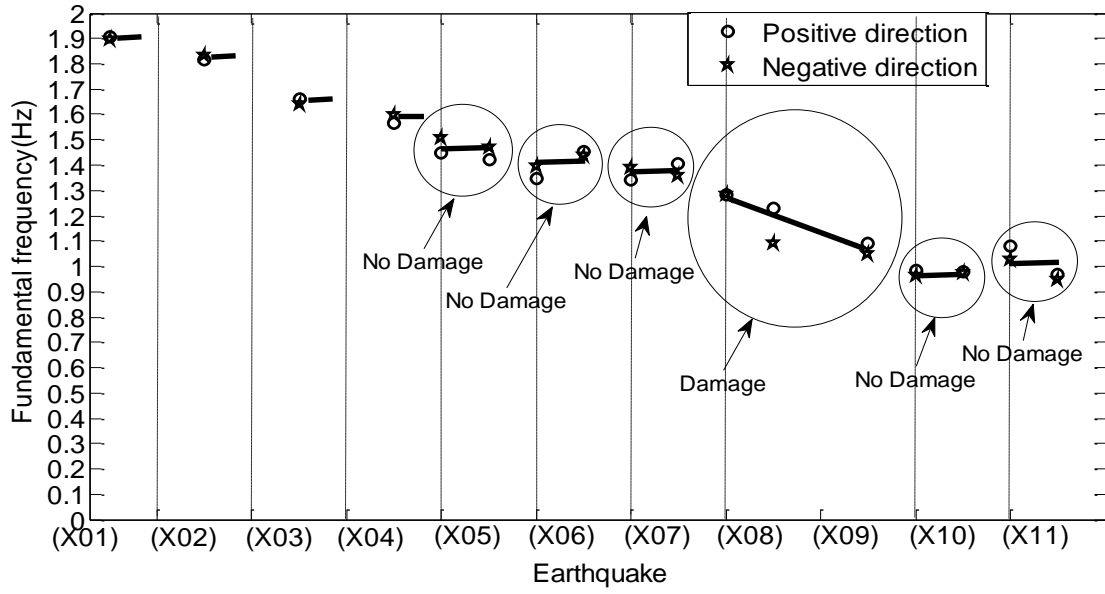
(a) Damage judgment in E-W direction
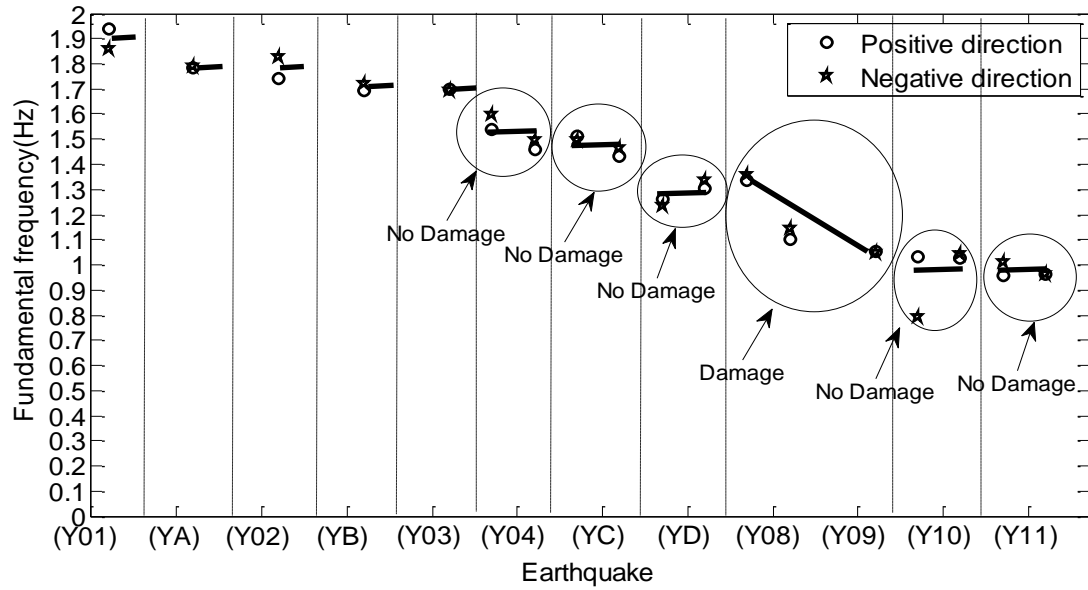
(b) Damage judgment in N-S direction

Fig. 4.8 Evaluation of $S_a - S_d$ curves

4.5 Influence of the rocking effect on $S_a - S_d$ curve

The method of simplifying the MDOF model to SDOF model is the foundation of the seismic performance curve. The method based on rigid-foundation has been given out [2]. While for BRI annex building, the influence of rocking effect was quite large. In this paper, in order to evaluate the influence of rocking motion on the performance curve, representative displacement S_d was calculated based on two cases: case 1, S_d was calculated based on rigid foundation model, which means only the deformations of superstructure (u_{i1}) were used; case 2, S_d was calculated based on flexible foundation model (mainly for rocking motion), which means not only the deformation of superstructure but the rocking motion (u_{ri}).

Case 1: for rigid foundation model

$$\Delta_1 = \frac{\sum m_i \cdot u_{i1}}{\sum m_i} \qquad (4.7)$$

Case 2: for flexible foundation model

$$\Delta_1 = \frac{\sum m_i \cdot (u_{i1} + u_{ri})}{\sum m_i} \qquad (4.8)$$

And the $S_a - S_d$ curve can be calculated using equations (4.2 a) and (4.2 b). The base-shear force coefficient S_a is same for both cases.

Just as what is shown in Figure 4.9, the influence of the rocking effect on $S_a - S_d$ curve is not large, and the earthquake damage evaluation can be carried out in both cases.

E-W direction

N-S direction
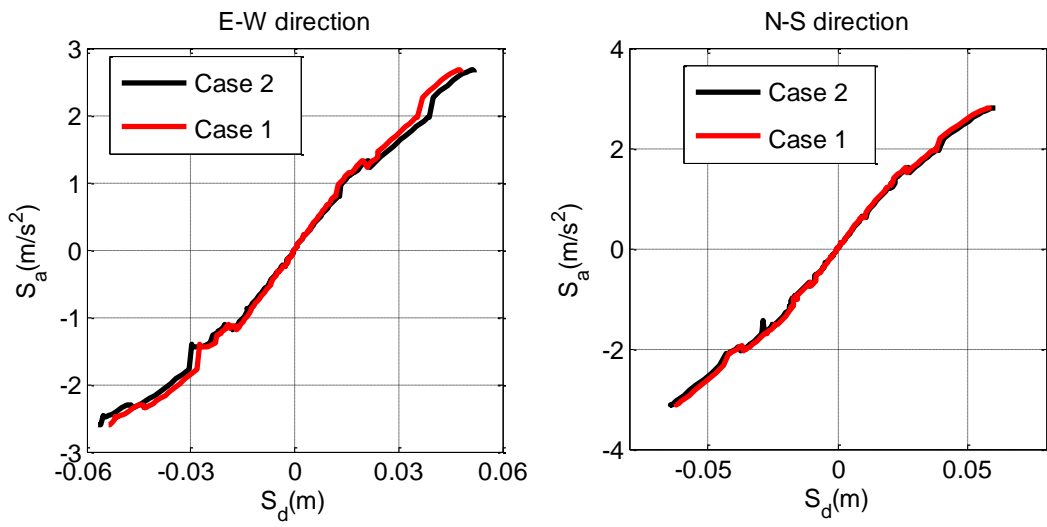
Fig. 4.9 Influence of rocking effect on residual seismic capacity curve
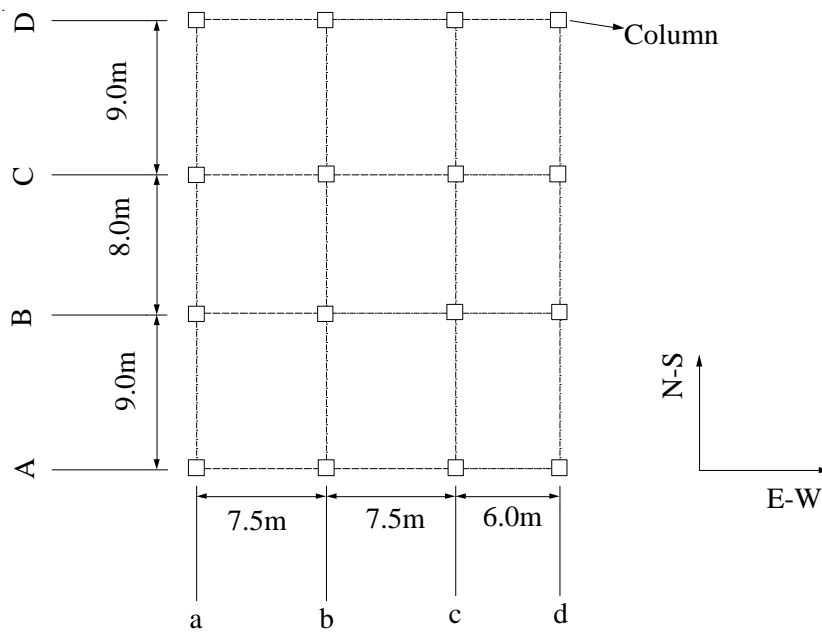
Fig. 4.10 (a) Distribution of the columns in plan
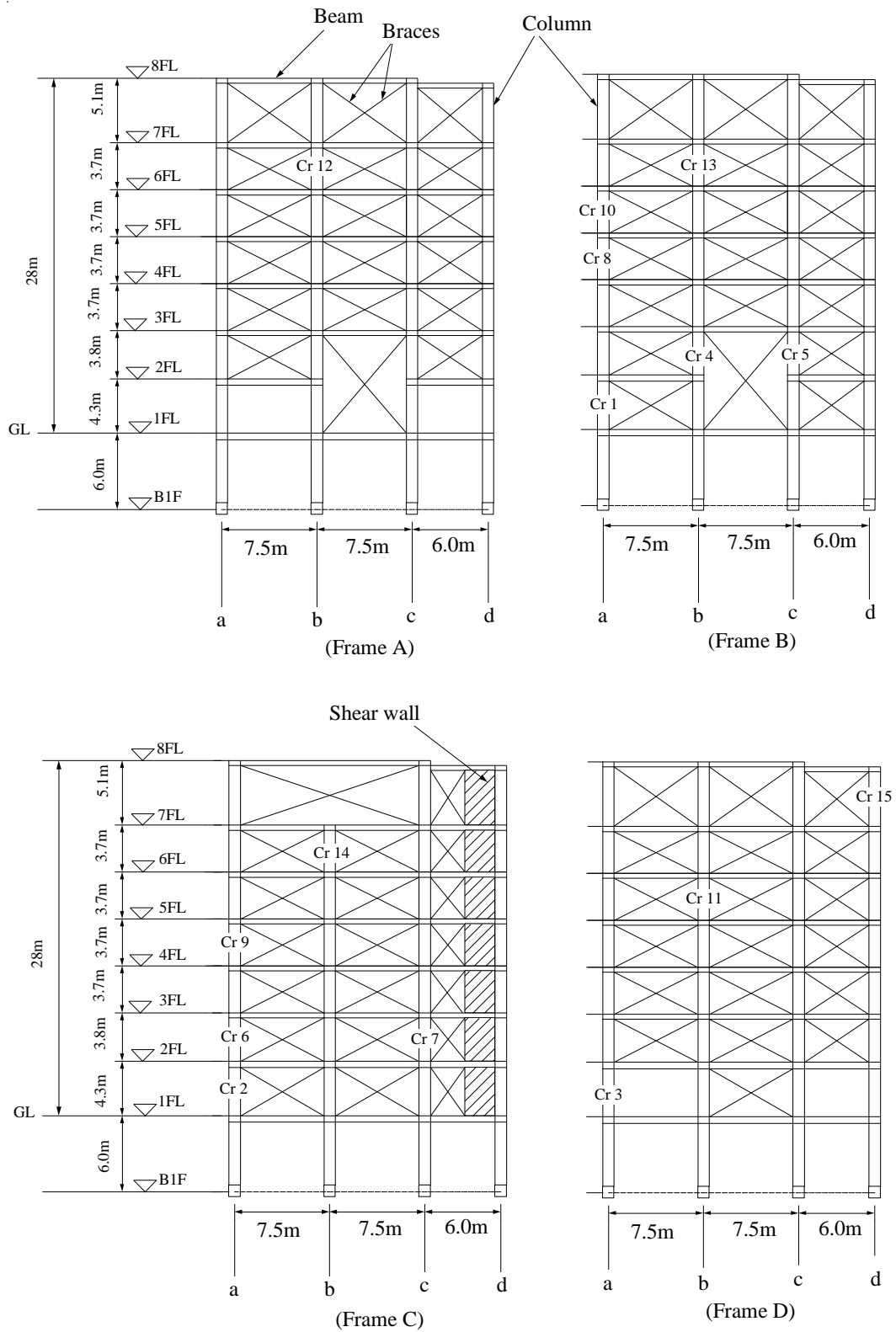
Fig. 4.10 (b) Distribution of the cracks in columns (Cr 1 ~ Cr 15 means the outstanding cracks occurred in the columns)

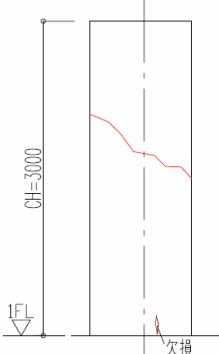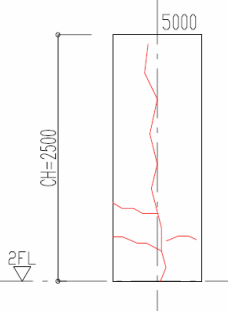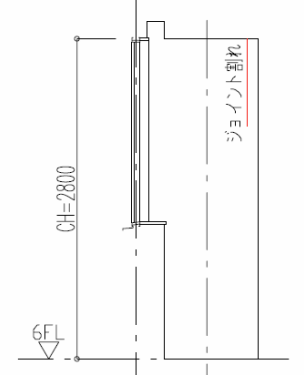Table 4.3(a) Detailed images of the Cracks (0.2mm ~ 0.8mm) on columns
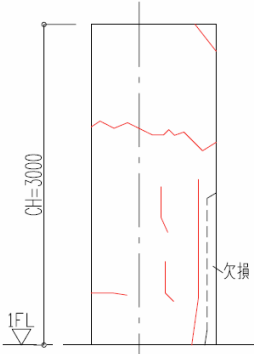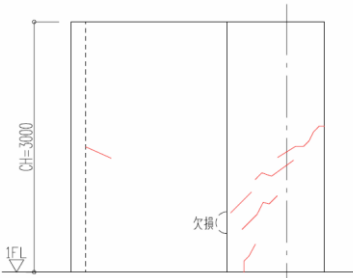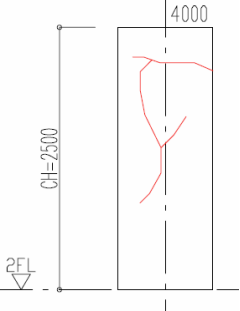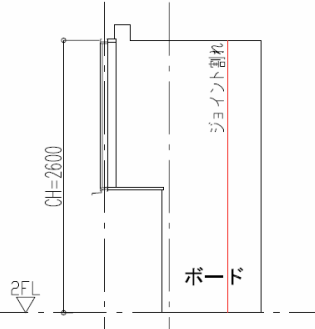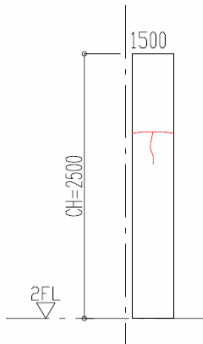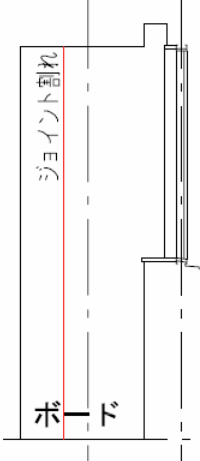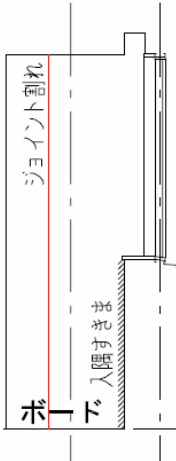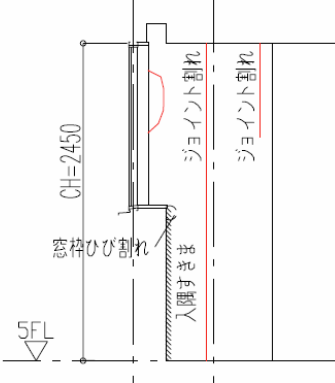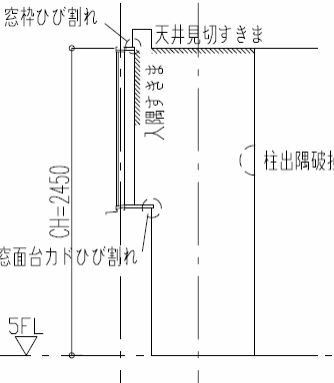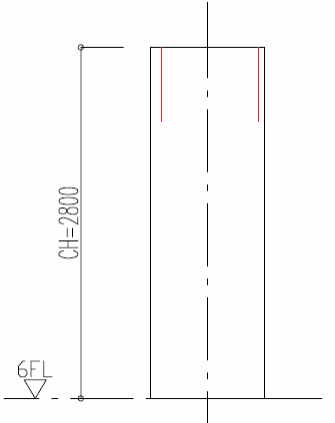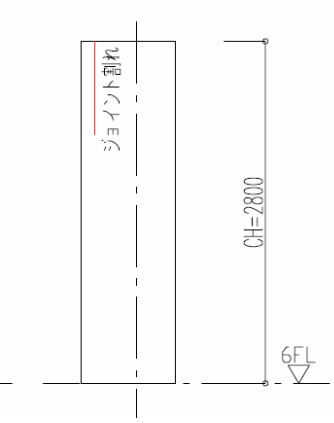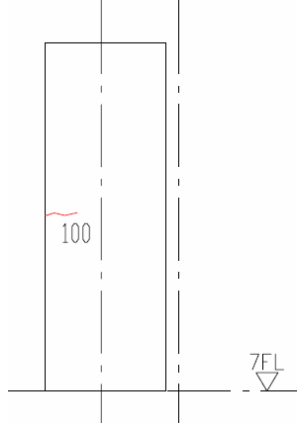
Cr 1 (Column B-a, 1FL)	Cr 2(Column C-a, 1FL)	Cr 3(Column D-a, 1FL)
Cr 4(Column B-b, 2FL)	Cr 5(Column B-c, 2FL)	Cr 6(Column C-a, 2FL)
Cr 7(Column C-c, 2FL)	Cr 8(Column B-a, 4FL)	Cr9(Column C-a, 4FL)

Table 4.3(b) Detailed images of the Cracks (0.2mm ~ 0.8mm) on columns

Cr 10(Column B-a, 5FL)	Cr 11(Column D-b, 5FL)	Cr 12(Column A-b, 6FL)
Cr 13(Column B-b, 6FL)	Cr 14(Column C-b, 6FL)	Cr 15(Column D-d, 7FL)

4.6 Comparison between observation structural damage and $S_a - S_d$ curve

4.6.1 Observed structural damage

The frame structure of the BRI Annex building is made up with three kinds of structural elements: columns, braces and shear walls (made of the steel reinforced concrete), see Figure 4.10. After the 2011 Off the Pacific Coast of Tohoku Earthquake, happened in 2011.03.11, the earthquake damage survey of the building was carried out. Damaged portions (Cracks: width is about 0.2mm ~ 0.8mm) on the columns of the superstructure were observed, see Table 4.3 (a) and (b). As shown in Figure 4.10 (b), cracks happened only on the 15columns of the total columns of 96. Besides, much more cracks happened in the non-structural elements (we did not discussed here), such as boards. Totally, according to the observation results of the cracks, no severe damage happened to the structure during the earthquake.

4.6.2 Residual seismic capacity ratio index R and $S_a - S_d$ curve

Although there was no severe earthquake damage in the structure, it is necessary to know the numerical expression of the damage level. Residual seismic capacity ratio index,R, can help us to understand the damage level and residual seismic capacity of the building. According to the Guidelines for Post-Earthquake Damage Evaluation and Rehabilitation of RC Buildings in Japan[15], the damage classification of the columns with cracks (shown in Figure 4.10(b)) is Damage Class Ⅱ (visible clear cracks on concrete surface, crack width is about 0.2mm ~ 1.0mm). Then the index R can be simply calculated, which is $R = 0.97 > 0.95$. So the superstructure was evaluated as slightly damaged in the earthquake.

Correspondingly, the $S_a - S_d$ curve of the superstructure during the

earthquake shows that the stiffness decreased to the 70% of the initial value before the earthquake, see Figures 4.5 (c), 4.6 (c) and 4.8.

In a word, both methods mentioned above can express the earthquake damage level of the superstructure during the 2011 Off the Pacific Coast of Tohoku Earthquake. Although the residual seismic capacity ratio index R showed that superstructure was slightly damaged, the $S_a - S_d$ curve showed that stiffness of the superstructure lost about 30%. However, compared with the index R, the $S_a - S_d$ curve can be obtained quickly right after an earthquake. Moreover, the $S_a - S_d$ curve was calculated using field measurement data while the index R was calculated using the observation results by engineers, so it can be concluded that the $S_a - S_d$ curve can reflect the global damage of the superstructure than the index R more quickly and convincible.

4.7 Conclusions

The seismic performance curve ($S_a - S_d$ curve) concept was used to evaluate earthquake damage of the real SRC building using the evaluation strategy described in this dissertation. The SSI effects (rocking motion and swaying motion) were eliminated in the calculation of the representative displacement S_d, and fundamental responses were extracted using wavelet transform technology. The conclusions reached can be summarized as follows.

(1) Changes in $S_a - S_d$ curves (which reflect changes in seismic capacity) can be observed using measurement data. The fundamental frequency of the

BRI annex building decreased from approximately 1.90 Hz to approximately 1 Hz between 1998 and 2012. This decrease was mainly caused by a decrease in the seismic capacity of the superstructure. The contribution of earthquake damage to the decrease in the fundamental frequency was approximately 11.1% in the E–W direction and 16.32% in the N–S direction. This damage occurred during the earthquake that occurred in 2011 off the Pacific Coast of Tohoku. Although no severe earthquake damage occurred between 1998 and 2010, the fundamental frequency of the superstructure decreased substantially (the superstructure stiffness decreased to approximately 50% of its initial value).

(2) The damage evaluation method based on the $S_a - S_d$ curve concept is simple and practicable. A simplified $S_a - S_d$ curve can help us understand changes that occur in the seismic capacity of a building in real time. Nevertheless, even though linearity or nonlinearity in $S_a - S_d$ curves can be observed, the initial stiffness of the curve is difficult to be derived numerically. Therefore, the damage evaluation strategy presented in this paper is considerably appropriate for cases in which the story drift angle is sufficiently large (for example, when the story drift angle of the building is greater than 1/3200 rad).

(3) The influence of the rocking motion on the $S_a - S_d$ curve of the BRI Annex building was very small for the 2011 off the Pacific Coast of Tohoku.

(4) Compared with the conventional damage observation method, $S_a - S_d$ curve can help us to understand the global structural damage quickly and effectively.

The evaluation method described in this dissertation needs to be adapted to other types of buildings, and its accuracy needs to be refined in the future. The building considered in this dissertation is an 8-story SRC building for which the applicability of the SDOF model is reasonable. For high-rise buildings and irregular buildings, much more complex mechanisms (such as high-mode effects, torsional effects) will influence the earthquake responses. Therefore, the applicability of the $S_a - S_d$ curve method should be evaluated for these types of buildings. In addition, it is possible to determine the damage points using the $S_a - S_d$ curve, and the residual displacements also need to be studied further in the future.

References

1) Peter C. Chang, Alison Flatau and S. C. Liu: Review Paper: Health Monitoring of Civil Infrastructure, Structural Health Monitoring, Vol. 2(3), pp. 257–267, 2003.

2)M. D. Trifunac, S. S. Ivanovic, and M. I. Todorovska: Apparent periods of a building. Ⅰ: Fourier analysis, Journal of Structural Engineering, Vol. 127, No. 5, pp. 517–526, 2001.

3)John F. Clinton, S. Case Bradford, Thomas H. Heaton and Javier Favela: The Observed Wander of the Natural Frequencies in a Structure, Bulletin of the Seismological Society of America, Vol. 96, No. 1, pp. 237–257, 2006. 2.

4)Zbigniew Zembaty, Marcin Kowalski and Stanislav Pospisil: Dynamic identification of a reinforced concrete frame in progressive states of damage, Engineering Structures, Vol. 28, pp. 668–681, 2006.

5)Maria I. Todorovska, Mihailo D. Trifunac: Earthquake damage detection in the imperial Country Service Building Ⅰ：The data and time-frequency analysis, Soil Dynamics and Earthquake Engineering, Vol. 27, pp. 564–576, 2007.

6)Maria I. Todorovska, Mihailo D. Trifunac: Earthquake damage detection in the imperial Country Service Building Ⅱ：Analysis of novelties via wavelets, Structural Control and Health Monitoring, Vol. 17, pp. 895–917, 2010.

7)Maria I. Todorovska, Mihailo D. Trifunac: Earthquake damage detection in the imperial Country Service Building Ⅲ: Analysis of wave travel times via impulse response functions, Soil Dynamics and Earthquake Engineering, Vol. 28, pp. 387–404, 2008.

8)Maria I. Todorovska, M. Rahmani: Recent Advances in Wave Travel Time Based Methodology for Structural Health Monitoring and Early Earthquake Damage Detection in Buildings, 15th World Conference of Earthquake Engineering, LISBOA, 2012.

9)Koichi KUSUNOKI, Ahmed Elgamal, Masaomi Teshigawara and Joel P. Conte: Evaluation of Structural Condition Using Wavelet Transforms, 14th World Conference on Earthquake Engineering, Beijing, China, Paper No.609, 2008.10.

10)Manabu Kawamura, Koichi Kusunoki, Miho Yamashita, Yuki Kattori, Daiki Hinata, Miguel Augusto DIAZ FIGUEROA and Akira Tasai: Study of a New Method to Compute the Performance Curve of Real Structures with Acceleration Sensors in the case of SDOF System Structures, J. Struct. Constr. Eng. AIJ, No.688, pp.1061–1069, 2013.6.

11) Toshihide Kashima and Yoshikazu Kitagawa: Dynamic characteristics of a building estimated from strong motion records using evolution strategy, J. Struct. Constr. Eng., AIJ, No. 602, pp. 145–152, 2006.4.

12) Toshihide Kashima: Dynamic behavior of an eight-story SRC building examined from strong motion recordings, 13th World Conference on Earthquake Engineering Vancouver, B. C., Canada, Paper No. 196, 2004.

13) Ali Niousha, Yukio Natio, Masao Kan, Atsushi Onouchi and Atsushi Tachibana: System Identification of a Nuclear Reactor Building Under Fixed Base Condition Using Measurement Data, J. Struct. Constr. Eng., AIJ, No. 583, pp. 69–76, 2004.9.

14) Koichi Kusunoki and Masaomi Teshigawara: A New Acceleration Integration Method to Develop a Real-Time Residual Seismic Capacity Evaluation System, J. Struct. Constr. Eng., AIJ, No. 569, pp. 119–126, 2003.7.

15) Yoshiaki NAKANO, Masaki MAEDA, Hiroshi KURAMOTO and Masaya MURAKAMI: GUIDELINES FOR POST-EARTHQUAKE DAMAGE EVALUATION AND REHABILITATION OF RC BUILDINGS IN JAPAN. 13th World Conference on Earthquake Engineering, Paper NO.124, Vancouver, B.C., Canada, August 1-6, 2004.

Chapter 5

Evaluation of Soil Stiffness Using Performance Curves of the BRI Annex Building

5.1 INTRODUCTION

The soil–structure interaction (SSI) effect is one of the important factor that influences the seismic response and dynamic characteristics of a building; the larger the ratio of superstructure stiffness to the stiffness of soil, the larger the SSI effect[1]. Although soil springs can be calculated using the soil properties obtained from the field test survey and experiments before the construction of the building, it is difficult to know the real value of soil springs after the construction of a superstructure, especially after earthquakes occur. Some researchers studied the accuracy of soil springs proposed by current methods in the past years. For example, Tamori and Iiba[2, 3] made the microtromer observations of 20 SRC buildings, and they used the measurement data to calculate the dynamic characteristics of the measured buildings, which were compared with those of the SSI model (swaying and rocking springs of soil were determined by the calculation method of response and limit strength, mass and stiffness of the superstructure were calculated according to the design standard) used at the design stage. Their results indicated that the calculation method of response and limit strength underestimated the rocking stiffness for the buildings with embedment spread foundations. Mori and Fukuwa et al.[4] evaluated the soil springs of the building with a embedment spread foundation using FEM and Layered models based on the dynamic SSI analysis. However, there is

rare research that evaluates the real measurement of the rocking stiffness of soil under earthquakes. This chapter presents the research that tried to solve the problem.

Nowadays, a new seismic evaluation method based on the real-time residual seismic performance curve ($S_a - S_d$ curve) is used to evaluate the seismic performance of superstructures[5–7]. This method has been shown to be practically applicable to seismic performance evaluation of real buildings[8]. It is expected that the concept of the $S_a - S_d$ curve of the Single-Degree-Of-Freedom (SDOF) model can be used to evaluate soil performance (reflected by the $R_a - R_d$ curve of the foundation) in earthquakes.

In this chapter, a simple evaluation method of rocking stiffness of the soil is proposed, which is based on the $R_a - R_d$ curve of the foundation. The $R_a - R_d$ curves were calculated using measurement earthquake response data of an eight-story steel-reinforced concrete (SRC) building with a direct embedment foundation (i.e., the underground soil is layered).

5.2 The Proposed Method for $R_a - R_d$ curve
5.2.1 $R_a - R_d$ curve

The superstructure of the measured building (Figure 5.1(a)) can be simplified down to an equivalent SDOF model, and the $S_a - S_d$ curve (representative displacement S_d and base shear force coefficient S_a) and the equivalent mass m_e of the equivalent SDOF model (refer to Figure 5.1 (b)) can be calculated using the method in the reference papers[7,8].

Generally, rocking motion mainly couples with the fundamental mode[9].

Then the representative rocking-moment coefficient R_a (Equation 5.1(a)) and rotation moment of the foundation M_r (Equation 5.1(b)) for the model in Figure 5.1(b) can be written as follows

$$R_a = \frac{S_a}{H_e} \tag{5.1a}$$

$$M_r = I_e \cdot R_a \tag{5.1b}$$

$$I_e = m_e \cdot H_e{}^2 \tag{5.1c}$$

where the equivalent height H_e (Chopra et al.[10]) was calculated using maximum response points $(u_{i1max}{}^f)$ of the fundamental mode response; see Equation (5.2) as follows:

$$H_e = \frac{\sum m_i \cdot u_{i1max}{}^f \cdot h_i}{\sum m_i \cdot u_{i1max}{}^f} \tag{5.2}$$

Then the dynamic equation for the rocking motion can be written as follows:

$$I_e \cdot R_a + c_R \cdot \dot{R}_d + k_r \cdot R_d = 0 \tag{5.3}$$

where c_R and k_R are the damping and stiffness, respectively, of the soil for the rocking motion. When the rocking motion reaches to the peak response, then damping force is zero; so Equation (5.3) can be rewritten as follows

$$-\frac{R_a}{R_d} = \frac{k_r}{I_e} \tag{5.4}$$

Then

$$\omega_r = \sqrt{-\frac{R_a}{R_d}} \tag{5.5}$$

And the rocking stiffness of the soil k_r can be calculated as follows:

$$k_r = I_e \cdot \omega_r{}^2 \tag{5.6}$$

where R_d is the representative rocking angle, the calculation method was referred to the paper by Ligang LI et al[8]. The relationship between R_a and R_d of the peak response points is simply shown in Figure 5.1(c), and PR+

and PR- are the maximum peak response points in $R_a - R_d$ curve. And ω_r is the fundamental circular frequency for the rocking motion, see Equation (5.5).

(a) Building model   (b) SDOF model

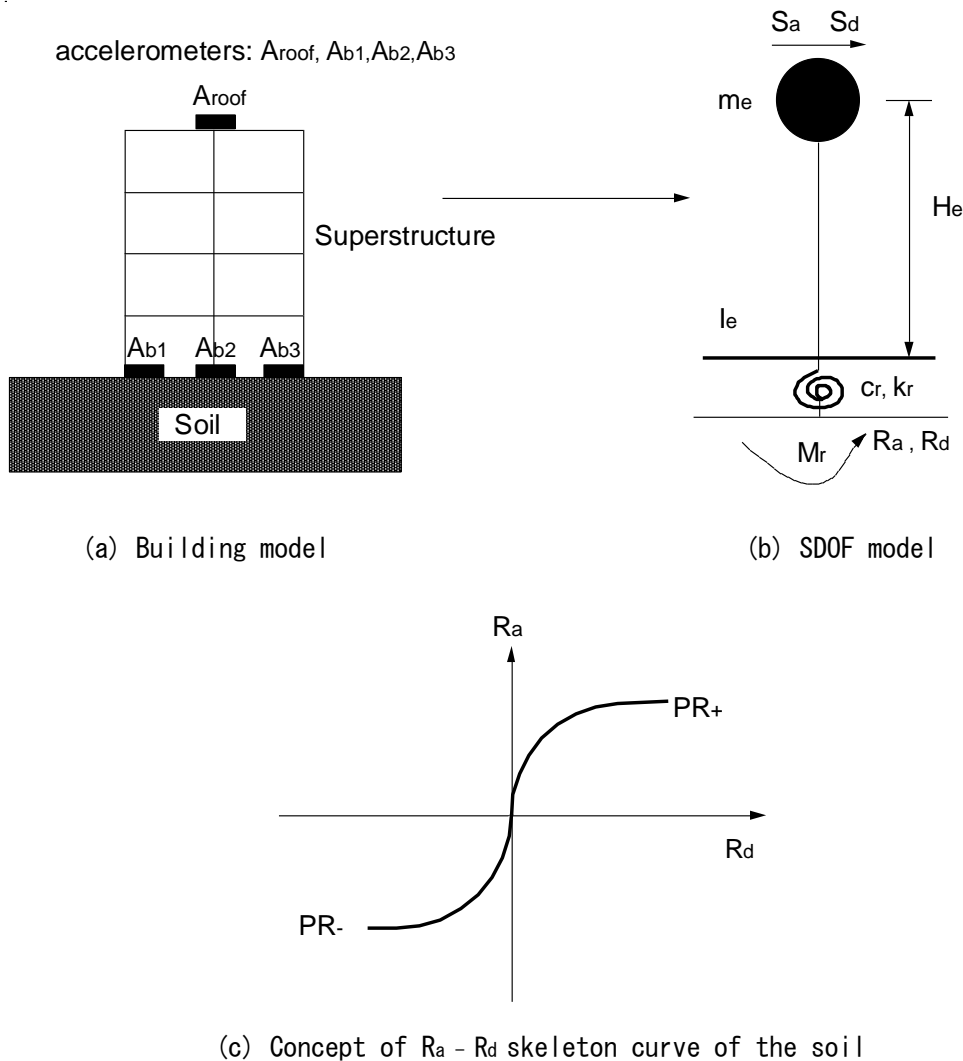(c) Concept of R_a - R_d skeleton curve of the soil

Fig. 5.1 Concept the $R_a - R_d$ curve

The fundamental responses of the superstructure (used for the calculation of S_a and the rocking motion R_d) can be extracted using the wavelet transform technique (WTT) [6], and the determination of the fundamental

responses (Rank 6 is the fundamental response through comparing the Fourier spectrum of each component) is shown in Figure 5.2 (a).

5.2.2 Polygonal Line restored from the $R_a - R_d$ curve

Like the $S_a - S_d$ skeleton curve[8], the $R_a - R_d$ skeleton curve can be obtained from some peak response points from a smaller response to the maximum response of the rocking motion, which can reflect the soil performance. However, outstanding peak response points (defined in Step 4) of the $R_a - R_d$ curve can avoid the influence of damping force (exists in the $R_a - R_d$ skeleton curve). If those points can be used to restore a simple Polygonal Line, then the linearity or nonlinearity of the soil response can be observed directly through Polygonal Line, as shown in Figure 5.2(c) (bold line); it can be found that soil response in E-W direction of the researched building in the earthquake 2011/03/11/15:15 (see Table 5.1) was almost linear. From this perspective, a series of proposed procedures of using the Polygonal Lines to evaluate the soil performance was obtained as follows:

Step 1: Accumulate the earthquake response data of the building and extract the fundamental response using the WTT technique. R_d, the representative rocking angle can also be extracted.

Step 2: The reference point is located at the ground level. Then calculate S_a, S_d and the properties of the SDOF model (m_e and H_e) [8]. Peak response points (for example, points Q_p and Q_c of S_d in Figure 5.2(c)) in $S_a - S_d$ skeleton curve will be got in this step.

Step 3: Calculate R_a, the representative rocking-moment coefficient (Equation 1(a)); then, the $R_a - R_d$ curve (fine line in Figure 5.2(c)) can be

obtained.

Step 4: Find the outstanding peak response points of the $R_d - R_a$ curve, which should satisfy three conditions at the same time: (1) these points should be corresponding to the peak response points in the $S_a - S_d$ skeleton curve (for example, points P_p to Q_p and P_c to Q_c in Figure 5.2(b)); (2) R_d is larger than 1×10^{-6} rad; (3) R_d of the current peak response point (for example point P_c in Figure 5.2(b)) is larger than that of the previous one (for example point P_p in Figure 5.2(b)).

Step 5: Outstanding peak response points (defined in step 4) of the $R_a - R_d$ curve will be connected to restore a simple Polygonal Line (bold line in Figure 5.2(c)).

In this chapter, we used Polygonal Line to judge the linearity and nonlinearity of the soil response; and the maximum peak response points (PR+ and PR- in Figure 5.1(c)) were used to calculate rocking stiffness of the soil.

(a) Fundamental response

(c) $R_a - R_d$ peak response

(b) Comparison of S_d and R_d in time domain
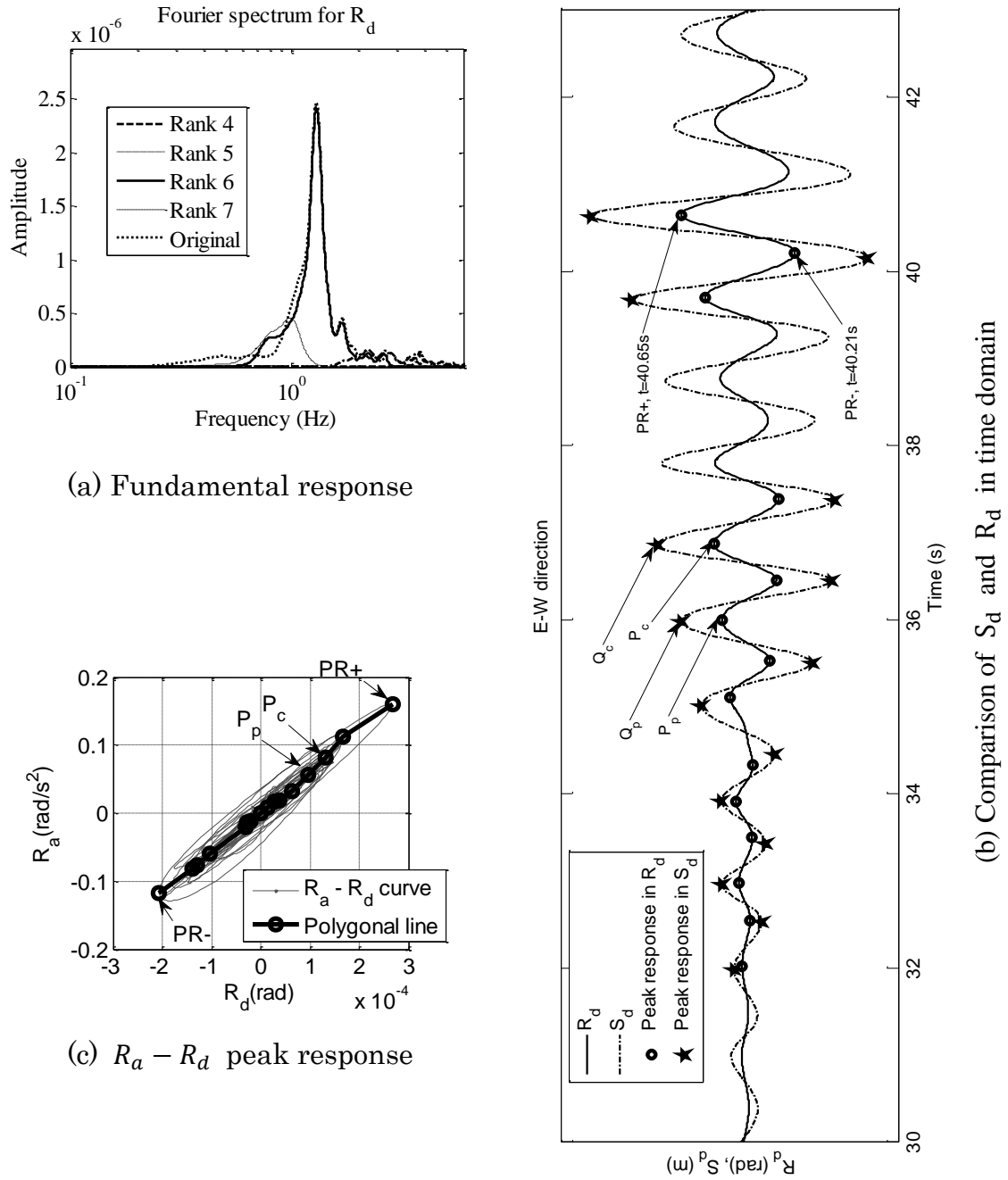
Fig. 5.2 Determination of the $R_a - R_d$ peak response for Earthquake

2011/03/11/15:15 in E-W direction

5.3 Research object

The research object of the paper is an eight-story SRC building (Building Research Institute BRI Annex Building; the dimensions of the superstructure are $H \times a \times b = 28 \times 21 \times 26$, unit: m) with a base floor underground. The locations of the accelerometers and the superstructure of the building have been discussed in chapter 3. The foundation type is a direct embedment foundation, of which the embedment depth underground is 8.5 m. The soil properties of each soil layer under the building were surveyed using the PS logging method, and the results of the soil properties are summarized in Figure 5.3.

The BRI Annex Building has experienced more than 1,239 earthquakes since it was built in 1998. Some research on the soil stiffness in earthquakes has been obtained in past years. For example, Kashima and Kitagawa[11] inferred that the soil stiffness (rocking stiffness and swaying stiffness) remained almost unchanged from 1998 to 2005, but the fluctuations in the results were very strong.

It is necessary to calibrate the rocking stiffness of the soil from 1998 to 2005 using earthquake response measurement data and also to check whether the rocking stiffness of the soil changed from 2006 to 2012. In the following sections, the outstanding peak response points of the $R_a - R_d$ curves of the foundation will be used to answer these questions. In this chapter, seven of the most significant earthquake records were selected from 1998 to 2012; see Table 5.1.
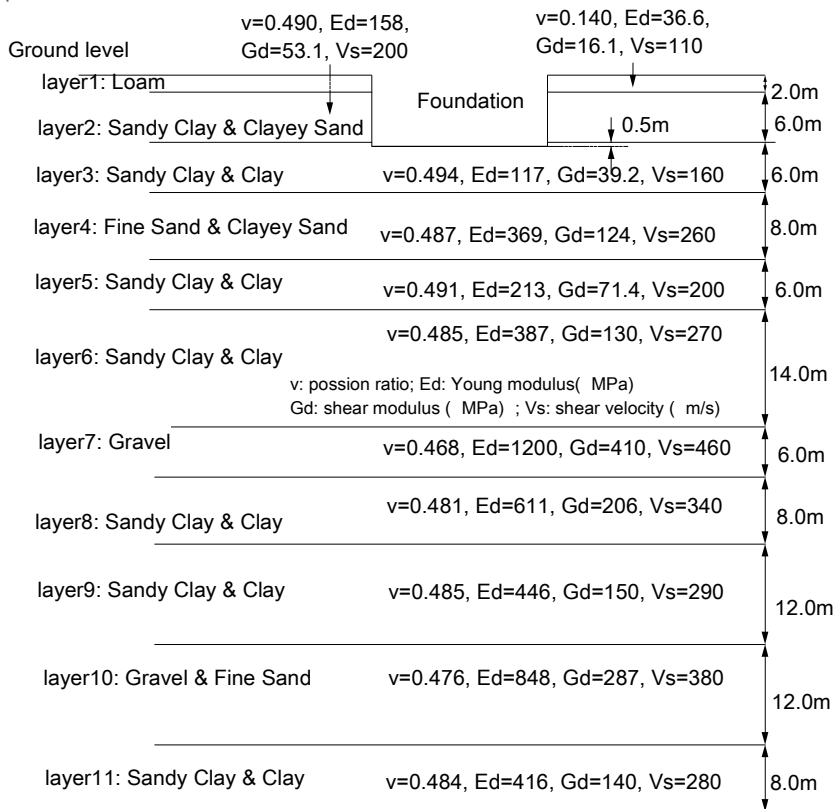
Figure 5.3 Soil properties under the Annex building

Table 5.1 Seven strong earthquakes that occurred in Japan between 1998

and 2012

Time	Epicenter	Latitude	Longitude	Depth (Km)	M (Degree)	Dist. (Km)	PGA (gal)	IJMA (Degree)	Fundamental response		Number
									E-W	N-S	
2003-09-20 12:54	S Chiba Pref.	140.3033	35.2150	70	5.8	104	13.7	2.8	rank6	rank6	E1
2004-10-06 23:40	S Ibaraki Pref.	140.0917	35.9850	66	5.7	17	54.5	3.8	rank6	rank6	E2
2005-08-16 11:46	Off Miyagi Pref.	142.2783	38.1500	42	7.2	298	29.8	3.3	rank6	rank6	E3
2008-06-14 08:43	S Inland Iwate Pref.	140.8800	39.0283	8	7.2	330	26.2	3.4	rank6	rank6	E4
2011-03-11 14:46	Off Sanriku	142.8600	38.1033	24	9.0	330	279.3	5.3	rank6	rank6+rank7	E5
2011-03-11 15:15	Off Ibaraki Pref.	141.2650	36.1083	43	7.6	107	151.1	4.7	rank6	rank6	E6
2011-04-11 17:16	Hama-dori, Fukushima Pref.	140.6717	36.9450	6	7.0	105	118.1	4.6	rank6+rank7	rank6+rank7	E7

5.4 Evaluation of rocking stiffness of the soil using the maximum peak response points of the $R_a - R_d$ curve

5.4.1 Study on the soil responses

The calculation method for the Polygonal Lines and the outstanding peak response points were previously introduced in Sections 5.2.1 and 5.2.2. Using the Polygonal Lines, soil responses of the 7 strong earthquakes were analyzed in this part.

As shown in Figure 5.4, the Polygonal Lines and the outstanding peak response points show that the soil responses were linear in most of the seven earthquakes (except E5 for the Tohoku Earthquake off the Pacific Coast in 2011). For example, the soil performance remained unchanged in Earthquakes E1–E4, E6, and E7; Earthquakes E5 showed that the soil performance decreased in the E-W direction during the earthquake (points A and B, see Figure 5.4(e)).

The maximum peak response points could be used to calibrate the rocking stiffness of the soil in earthquakes E1–E7.

5.4.2 Fundamental rocking period

According to the analysis in Section 5.4.1, the maximum peak response points of $R_a - R_d$ curves could be used to calculate the fundamental natural frequency of the rocking motion (Eq. (5.5)). Then the fundamental natural periods for the rocking motion in the seven earthquakes are summarized in Figure 5.5.

As shown in Figure 5.5, in the E–W direction, the fundamental natural periods for the rocking motion of Earthquakes E1–E4 (and the points A+ and A- in earthquake E5) were almost stable. The period was approximately

0.17–0.20 s, whereas for Earthquakes E5 (points B+ and B-)–E7, the period was approximately 0.25 s. In the N–S direction, the fundamental periods of the rocking motion for the seven earthquakes were approximately 0.15–0.18 s.

### 5.4.3 Influence of mass uncertainty on $R_a - R_d$ curve

To calibrate the rocking stiffness, the core problem is how to determine the total mass of the building. Therefore, in this chapter, two cases (Cases 1 and 2; see Table 5.2) were studied and could be used as the approximation values of the total mass.

For Case 1 (the upper limit), the masses of each floor were taken from the design document (the combination of the live loads and dead loads for each structural element and the different function rooms), which were calculated based on design standards. For Case 2 (the lower limit), mass density is approximately 0.8×10^3 kg/m² for the SRC office building[12]. This value will be used for the calculation $m_i = A_i \times \rho$ (where A_i is the area of the i-th floor), and ρ is the mass density 0.8×10^3 kg/m². The mass distribution is summarized in Table 5.2.

As shown in Figures 5.6 and 5.7, the equivalent height of the SDOF model H_e (approximately 18.4–18.8 m, with a ratio H_e/H of approximately 0.66) and the equivalent mass ratio M_e/M_{total} (approximately 0.72–0.75) are the same for the seven earthquakes in the two cases (Cases 1 and 2). This means that the influence of the absolute value of the total mass of the superstructure on the $R_a - R_d$ curves is little because the mass distributions (mass ratio) in Cases 1 and 2 are almost the same (a little different); see Table 5.2.
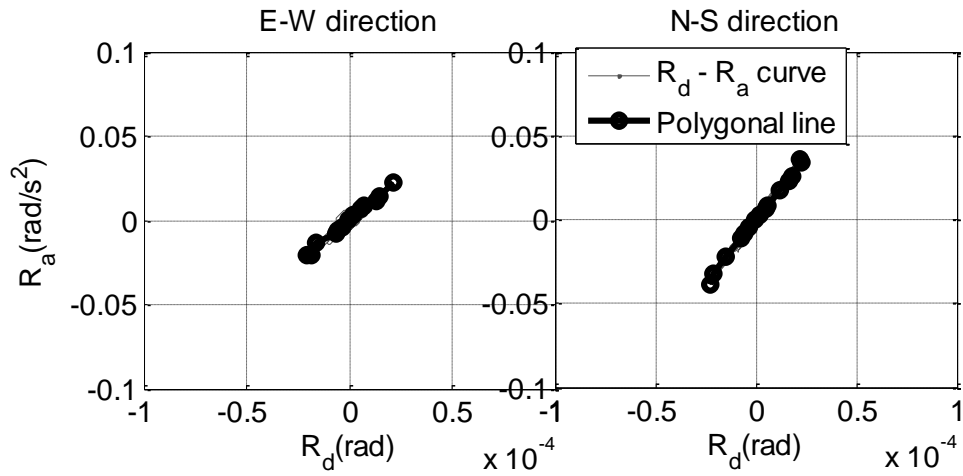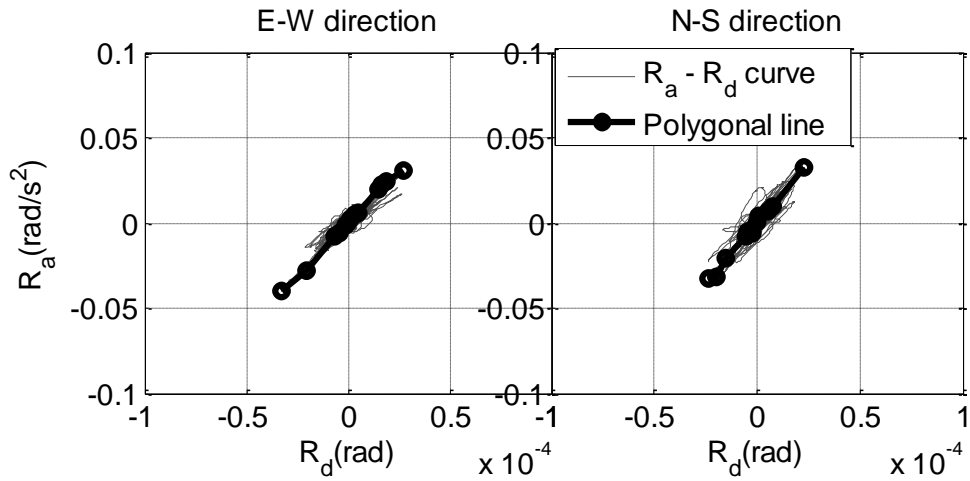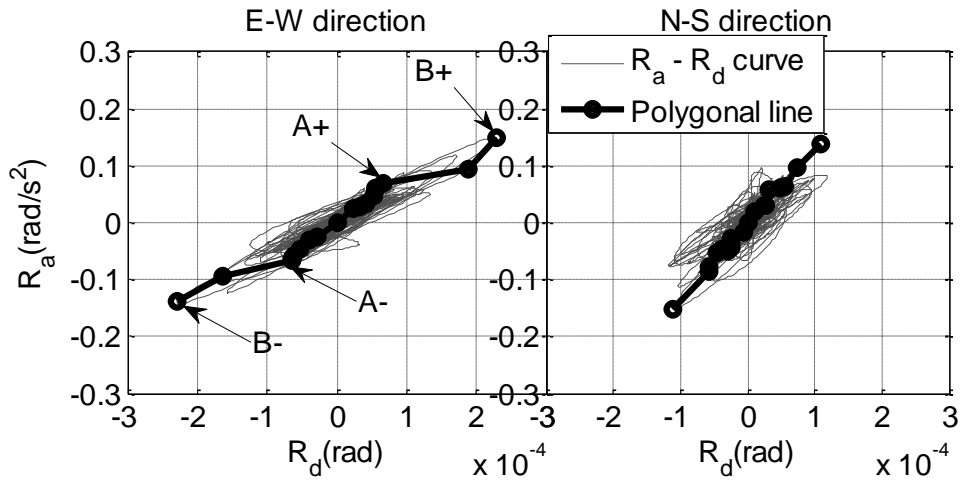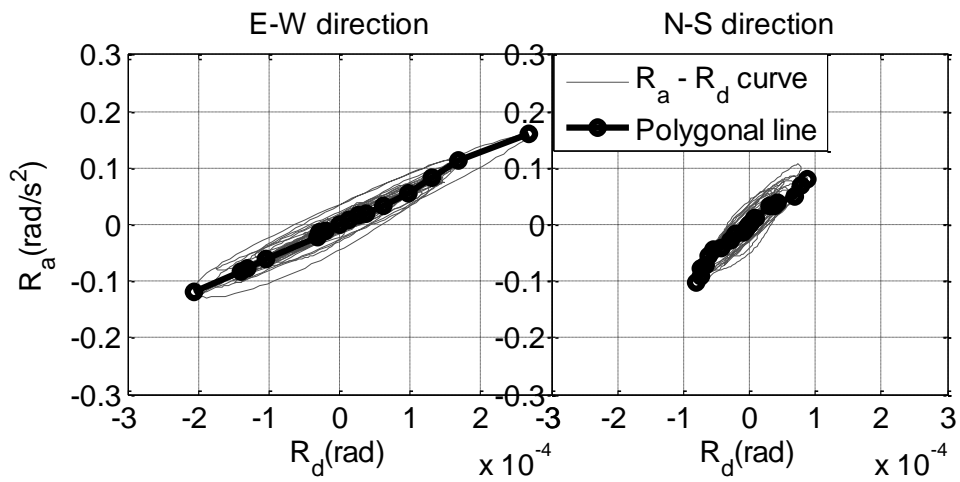
(a) E1

(b) E2
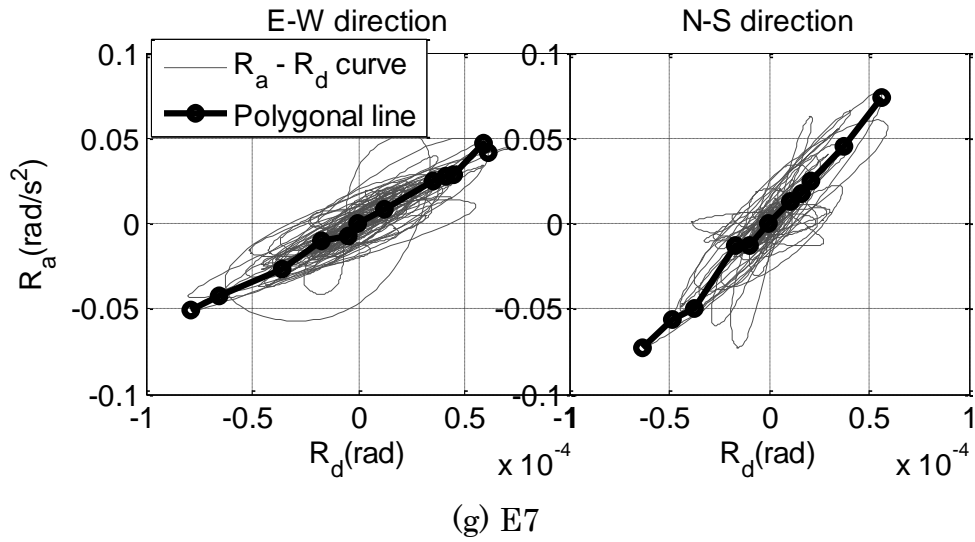

(c)E3

(d) E4

(e) E5

(f) E6

(g) E7
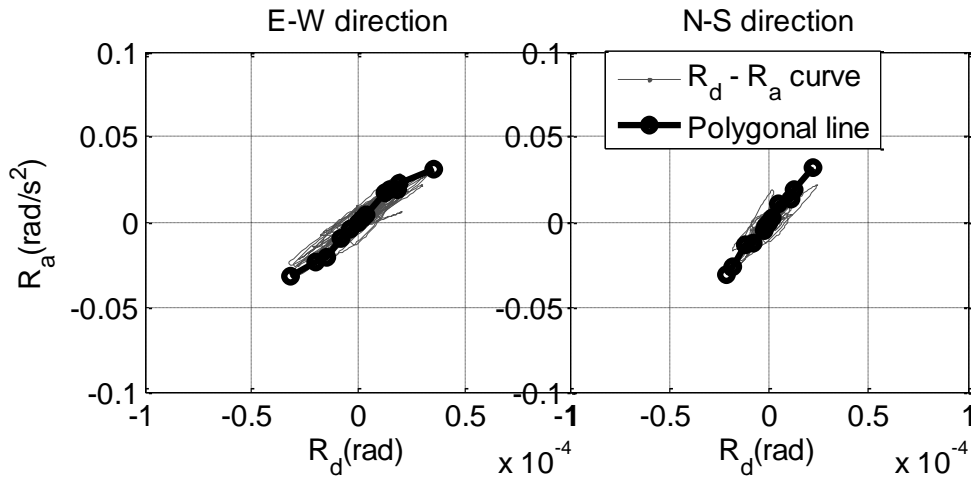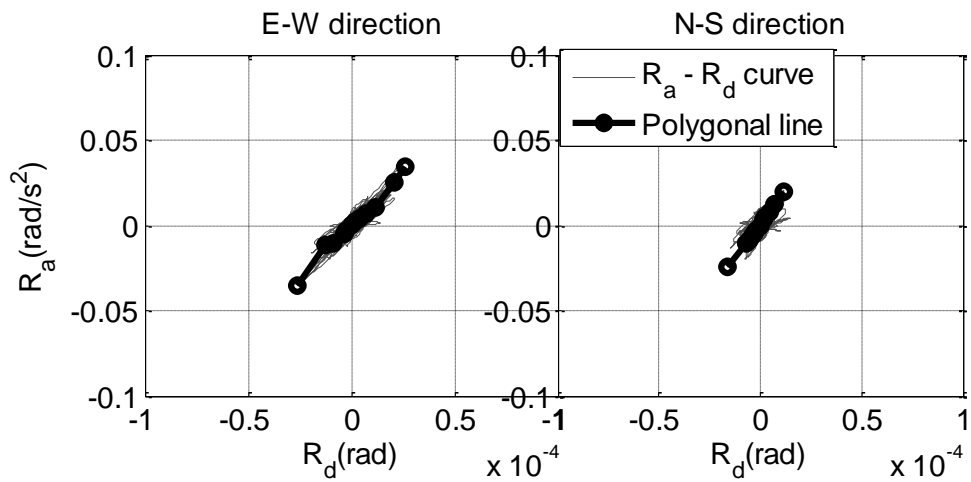
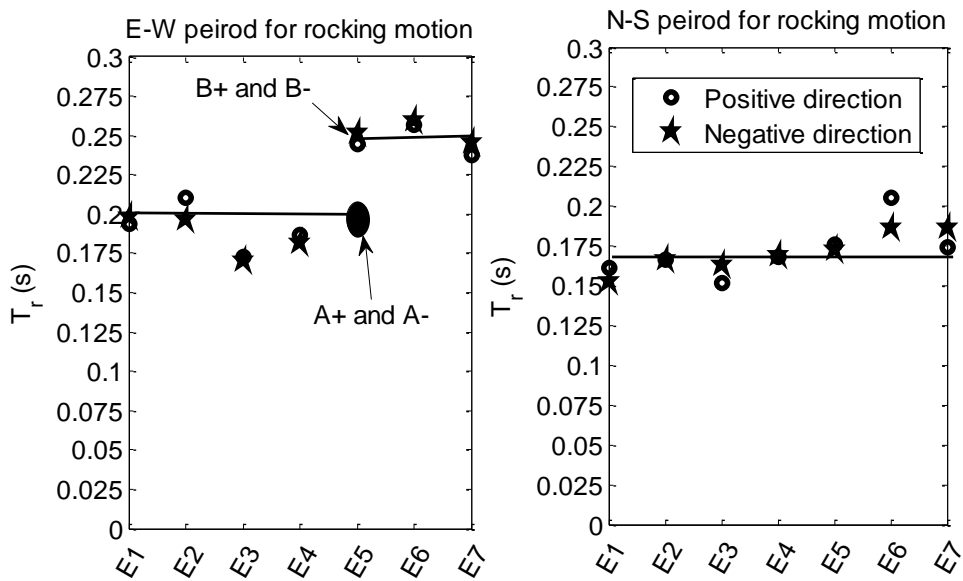Fig. 5.4 Peak response points of the $R_a - R_d$ curve

Fig. 5.5 Natural fundamental period for rocking motion

Table 5.2 Masses, areas, and heights of superstructure

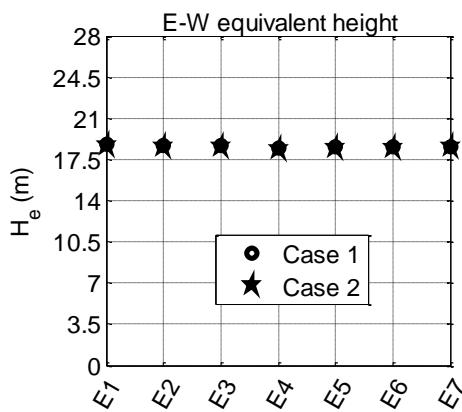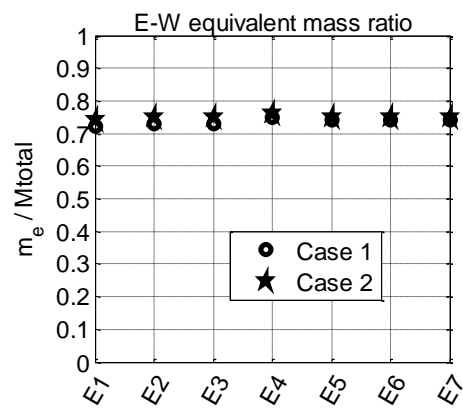| Floor	h_i (m)	Mass m_i (mass ratio: m_i/M_{total})				
		Case 1	Case 2			
		$(10^6$ kg)	Area (m²)	Density (10^3 kg/m²)	m_i $(10^6$ kg)	
8 +P1F	28.0	0.30 (0.059)	186.38			0.15 (0.049)
7	22.9	0.82 (0.16)				
6	19.2	0.74 (0.14)				
5	15.5	0.77 (0.15)	620.88			0.50 (0.16)
4	11.8	0.93 (0.18)		0.8		
3	8.1	0.78 (0.15)				
2	4.3	0.78 (0.15)	531.26			0.42 (0.14)
1	0.0	—	—			—
B1F	−6.0	—	—			—
M_{total}: Case 1, 5.12×10^6 kg; Case 2, 3.07×10^6 kg						

Fig. 5.6 Equivalent height

Fig. 5.7 Equivalent mass ratio

5.5 Current calculation methods of rocking stiffness of soil

5.5.1 Calculation method of response and limit strength (published by AIJ)[1, 13]

The rocking stiffness for the vertical direction is calculated as follows

$$K_{rb} = \beta_R K_{1r} \tag{5.7}$$

Where β_R reflects the contribution of all soil layers for the total rocking stiffness, K_{1r} is the rocking stiffness for the first soil layer, and the calculation model is shown in Figure 5.8.

$$\beta_R = \frac{1}{\sum_{i=1}^{n}(1/\alpha_{ri})} \tag{5.8}$$

$$K_{1r} = \frac{4}{3}\frac{E_1 r_{r0}^3}{1-\nu_1^2} \tag{5.9}$$

Where

$$\alpha_{ri} = \left(\frac{E_i}{E_1}\right)\frac{z_{ri}^3 \cdot z_{ri-1}^3}{z_{r0}^3 \cdot (z_{ri}^3 - z_{ri-1}^3)} \quad (i=1,\cdots,n-1) \tag{5.10}$$

$$\alpha_{rn} = \left(\frac{E_n}{E_1}\right)\left(\frac{z_{rn-1}}{z_{r0}}\right)^3 \tag{5.11}$$

$$z_{r0} = \frac{9}{16} \cdot \pi \cdot (1-\nu_1^2) r_{r0} \tag{5.12}$$

When considering the embedment effect of the foundation in the soil, the rocking stiffness will be calculated as follows[13]:

$$K_r = K_{rb} + K_{re} \tag{5.13}$$

$$K_{re} = \xi_{re} \cdot K_{rb} \cdot \left\{2.3 \cdot \frac{D_e}{r_{r0}} + 0.58 \cdot \left(\frac{D_e}{r_{r0}}\right)^3\right\} \cdot \frac{G_{he}}{G_{hb}} \tag{5.14}$$

Where K_{re} is caused by the foundation embedment effect (reduction coefficient ξ_{re} is 0.5 under strong earthquakes); D_e is the embedment depth of the foundation, G_{he} and G_{hb} can be calculated as follows (see Figure 5.9),

$$G_{he} = \frac{\sum_{i=1}^{m} G_i \cdot H_i}{\sum_{i=1}^{m} H_i} \tag{5.15}$$

$$G_{hb} = \frac{(2-\nu) \cdot K_{hb}}{8 \cdot r_0} \tag{5.16}$$

Where K_{hb} is the horizontal soil stiffness, and the detailed calculation procedure can be found in the same document[13].

5.5.2 Calculation method based on JARA standard[14]

The JARA (Japanese Road Association) standard gives a method of calculating the vertical ground reaction force coefficient k_v as follows:

$$k_v = k_{v0} \cdot \left(\frac{B_V}{0.3}\right)^{-3/4} \tag{5.17}$$

where $k_{v0} = 10/3 \cdot \alpha \cdot E_0$, in which α is a scaling factor (as for the PS Well Logging method in this paper, earthquake condition: $\alpha = 0.25$[15]); and E_0 is calculated by the elastic modulus of the layered soil obtained by PS Well Logging method; $B_V = \sqrt{a \times b}$ (size of the foundation mat).

Because the soil responses during the earthquakes were linear, see Figure 5.4; so the rocking stiffness (k_{rb}, see Figure 5.9) can be calculated as follows:

$$k_{rb} = k_v \cdot I \tag{5.18}$$

where I is the moment of inertia of the foundation mat ($I = ab^3/12$, unit: m^4, where a and b are the size of the foundation mat, unit: m).
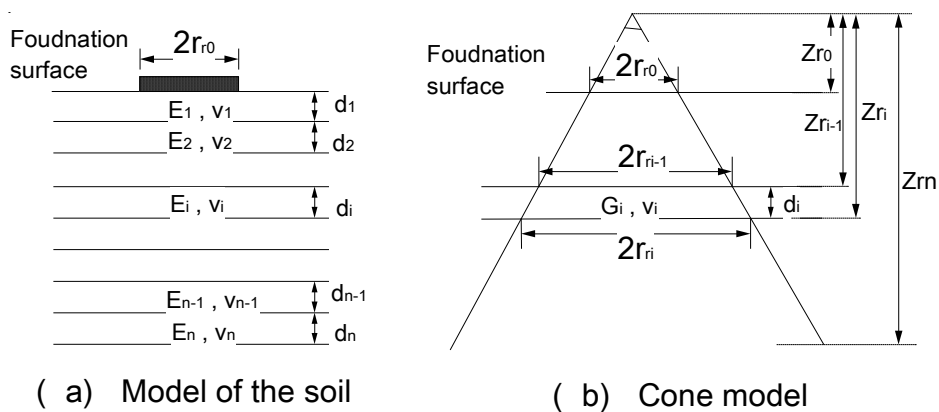

(a) Model of the soil   (b) Cone model
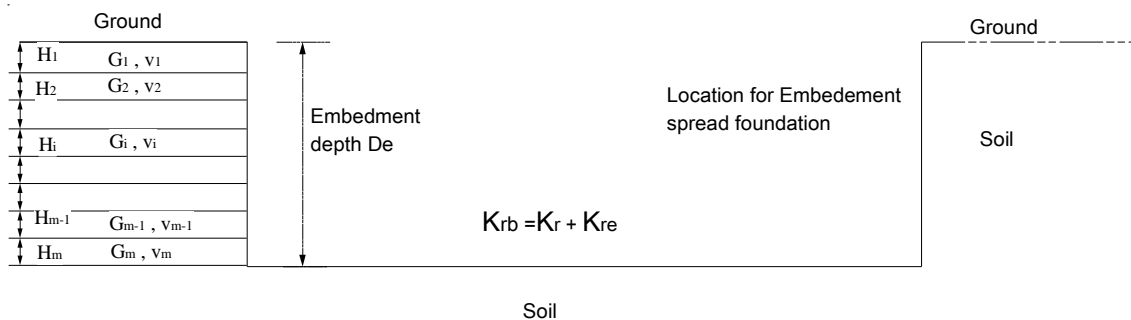
Fig. 5. 8 Calculation model for the rocking stiffness

Fig. 5. 9 Concept of the rocking stiffness

5.6 Calibration of rocking soil stiffness

The previous analysis (section 5.4.2) showed that the fundamental natural period T_r (corresponding to the rocking motion) 0.19 s (mean value in the E–W direction) and 0.16 s (mean value in the N–S direction) remained almost stable in Earthquakes E1 (2003)–E4 (2008) (and the points A+ and A- in earthquake E5). In this section, the five earthquakes are used to calibrate the rocking stiffness of the soil.

Based on the analysis in section 5.4.3, it can be concluded that the fundamental rocking frequency ω_r (= $2\pi/T_r$, where T_r is the fundamental rocking period) of a specific SRC building is independent of different estimations of the total mass (and even when mass distributions are a little different; see Table 5.2) and equivalent height H_e. According to Equation (5.6), the moment of inertia I_e (corresponding to M_{total} and H_e) determines the value of the rocking stiffness when ω_r is fixed. Therefore, a range of total mass (M_{total} for Case 2, M_{total} for Case 1) was set up to calibrate the rocking stiffness. Then, the rocking stiffness was calculated and summarized in Table 5.3.

89

Table 5.3 Comparison of the rocking stiffness of the soil

	Rocking stiffness (10^{12} N·m/rad)		
	AIJ	Real values	JARA standard
E–W	$0.56(K_{rb}) + 0.32(K_{re})$ $= 0.87$	0.84 (Case 2) ~1.40 (Case 1)	$K_{rb} = 0.146$
N–S	$0.82(K_{rb}) + 0.41(K_{re})$ $= 1.23$	1.18 (Case 2) ~1.97 (Case 1)	$K_{rb} = 0.225$

As shown in Table 5.3 for Case 1, the rocking stiffness calculated using the measurement data is greater (1.6 times) than the designed values by the calculation method of response and limit strength. However, the real-time values are much greater (5-10 times) than those in the JARA standard, of which the vertical ground reaction force coefficient k_v was used to calculate the rocking stiffness with the model shown in Figure 5.9. For Case 2, the rocking stiffness calculated by the calculation method of response and limit strength agreed well with the results from the measurement data. It can be concluded that the estimation of the total mass has a significant influence on the calibration of the rocking stiffness of the soil.

In conclusion, the rocking stiffness calculated by the calculation method of response and limit strength is not accurate and needs to be improved; and the vertical ground reaction force coefficient k_v defined by JARA standard cannot reflect the real measurement of the soil stiffness. The total mass of the superstructure is a significant factor to determine the value of the rocking stiffness.

5.7 Influence of the ground motion on the $R_a - R_d$ curve
## 5.7.1 Analysis on the vertical motion of the ground

In order to analyze the vertical motions of the ground, 5 measurement points (N14, 14 meters under the building; A01, B01 and C01, 1 meter under the ground; A14, 14 meters under the ground, see Figure 5.10) located in the soil were studied. The vertical motions of the 5 points were recorded during the earthquakes, see Figure 5.11 (c). The earthquake E7 was taken as the analysis sample in this section.

As shown in Figure 5.12, the 5 points are separated into three cases: (1) case 1, the reference point is N14, and the relative vertical motions of A01 and A14 are shown in Figure 5.13(a); (2) case 2, the reference point is A01, and the relative vertical displacements of B01 and C01 are shown in Figure 5.13(b); (3) case 3, the reference point is N14, and the relative vertical motions of A01 and B01 are shown in Figure 5.13(c).

According to the Figure 5.13, it was found that almost at any time: (1) rotation motion exists between points N14 and A01, A14, and the rotation directions are almost same for A01 and A14; (2) rotation motion happens between points A01 and B01, C01, and rotation directions are almost same for B01 and C01; (3) rotation motion exists between points N14 and A01, B01, and rotation direcitons are almost same for A01 and B01.
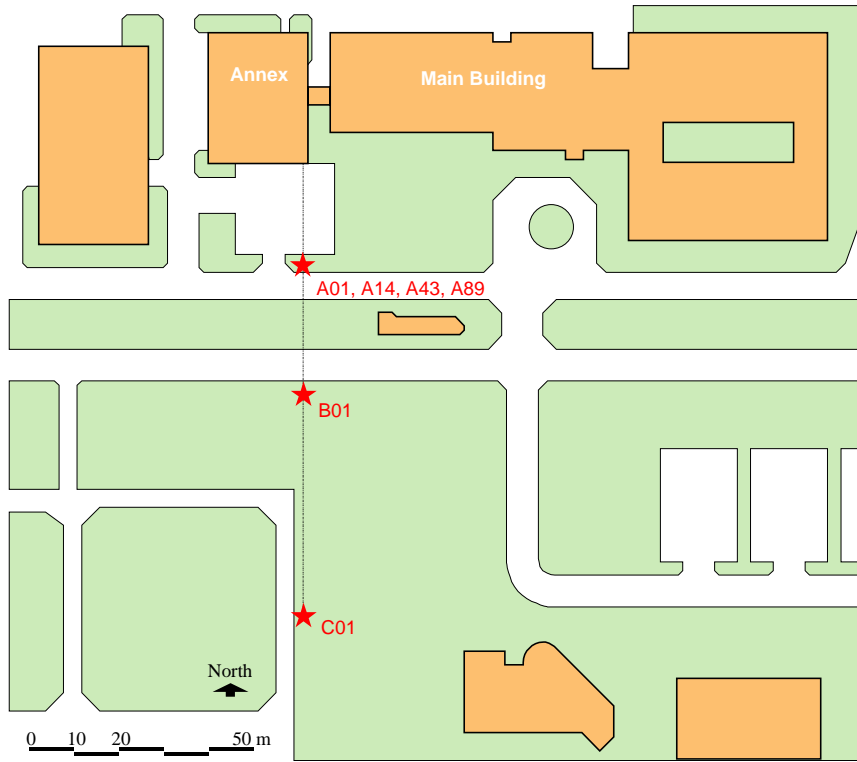
(a)Location of the building and accelerometers on the ground
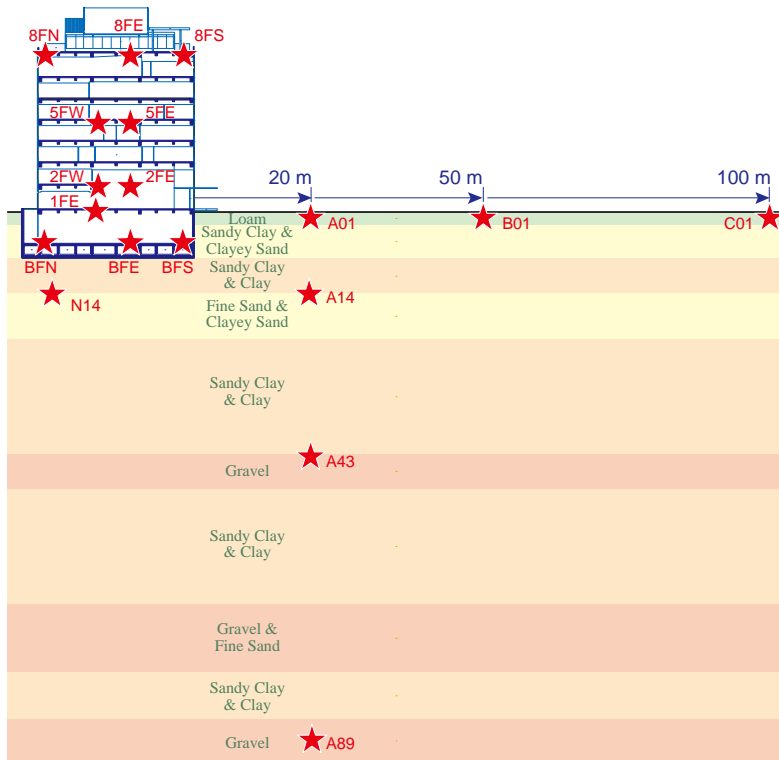
(b) Locations of the accelerometers in the soil

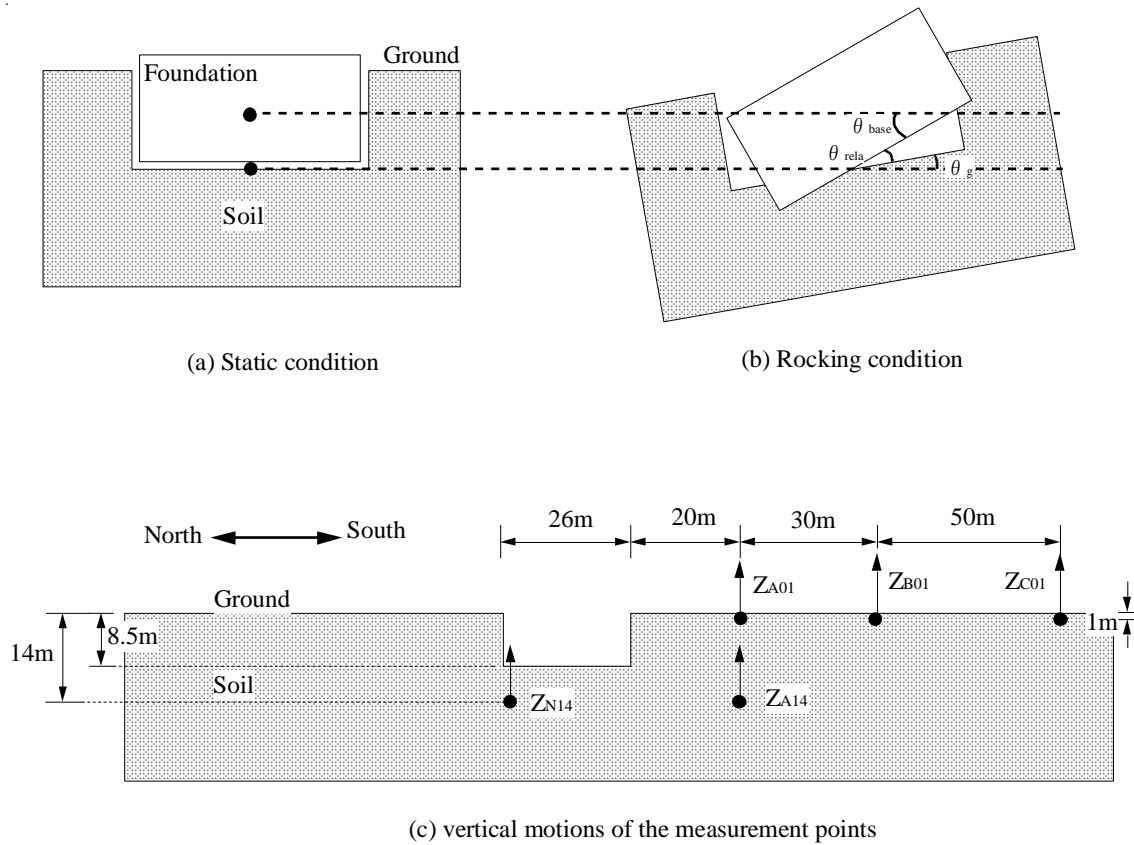Fig. 5.10 Distribution of the accelerometers in the ground and the soil

(a) Static condition   (b) Rocking condition

(c) vertical motions of the measurement points

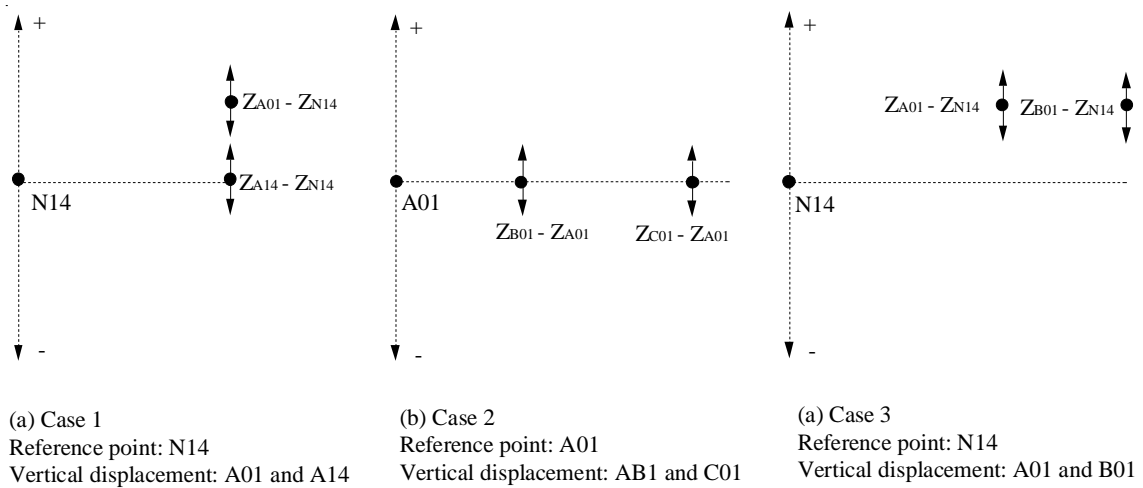Fig. 5.11 Concept of the rocking motion for the surrounding ground of the building in

Figure 5.9

(a) Case 1
Reference point: N14
Vertical displacement: A01 and A14

(b) Case 2
Reference point: A01
Vertical displacement: AB1 and C01

(a) Case 3
Reference point: N14
Vertical displacement: A01 and B01

Fig. 5.12 Concept of the Relative vertical displacements among the 5

measeruemnt points of Figure 5.11
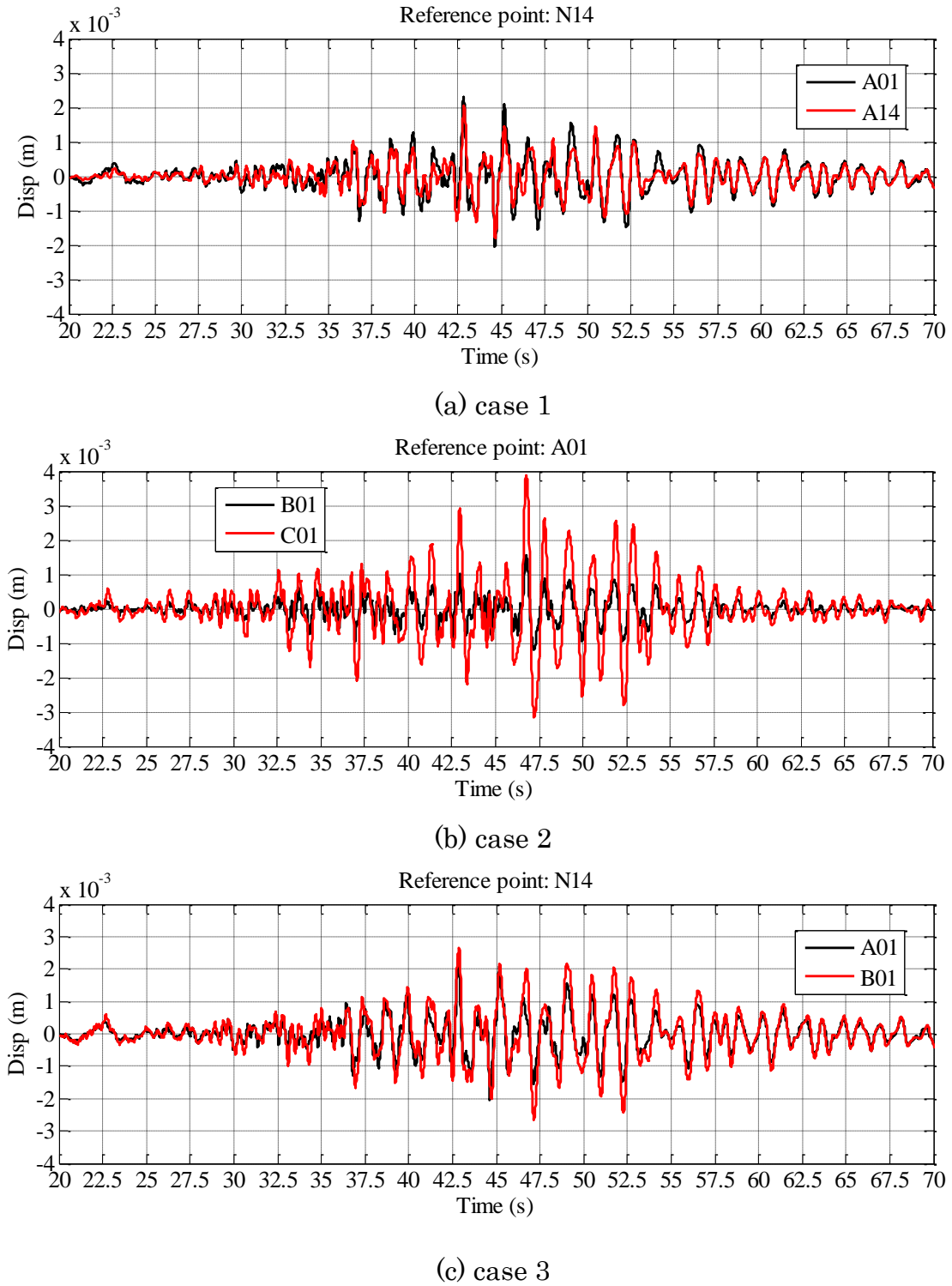
(a) case 1

(b) case 2

(c) case 3

Fig. 5.13 Relative vertical displacements of the 3 cases of Figure 5.12 for earthquake E7 in N-S direction

It can be concluded that rotation motions of the ground existed surrounding the building, and the rotation motion (rocking angle) of the basement maybe contain the rotation motions (rotation angle) of the ground.

5.7.2 Calculation of the rotation angle of the ground

As for the calculation of the rocking angle of the building θ_{base}, the motions of the three points BFN, BFE and BFS located on the base floor were used, see Figure 5.10 (b). However, θ_{base} reflects the absolute rocking motion of the foundation, which contains the rototation motion of the ground. In order to get the $R_a - R_d$ curve of the soil (reflects the relationship bewteen the deformation of soil and the moment of the building), the relative rotation angle θ_{rela} between the foundation and its surrounding ground should be calculated, see Figure 5.11 (b). There is a simple relationship between θ_{base} and θ_{rela} as follows,

$$\theta_{rela} = \theta_{base} - \theta_g \quad (5.19)$$

Where θ_g is the rotation angle of the ground surrouding the foundation, see Figure 5.11 (b). The vertical motions of the measurement points can be used to calculate θ_g. For the case shown in Figure 5.10 and 5.11, five points (A14, N14, A01, B01 and C01) and four equations will be employed to calculate θ_g, which are as follows, see Figure 5.12.

For points N14 and A14:

$$\theta_{g1} = \frac{Z_{A14} - Z_{N14}}{46} \quad (5.20)$$

For points A01 and B01:

$$\theta_{g2} = \frac{Z_{B01} - Z_{A01}}{30} \quad (5.21)$$

For points A01 and C01:

$$\theta_{g3} = \frac{Z_{C01} - Z_{A01}}{80} \qquad (5.22)$$

For points B01 and C01:

$$\theta_{g4} = \frac{Z_{C01} - Z_{B01}}{50} \qquad (5.23)$$

As shown in Figure 5.14 and Figure 5.15, the rotation motions of the ground were strong compared with the rocking motion of the foundation in earthquake E7. Fourier spectrums (Figure 5.14) show that rotation motions θ_{g2}, θ_{g3} and θ_{g4} own almost the same frequency spectrums, but the θ_{g1} is a little different from the three rotation motions. One of the reasons may be because of the locations of the measurement points. For example, the measurement points A01, B01 and C01 (used for the calculation of θ_{g2}, θ_{g3} and θ_{g4}) were located in the free field ground; but A14 and N14 (for θ_{g1}) were under the ground, and the building was just above the point A14, see Figure 5.10 (b).

(a) θ_{g1}
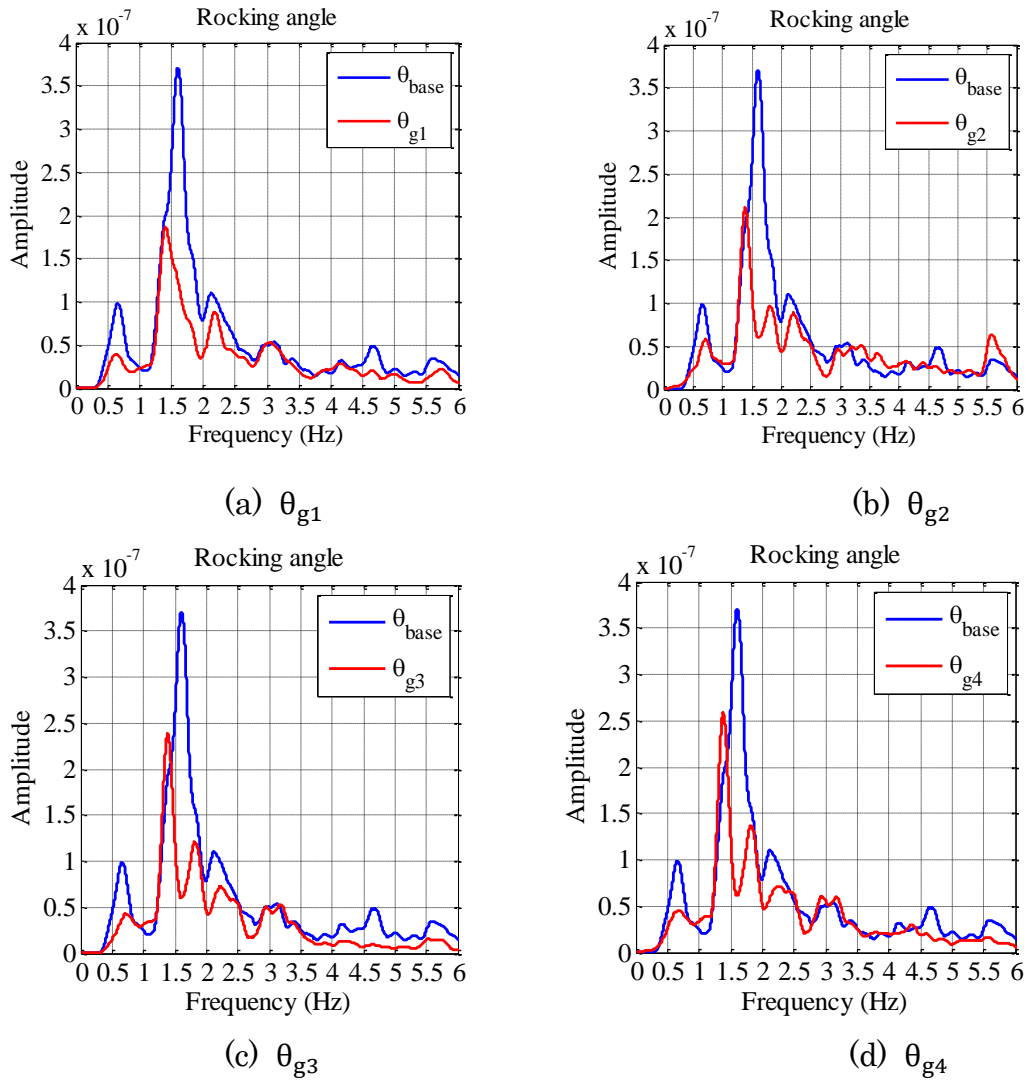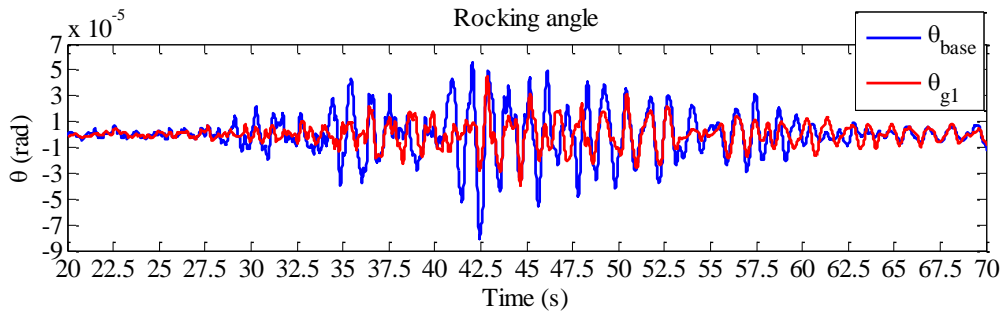
(b) θ_{g2}

(c) θ_{g3}
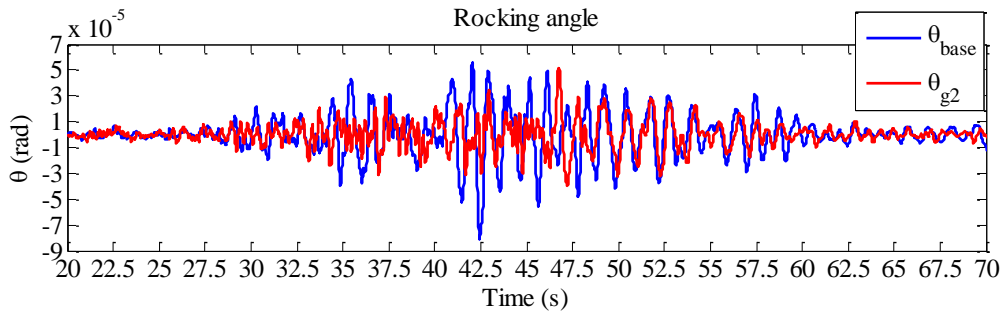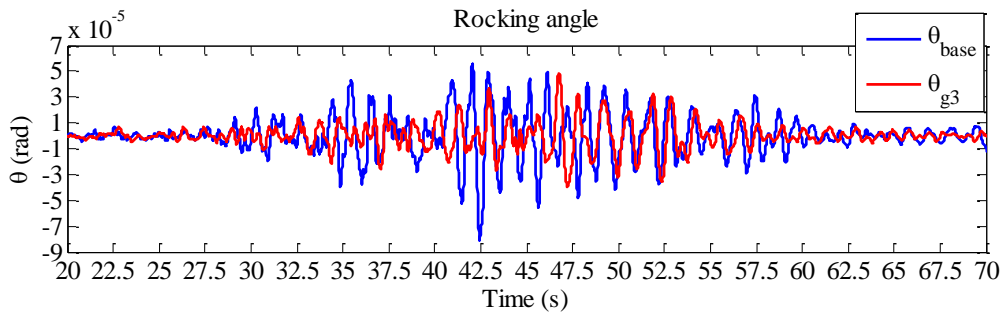
(d) θ_{g4}

Fig. 5.14 Fourier spectrum of the θ_g for earthquake E7 in N-S direction
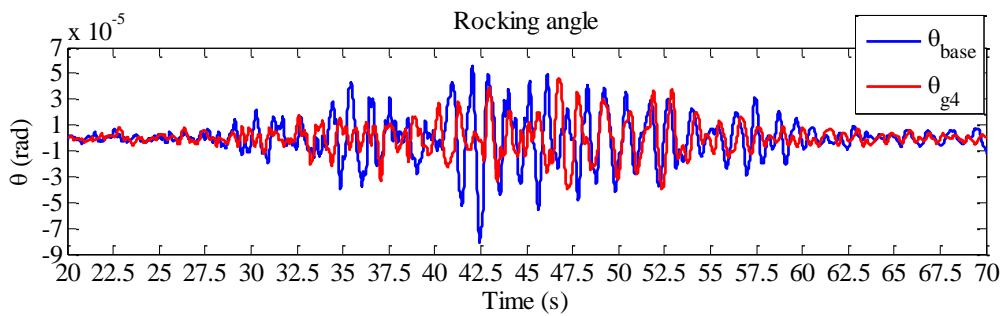
(a) θ_{g1}

(b) θ_{g2}

(c) θ_{g3}

(d) θ_{g4}

Fig. 5.15 Time history of the N-S direction rotation angles for earthquake E7

5.7.3 Decision of the rotational motions of the ground surrounding the building

Based on previous analysis, it is already known that the rotational motions of the ground occurred during the earthquakes. The different rotational motions (θ_{g1}, θ_{g2}, θ_{g3} and θ_{g4}) would be achieved using different measurement points. In this section, the influence of the different rotational motions of the ground on the shape of $R_a - R_d$ curve of the foundation of the building is studied. The calculation model of the relative rocking angle θ_{rela} can be shown as Equation (5.19) and Figure 5.11 (a) and (b), θ_{rela} is the relative rotational angle between θ_{base} and θ_g. The earthquake E7 was taken as the example, see Figure 5.16. The comparison between the θ_{base} (absolute rocking angle of the foundation) and the θ_{rela} (relative rotation motion between the foundation and the surrounding ground, θ_{g2} as the rotation motion of the ground) is shown in Figure 5.16.

The representative rocking angle R_d will be corresponding to the θ_{base} and the θ_{rela} respectively. Then Wavelet Transform Technology was employed to get fundamental response of the rocking angle. As shown in Figure 5.17, five different cases for R_d (rank 6 as the fundamental response) were campared. It can be found that the hysteresis loops of the $R_a - R_d$ curve for $\theta_{base} - \theta_{g2}$ (see Figure 5.17 (c)) are much clearer than other cases. It is concluded that the soil response is linear according to the Figure 5.17 (c), but it is difficult to get the same coclusion for other cases. The reason may be because of the locations of the measurement points, which has already dicussed in section 5.7.2.

It is deemed that the rotational motions of the ground have much influence

on the shape the $R_a - R_d$ curve, when the rotational motions of the ground are strong. In a sense, the rotational motions of the ground are kinds of noise. However, the $R_a - R_d$ curve is still easy to be understood once the the rotational motions of the ground iseliminated. In this resarch, θ_{g2} can be accepted as the real rotational motions of ground surrounding the building.
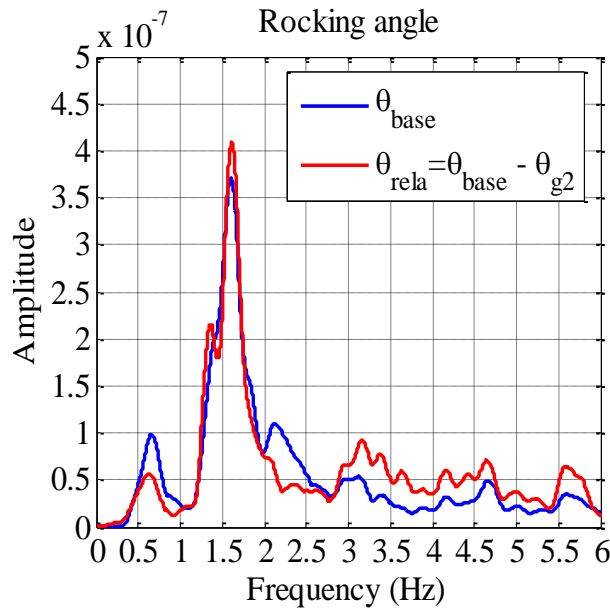
(a) Fourier spectrum of θ_{rela} for E7 in N-S direction
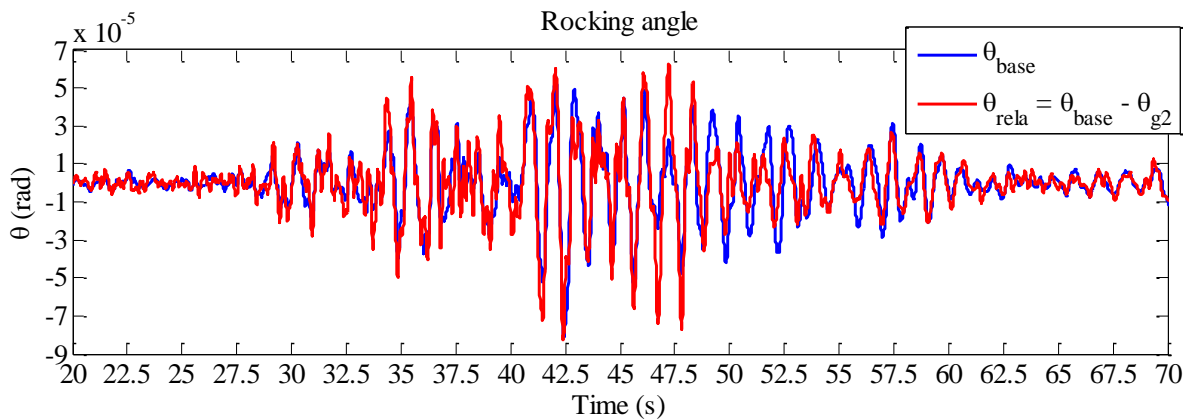
(b) Time history of θ_{rela}

Fig. 5.16 Relative rocking angle θ_{rela} of the foundation to the ground for θ_{g2} for E7 in N-S direction

(a) R_d for θ_{base}

(b) R_d for $\theta_{base} - \theta_{g1}$

(c) R_d for $\theta_{base} - \theta_{g2}$

(d) R_d for $\theta_{base} - \theta_{g3}$

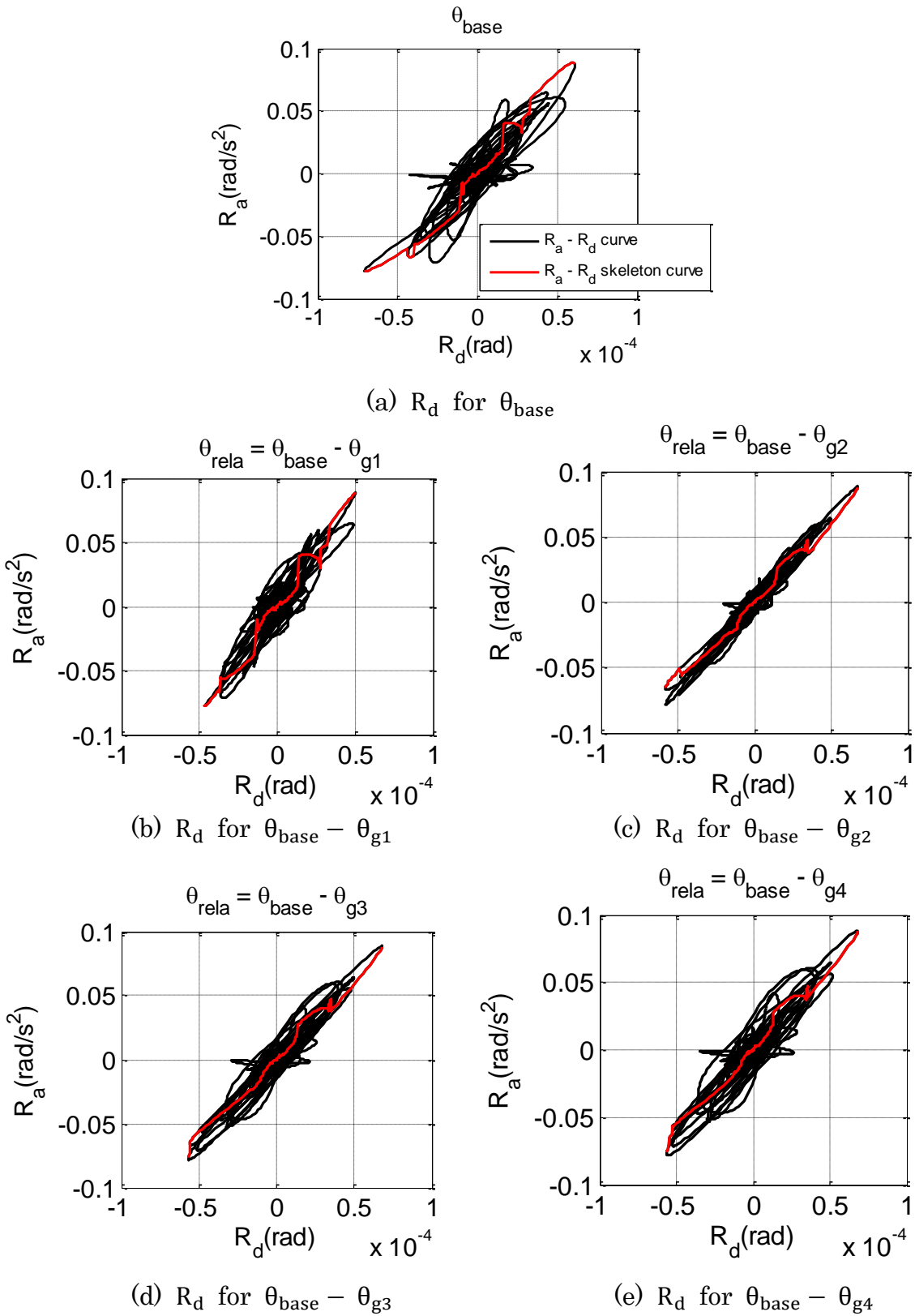(e) R_d for $\theta_{base} - \theta_{g4}$

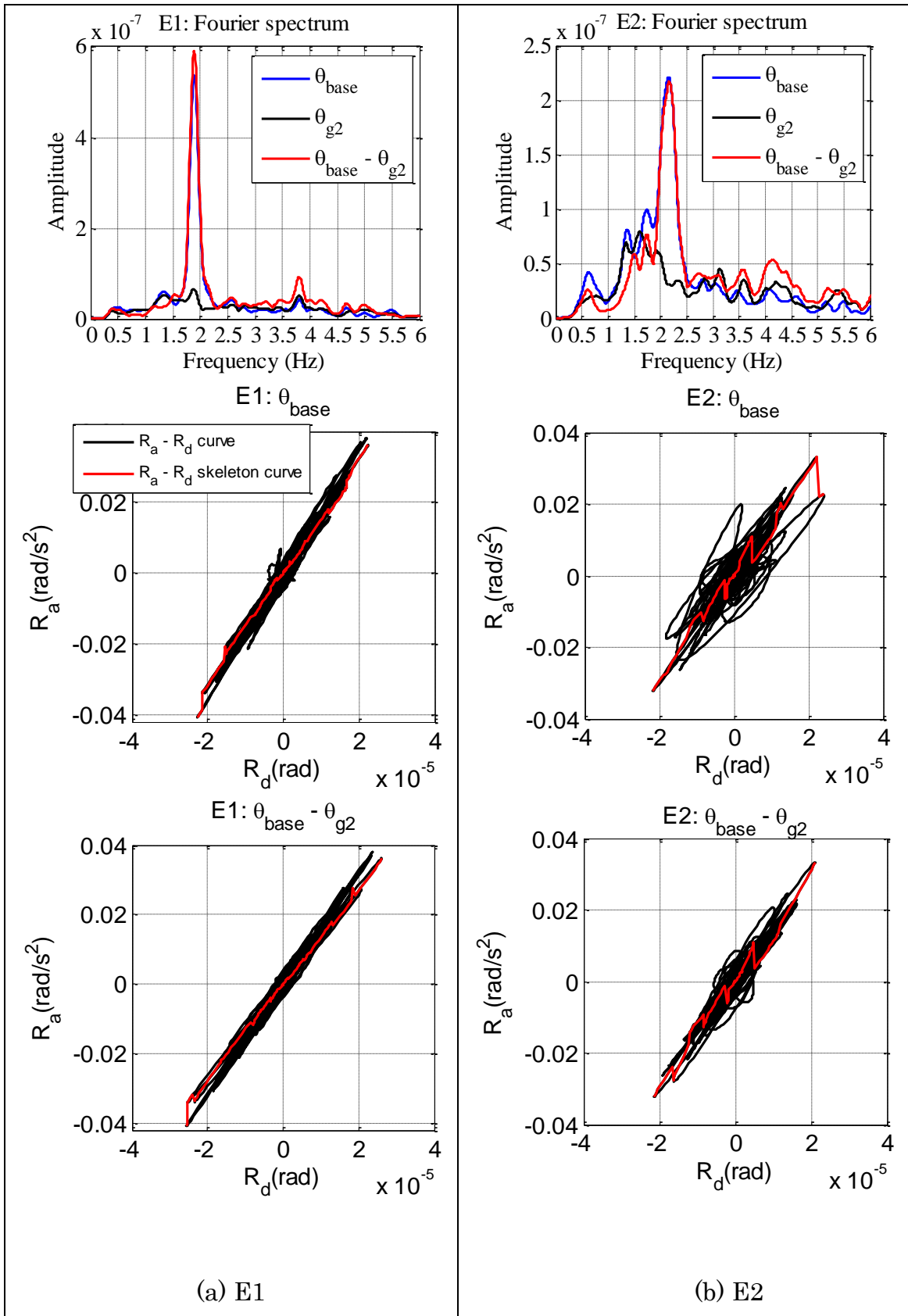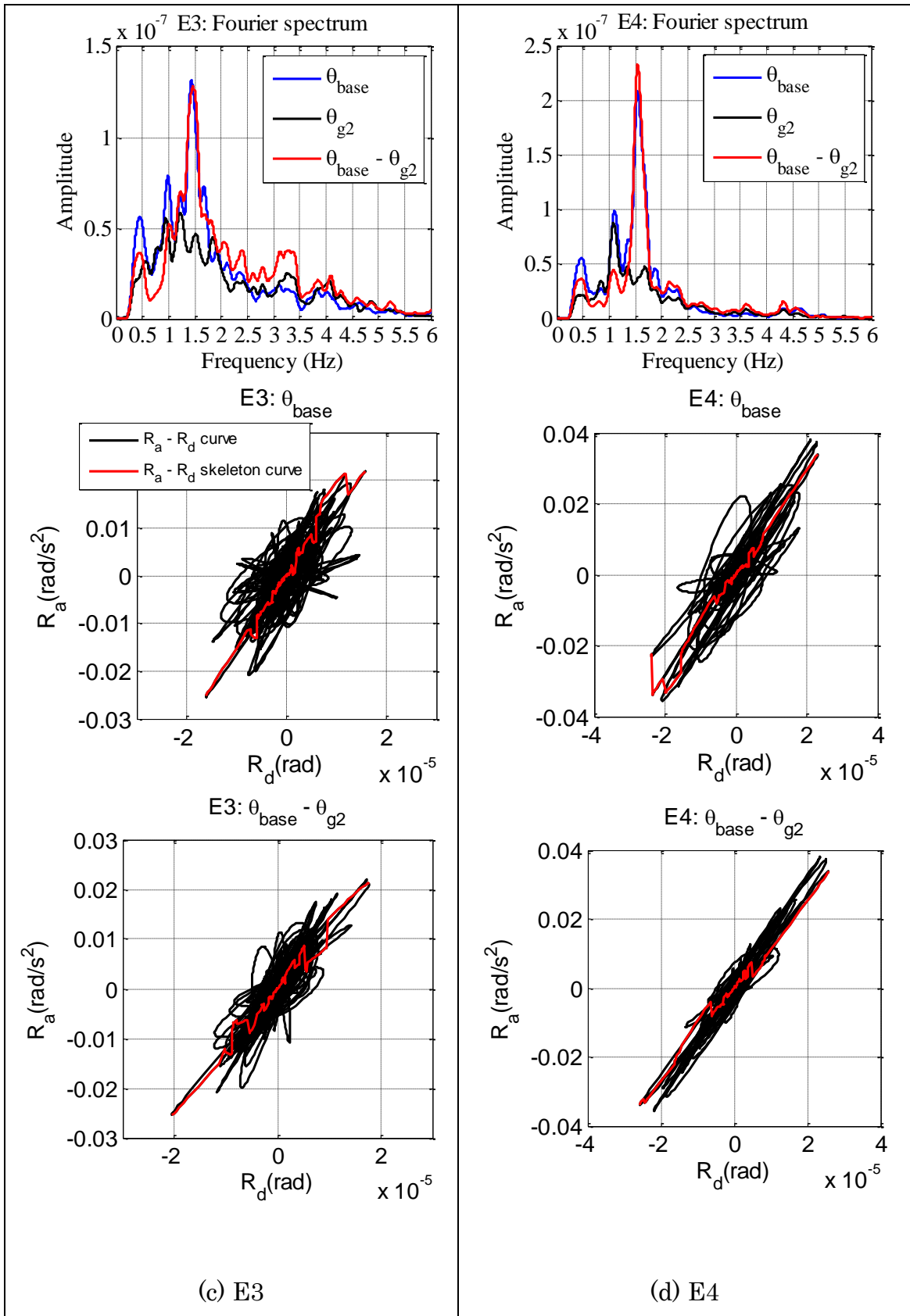Fig. 5.17 Comparison of the influences of the different θ_g of the ground on $R_a - R_d$ for earthquake E7 in N-S direction

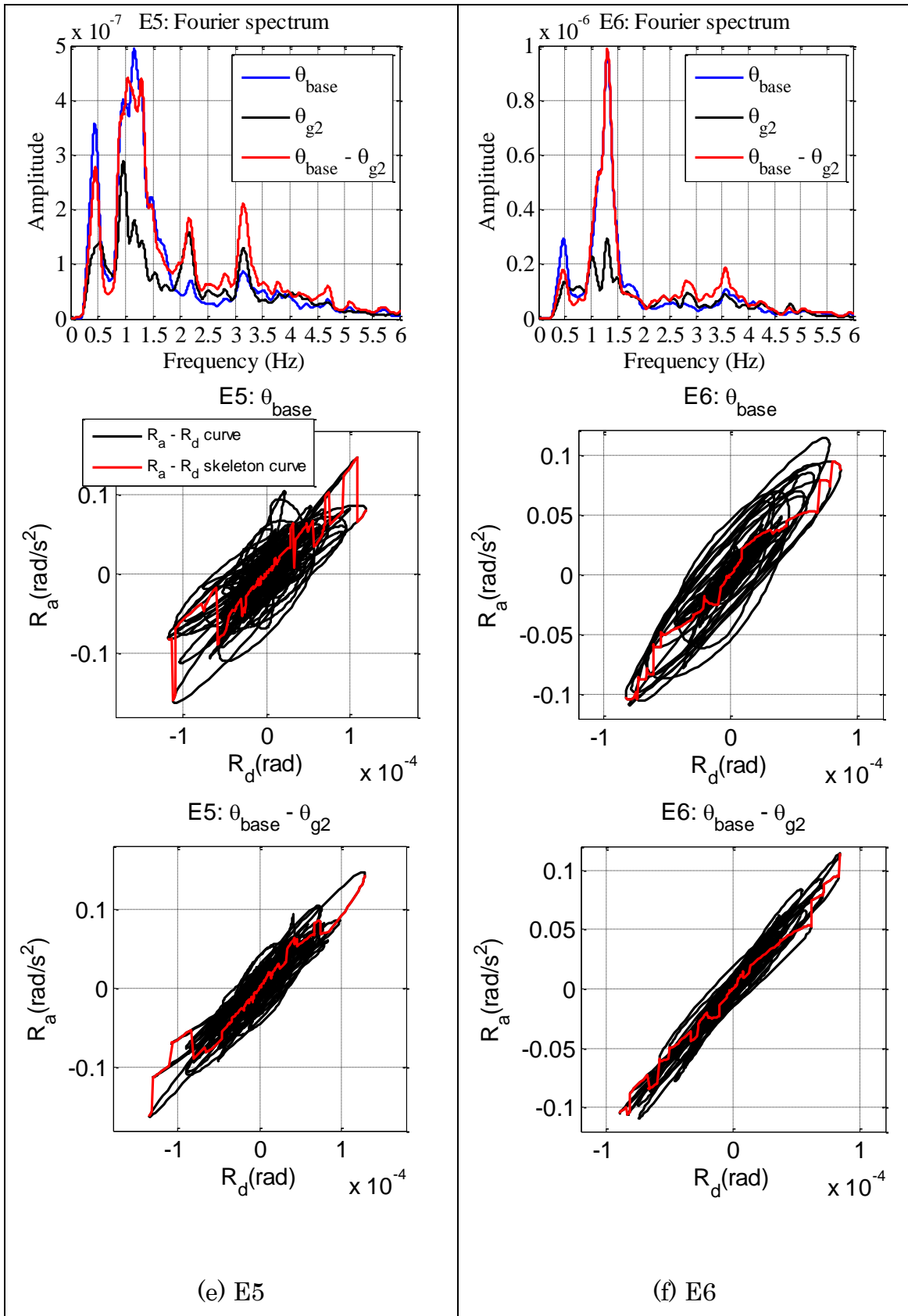(a) E1   (b) E2

(c) E3

(d) E4

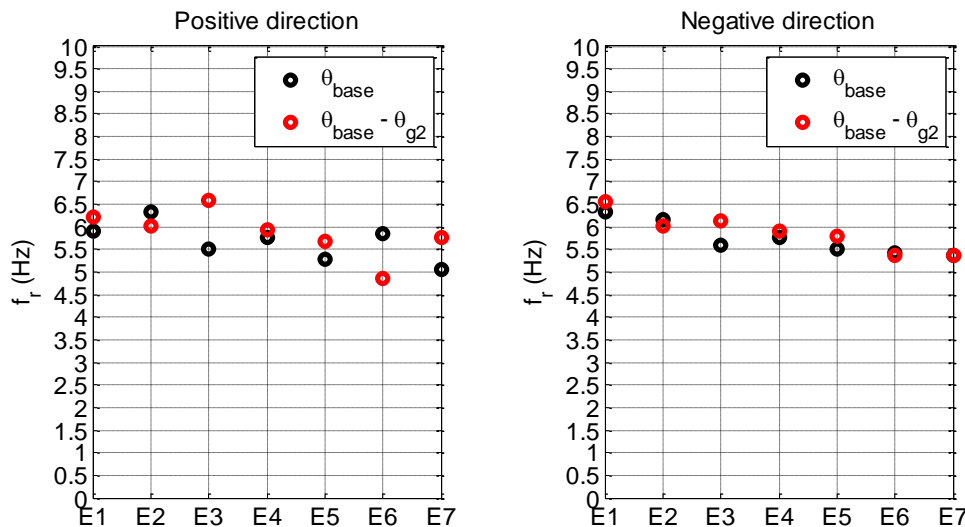Fig. 5.18 Influence of θ_{g2} on the $R_a - R_d$ curves in N-S direction

Fig. 5.19 Influence of θ_{g2} on the fundamental frequency of the rocking

motion of the foundation in N-S direction

5.7.4 Influence of θ_{g2} on the shape of the $R_a - R_d$ curve

As for the influence of the θ_{g2} on the shape of the $R_a - R_d$ curves, all the 7

earthquakes were discussed. Just as what is shown in Figure 5.18, when the

rotational motion of the ground θ_{g2} was deleted from the rocking motion of

the foundation θ_{base}, the hysteresis loops of the corresponding $R_a - R_d$

curves become compact and easy to understand. It can be concluded that the

soil responses were linear during the earthquakes E1-E6. The section 5.7.3

already showed the same conclusion. Besides, stronger rotational motion of

the ground θ_{g2} always have larger influence on $R_a - R_d$ curves.

As for earthquake E1, see Figure 5.18 (a): Because θ_{g2} was very small

during the earthquake, so the influence of θ_{g2} on the shape of $R_a - R_d$

curve was very litte.

For earthquake E2, E4, E5 and E6, see Figure 5.18 (b), (d), (e) and (f): the

105

influence of θ_{g2} on $R_a - R_d$ curves was strong, but the influence of θ_{g2} is almost directlyeliminated.

For earthquake E3, see Figure 5.18 (c): it seems that inflence of the rotational motion of the ground on the $R_a - R_d$ curve is much more complicated, and $R_a - R_d$ curve did not become simple after eliminating θ_{g2}. However, because the rocking motion is not strong compared with other earthquakes and the $R_a - R_d$ skeleton curve shows the linearity of the soil response, it can be accepted that the soil response during the eartqhuake was linear.

5.7.5 Influence of θ_{g2} on the fundamental frequency for the rocking motion

After eliminating (means $\theta_{base} - \theta_{g2}$) the influence of θ_{g2}, the $R_a - R_d$ curves and $R_a - R_d$ skeleton curves become easier to understand and analyze. Because the soil response for the 7 earthquakes are linear, so the maximum peak response points of the $R_a - R_d$ curves were seleted to calculate the fundamental frequency (f_r) for the rocking motion of the foundation. In section 5.2.2, a method based on ploygonal line was brought to evaluate the soil response, and the R_d in this method is corresponding for the θ_{base} without deleting θ_{g2}; and the f_r was also calculated using maximum peak response points.

The influence of θ_{g2} on the fundamental frequency for the rocking motion in N-S direction was evaluated in Figure 5.19: θ_{base} means the f_r contains the influence of θ_{g2}, and $\theta_{base} - \theta_{g2}$ means f_r deletes the influence of θ_{g2}. Discussions were made as follows according to Figure 5.19:

(1) The approximate value of f_r is about 6.5Hz – 5.0Hz. And there is a trend that f_r decreased gradually from about 6.5 Hz to about 5.5 Hz for earthquakes E1-E7, expecially in the Negative direction.

(2) For earthquakes E3, E6 and E7, the influence of θ_{g2} on the f_r is a little large in Positive direciton of the response. Compared with the influence of θ_{g2} on the hysteresis loops of the $R_a - R_d$ curves, the influence of θ_{g2} on the f_r maybe not so outstanding.

Totally, no matter eliminating or without eliminatingdeleting θ_{g2}, the maximum peak response points of the $R_a - R_d$ curves can be used to calculate f_r (fundamental frequency of the fundation for rocking motion).

5.7.6 Discussion on the influence of rotation motion of the ground on the $R_a - R_d$ curve

In this section, I analyzed the influence of the rotational motion on the $R_a - R_d$ curve of the foundation in N-S direciton. It is found that although the rotational motion of the ground surrounding the building affected the hysteresis loops of the $R_a - R_d$ curve very much (especially when the rotational motions of the ground surrounding the building were large), the influence of the rotational motion of the ground on f_r was not so large. Besides, rotational motion of the ground surrounding the building was influnced by the locations of the measurement points.

In this research, I no measurement points were located in the ground in E-W direction, so no analysis was made on the influence of the rotational motion of the ground on the $R_a - R_d$ curve in E-W direction.

5.8 Conclusions and discussion

A simple $R_a - R_d$ curve of the soil for the rocking motion was presented in this paper, which can be used for the evaluation of real-time seismic performance of soil and rocking soil stiffness. In this paper, the maximum response points of the $R_a - R_d$ curves of an eight-story SRC building in earthquakes were used to calibrate the rocking stiffness of the soil, and three conclusions can be made as follows:

(1) The Polygonal Lines restored from the $R_a - R_d$ curves can help us understand the real-time performance changes of the soil during earthquakes. The outstanding peak response points of $R_a - R_d$ curves are important for understanding the current properties of the soil, as the superstructure reaches its peak deformation at the same time.

(2) The rotation motion of the ground surrounding the building has a large influence on the $R_a - R_d$ curves, especially on the hysteresis loops of the $R_a - R_d$ curves. However, the influence of the rotation motion of the ground surrounding the building on the maximum peak response points of the $R_a - R_d$ curves are not so large. And the rotation motions of the ground surrounding the building are influeced by the locations of the measurement points, which needs to be researched by Simulation Analysis in the future.

(3) For the researched SRC building that has an embedment spread foundation, the calculation method of response and limit strength published by the AIJ underestimated the rocking stiffness of the soil, and the vertical ground reaction force coefficient k_v defined by JARA standard cannot reflect the real measurement of the soil stiffness; one important reason is because of

the definition of the scaling factor α in section 5.5.2, which does not completely consider the influence of the different strain levels in the current design methods[15]. For the large strain levels under strong earthquakes in this research, scaling factor α = 0.25 may be too small.

Besides, the estimation of the total mass has a significant influence on the calibration of the rocking stiffness.

However, the fundamental rocking period increased to approximately 0.25 s after Earthquake E5 (the Tohoku Earthquake off the Pacific Coast in 2011) in the E–W direction, whereas almost no changes of the fundamental rocking period took place in the N–S direction. It is necessary to make further research on that phenomenon in the future.

Besides, as for the embedment spread foundation in the paper, it is impossible to know how much influence of the embedment effect (exists in the sides of foundation) on the total rocking stiffness of soil under earthquake condition. We need to make further research on that point to directly evaluate the vertical soil stiffness under the foundation.

References:

1) Architecture Institute of Japan: Seismic response analysis and design of buildings considering dynamic soil-structure interaction, pp.127-131, 2006.

2)Shinichiro Tamori and Masanori Iiba: Study on accuracy of sway and rocking springs in soil-structure interaction proposed by the calculation method of response and limit strength—Evaluation with predominant frequency and mode, AIJ Hokuriku Research Reports, Vol. 47, pp. 80–83, 2004.7.

3)Shinichiro Tamori and Masanori Iiba: Study on accuracy of sway and rocking springs in soil-structure interaction proposed by the calculation method of response and limit strength—Evaluation with predominant frequency and mode, AIJ Hokuriku Research Reports, Vol. 48, pp. 157–160, 2005.7.

4)Masafumi Mori, Nobuo Fukuwa, Rieko Sakai, and Xuezhang Wen: Effects of side and base elements of embedded spread foundations on dynamic soil-structure interaction and conventional estimation methods for soil springs by composing the impedance of each element, J. Struct. Constr. Eng., AIJ, No. 626, pp. 535–542, 2008.4.

5)Koichi Kusunoki and Masaomi Teshigawara: A new acceleration integration method to develop a real-time residual seismic capacity evaluation system, J. Struct. Constr. Eng., AIJ, No. 569, pp. 119–126, 2003.7.

6)Manabu Kawamura, Koichi Kusunoki, Miho Yamashita, Yuki Kattori, Daiki Hinata, Miguel Augusto, Diaz Figueroa, and Akira Tasai: Study of a new method to compute the performance curve of real structures with

acceleration sensors in the case of SDOF system structures, J. Struct. Constr. Eng., AIJ, No. 688, pp. 1061–1069, 2013.6.

7)Koichi Kusunoki, Daiki Hinata, Yuki Hattori, and Akira Tasai: Development of a new method of realtime residual seismic capacity evaluation of existing structures with accelerometers in the case of MDOF system structures, J. Struct. Constr. Eng., AIJ, No. 699, pp. 613–620, 2014.5.

8)Ligang Li, Akihiro Nakamura, Toshihide Kashima, and Masaomi Teshigawara: Earthquake damage evaluation of an 8-story steel-reinforced concrete building using $S_a - S_d$ curves, J. Struct. Constr. Eng., AIJ, No. 702, pp. 1107–1116, 2014.8.

9)PAUL C. JENNINGS and JACOBO BIELAK: Dynamics of Building-Soil Interaction, Bulletin of the Seismological Society of America, Vol.63, NO.1, pp.9-48, 1973.2.

10)Anil K. Chopra et al.: Dynamics of structures: Theory and applications to earthquake engineering (second edition), 2002.

11)Toshihide Kashima and Yoshikazu Kitagawa: Dynamic characteristics of a building estimated from strong motion records using evolution strategy, J. Struct. Constr. Eng., AIJ, No. 602, pp. 145–152, 2006.4

12) Architecture Institute of Japan Kanto Branch: Structural design of reinforced concrete structures, 2002.

13) Architecture Institute of Japan: Workshop: Simplified Calculation Method for Soil-Structure Dynamic Interaction Effect, pp.2-9 – 2-16, 2011.1.14.

14) Japan Road Association: Specifications for highway bridges—IV edition:

Substructure, pp.283-285. 311-312, 2012.3.

15) Kanto Branch of the Japanese Geotechnical Society,

http://www.jiban.or.jp/kantou/group/pdf/H19hokoku.pdf (2007)

Chapter 6
Conclusions

6.1 Summary

The research in this paper focused on the application of seismic performance curve (Sa – Sd curve and Ra – Rd curve) of the buildings (BRI annex building, an 8-story SRC building) that experienced strong earthquakes, which used the filed measurement earthquake response data: firstly, Sa – Sd curve was used to evaluate the earthquake damage of SRC building; secondly, Ra – Rd curve was used to evaluate the seismic performance of soil and calibrate the vertical soil stiffness. The main achievements are summarized as follows:

(1) The earthquake damage of the researched SRC building can be evaluated using the real-time $S_a - S_d$ curves.

A simple damage assessment method based on two deformation levels (S_{d1} and S_{d2}) and the comparison of the corresponding fundamental frequencies of the peak response points (P1, P2 and N1, N2) were brought out. Then 11 strong earthquake responses of the building were evaluated using the previous method.

The results can be summarized as follows:

(a) Changes in $S_a - S_d$ curves (which reflect changes in seismic capacity) can be observed using measurement data. The fundamental frequency of the BRI annex building decreased from approximately 1.90 Hz to approximately 1.0 Hz between 1998 and 2012. This decrease was mainly caused by a decrease in the seismic capacity of the superstructure. The contribution of earthquake damage to the decrease in the fundamental frequency was approximately

11.1% in the E–W direction and 16.32% in the N–S direction. This damage occurred during the earthquake that occurred in 2011 off the Pacific Coast of Tohoku. Although no severe earthquake damage occurred between 1998 and 2010, the fundamental frequency of the superstructure decreased substantially (the superstructure stiffness decreased to approximately 50% of its initial value).

(b) The damage evaluation method based on the $S_a - S_d$ curve concept is simple and practicable. A simplified $S_a - S_d$ curve can help us understand changes that occur in the seismic capacity of a building in real time. Nevertheless, even though linearity and nonlinearity in $S_a - S_d$ curves can be observed, the initial stiffness of the curve is difficult to establish numerically. Therefore, the damage evaluation strategy presented in this research is considerably appropriate for cases in which the story drift angle is sufficiently large (for example, when the story drift angle of the building is greater than 1/3200 rad).

(c) The influence of the rocking motion on the $S_a - S_d$ curve of the BRI Annex building was very small for the 2011 off the Pacific Coast of Tohoku.

(d) Compared with the traditional damage observation method, $S_a - S_d$ curve can help us understand the global structural damage quickly and effectively.

(2) Soil stiffness of a building with embedment spread foundation can be estimated using the real-time Ra – Rd curves.

$S_a - S_d$ curve and $R_a - R_d$ curve can be used to evaluate the seismic

performance of the superstructure and soil respectively. $R_a - R_d$ curve can be got from the $S_a - S_d$ curve. Then maximum response points (PR+, PR- which are corresponding to the points PS+ and PS- in $S_a - S_d$ curve) of the $R_a - R_d$ curve will be used to calculate the natural fundamental frequency of the soil for rocking motion. Finally, those frequencies can be used to calibrate the rocking stiffness (largely influenced by the definition of the total mass of the superstructure) of the soil. Then the results can be summarized as follows.

(a) As for the researched SRC building that has a embedment spread foundation under the condition of the strong earthquakes, the calculation method of response and limit strength adopted by AIJ underestimated the vertical soil stiffness; while the method in JARA overestimated the vertical soil stiffness. And the calculation method of the total mass has a great influence on the calibration of the rocking stiffness.

(b) The rotation motion of the ground surrounding the building has a large influence on the $R_a - R_d$ curves, especially on the hysteresis loops of the $R_a - R_d$ curves. However, the influence of the rotation motion of the ground surrounding the building on the maximum peak response points of the $R_a - R_d$ curves are not so large. And the rotation motions of the ground surrounding the building are influeced by the locations of the measurement points, which needs to be researched by Simulation Analysis in the future.

The seismic performance curve (SPC) of the field measurement building can help us understand the performance of the superstructure and the soil quickly and simply. We can use the SPC to evaluate the earthquake damage

of the superstructure and calibrate the soil stiffness. But the applicability of the methods need to be verified with much more earthquake response data of other kinds of buildings (such as buildings with soft story, asymmetrical buildings, taller buildings etc.), and also the practicability under the condition of large nonlinear responses caused by very strong earthquakes.

(3) According to the results of Chapter 4 and Chapter 5, it can be confirmed that the decrease of the fundamental frequncey of the building from 1998 to 2012 is because of the loss of the superstructure stiffness (fundamental frequency decreased from about 1.9 Hz to 1.0Hz), not because of the fluctuations of the rocking stiffness of soil (fundamental frequency is about 6.5Hz~5.5Hz).

6.2 Prospects

In the present research, the research mainly focused on the application of performance curve on the seismic evaluation. A large number of field measurement earthquake response data of a kind of 8-story SRC building was researched in detail. Performance curves were used to evaluate the damage situation of the superstructure and the soil stiffness respectively using the field measurement data. The research discussed the applicability of performance curves of the real building in earthquakes when considering soil-structure interaction effect. The research achievements showed that performance curve is an effective tool for the seismic evaluation of the researched in-service building. Real-time seismic performance changes of the

building and the soil could be observed directly from the performance curves, which excel the vibration based methods.

However, there are two limitations in the present research, which are as follows:

1. Lack of large nonlinear earthquake response. In the present research, the researched building was not damaged seriously and the nonlinearity of the earthquake responses of the building was not large enough. As a result, it was impossible to test the practicability of performance curve under the condition of large nonlinear response. And some related important research points are: (1) influence of nonlinear response on the number and locations of accelerometers installed in a building; (2) accuracy of SDOF model under large nonlinear response; (3) accuracy of Wavelet Transform Technology to extract fundamental response under large nonlinear response; (4) the influence of the residual displacement on the performance curve for large nonlinear response.

2. The researched building is a kind of regular symmetrical 8-story SRC building, it is necessary to study the applicability of performance curve in other kinds of buildings. For example: (1) for irregular unsymmetrical buildings; (2) for buildings with soft story; (3) for low-rise buildings, middle-rise buildings and high-rise buildings, the difference among them; (4) for buildings with base-isolation system and other seismic systems. The large nonlinearity is also an important problem the other kinds of buildings should face.

Based on the previous introduction, the research plan will be constructed

117

according to the mentioned problems above, which is aimed to extend the applicability of performance curve to more kinds of buildings. The detailed outlines of the future research includes following contents:

1. Evaluate the influence factors on the accuracy of performance curve, such as nonlinearity of response, residual displacements, Wavelet Transform Technology, location and number of accelerometers. Then we will access a possible measurement system which uses limit accelerometers to get expected performance curve of the measurement buildings, for example only 2 accelerometers (accelerometers are installed in base floor and roof floor).

2. Discuss whether the proposed measurement system in purpose 1 will be suitable for some other kinds of buildings (irregular unsymmetrical buildings; buildings with soft story; low-rise buildings, middle-rise buildings and high-rise buildings; buildings with base-isolation system and other seismic systems).

3. Based on the previous research, some important problems will be found and it is necessary to solve the problems using some other new methods. Finally, performance curve should be improved to be more accurate and effective for earthquake damage and prediction of real buildings.

Symbols and Abbreviations

R	Residual Seismic Capacity Ratio Index
I_s	Seismic capacity index of structure before earthquake damage
I_s^D	Seismic capacity index of structure considering deteriorated member capacity
S_a	Representative base shear force coefficient
S_d	Representative displacement
CA_M	Maximum response point in the main shock
DE_A	Demand point in aftershock
CP	Collapse point
SDOF	Single-Degree-Of-Freedom
MDOF	Multi-Degree-Of-Freedom
SRC	Steel Reinforced Concrete
R_a	Representative rocking-moment coefficient.
R_d	Representative rocking angle
$[M]$	Mass matrix of a Multi-Degree-Of-Freedom model
$[C]$	Damping matrix of a Multi-Degree-Of-Freedom model
$[K]$	Stiffness matrix of a Multi-Degree-Of-Freedom model
$\{U\}$	Displacement vector of a Multi-Degree-Of-Freedom model
$\ddot{u}_g$	Input ground motion
$\{s_n\}$	Modal inertia force distribution for nth mode
$\{\phi_n\}$	The nth natural vibration mode of the structure
Γ_n	Modal participation factor
ω_n	Natural vibration frequency for nth mode

ξ_n	Damping ratio for the nth mode
S_i	Component signal for the Rank i
$f_{s,\ i}$	Nyquist frequency for Rank i
dt	Time step of the sampling for accelerometers
$u_{i1}{}^f$	Fundamental displacement
$\ddot{u}_g{}^f$	Fundamental input ground motion
M_e	Equivalent mass
E_i	Envelope size of the displacement time history for Rank i
E_o	Envelope size of the displacement time history for original signal
d_i	Difference between E_i and E_o
PGA	Peak Ground Acceleration
IJMA	Japanese Meteorological Agency Intensities
D_{ai}	Drift angle of the superstructure for deformation level i
Δ_1	The assumption representative displacement
M_r	Rotation moment of the foundation
H_e	Equivalent height
k_r	Stiffness for the rocking motion of the foundation
c_R	Damping for the rocking motion of the foundation
ω_r	Circular frequency for the rocking motion of the foundation
K_{rb}	Rocking stiffness for the vertical direction
K_{1r}	Rocking stiffness for the first soil layer
β_R	Contribution index of all soil layers for the total rocking stiffness
K_{re}	Rocking stiffness casued by the foundation embedment effect
ξ_{re}	Reduction coefficient

D_e Embedment depth of the foundation

K_{hb} Horizontal soil stiffness

K_r Rocking stiffness

k_v Vertical ground reaction force coefficient

α Scaling factor

θ_{rela} Relative rotational angle between the foundation and its surrounding ground

θ_{base} Rotational angle of the foundation

θ_g Rotational angle of the ground

f_r Fundamental frequency for the rocking motion of the foundation

PUBLICATIONS
Journal:

1. Ligang LI, Akihiro NAKAMURA, Toshihide KASHIMA and Masaomi TESHIGAWARA: Earthquake Damage Evaluation of an 8-Story Steel-Reinforced Concrete Building Using Sa – Sd Curves, J. Struct. Constr. Eng. AIJ, No.702, pp. 1107–1115, 2014.8.

2. Ligang LI , Masaomi TESHIGAWARA, Akihiro NAKAMURA and Toshihide KASHIMA: SEISMIC EVALUATION OF AN 8-STORY SRC BUILDING USING PERFORMANCE CURVE IN THE 2011 OFF THE PACIFIC COAST OF TOHOKU EARTHQUAKE, Proceedings of the Japan Concrete Institute, Vol.36, No.2, pp.697-702, 2014.

3. Ueno Daisuke, Ligang LI, Akihiro NAKAMURA and Masaomi TESHIGAWARA: Evaluation of the Dynamic Characteristics of a Middle-Rise Steel Reinforce Concrete School Building Using Performance curve, Proceedings of the Japan Concrete Institute, Vol.36, No.2, pp.733-738, 2014.

4. Ligang LI, Akihiro NAKAMURA, Toshihide KASHIMA and Masaomi TESHIGAWARA: Evaluation of Rocking Soil Stiffness Using Performance Curves of an Eight-Story Steel-Reinforced Concrete Building With Embedded Spread Foundation, J. Struct. Constr. Eng. AIJ. No.710, 2015.4. (Accepted)

PUBLICATIONS

Proceedings of International Conference:

1. Ligang LI, Akihiro NAKAMURA, Toshihide KASHIMA and Masaomi TESHIGAWARA: An Simple Earthquake Damage Evaluation Method Using S_a-S_d Curves and the Rudimental Research on the Accuracy of the Method, Sixth World Conference on Structural Control and Monitoring(6WCSCM), Barcelona, Spain, pp.1428-1435, 07,2014.

2. A. Nakamura, Ligang LI, and M. Teshigawara: Observation of the Rocking Motion of a Middle-Rise Reinforced Concrete Building, Sixth World Conference on Structural Control and Monitoring (6WCSCM), Barcelona, Spain, pp.2532-2540, 07,2014.

3. Ligang Li, Toshihide Kashima, Akihiro Nakamura and Masaomi Teshigawara: STUDY ON THE ROCKING EFFECT OF AN EIGHT-STORY SRC BUILDING, 10CUEE CONFERENCE PROCEEDINGS , 10th International Conference on Urban Earthquake Engineering (10CUEE), Tokyo, Japan, pp.1721-1729, 3.2013.

Oral Presentation:

1. Ligang LI, Akihiro NAKAMURA and Masaomi TESHIGAWARA: Observation of the Rocking Effect of a Low-Rise Building, Summaries of Technical Papers of Annual Meeting Architectural Institute of Japan, Nagoya, Japan, 2012.

2. Ligang LI, Akihiro NAKAMURA and Masaomi TESHIGAWARA: Study on the Stiffness Degradation of an Eight-Story SRC Building, Summaries of Technical Papers of Annual Meeting Architectural Institute of Japan, Hokkaido, Japan, 2013.

3. Ligang LI, Akihiro NAKAMURA and Masaomi TESHIGAWARA: Evaluation of the Rocking stiffness of Soil Using Field Measurement Data, Summaries of Technical Papers of Annual Meeting Architectural Institute of Japan, Kinki, Japan, 2014.

ACKNOWLEDGEMENTS

ACKNOWLEDGEMENTS

<div align="right">
Li Ligang

January 2015
</div>